ISAS - INTERNATIONAL SCHOOL FOR ADVANCED STUDIES

Dynamics and Evolution of Polar Ring Galaxies

Thesis submitted to the
International School for Advanced Studies, Trieste, Italy
– Astrophysics Sector –
in partial fulfillment of the requirements for the degree of

Doctor Philosophiæ

Candidate:
Magda Arnaboldi

Supervisors:
Prof. Dennis W. Sciama
Prof. Massimo Capaccioli
Prof. Linda S. Sparke

Academic Year 1991/1992

SISSA - SCUOLA INTERNAZIONALE SUPERIORE DI STUDI AVANZATI
TRIESTE
Strada Costiera 11

TRIESTE

Contents

Chapter 1

Introduction and summary

Polar Ring (PR) galaxies are systems composed of a central component, normally an S0 galaxy, circled by a luminous annulus with gas, dust, and stars, aligned along the minor axis of the host galaxy. From the earliest studies (Bertola & Galletta 1978, Lausten & West 1980, Schweizer *et al.* 1983, Whitmore *et al.* 1987a) they were shown to be very effective laboratories of the dark matter problem, the intrinsic shape of hot stellar bodies, and interaction/merging between galaxies.

The questions stressed by the first papers (Schweizer *et al.* 1983, Whitmore *et al.* 1987a,b) on these systems dealt with the presence of the dark halo around the central component and its three–dimensional shape; especially NGC 4650A which showed the best evidence of a dark matter halo. The rotation curve for the ionized gas in the ring is *flat* and extended out to $\sim 3R_{25}$[1], a distance comparable with the most extended radio rotation curves obtained for spiral galaxies using the 21 cm HI neutral hydrogen emission.

At the same time, information on the three–dimensional shape of dark matter halos were deduced from the comparison between the velocities of stars in the host galaxy and that of gas in the ring, since they are lying on nearly orthogonal planes. Whitmore *et al.* (1987a,b) using the scale free potential of Monet *et al.* (1981) and a straight comparison of the above velocities derived that the dark halos were spherical in the case of three PR systems. A similar conclusion has been derived previously by Schweizer *et al.* (1983) and is based on stability arguments. Ring structures embedded in a flattened potential are perturbed by its quadrupole moment and their precession rates depend both on radius and inclination. They estimated that such structures, tilted away from 90°, are subject to differential precession and disrupted

[1] R_{25} is the distance corresponding to the 25–mag–arcsec^{-2} isophote of the central S0

in less than a Hubble time. An alternative for the stability of inclined is a spherical potential, or nearly orthogonal rings, since in that case the PR precession rate would easily exceed the Hubble time.

But still the PR dilemma remains: PR structures are found normally $10° - 20°$ far from the pole, and they should feel the differential precession and be disrupted, while, were the potential spherical, the ring structures should be found at any inclinations.

Sparke (1986) discussed whether self–gravity would be able to stabilize PR in an axisymmetric oblate potential. She studied the dynamics of precessing rings in a scale free potential of Monet *et al.* (1981) and found that stable PRs are possible if their masses exceed a minimum value. For lighter PR, stable configurations are possible just near the symmetry plane of the potential. For intermediate masses, PR are stable near either 90° or 0°. If the PR is really massive it evolves independently from the potential and is stable at whatever angle.

Moreover, a detailed analysis of the rotation curve for the gas in the ring of NGC 4650A, and a different correction of the stellar rotation curve for asymmetric drift, lead Sackett and Sparke (1990) to state that the dark halo in NGC 4650A is probably not spherical but flattened.

Regarding the stability of PR structures another model has been discussed: the preferred orientation model (Steiman–Cameron & Durisen 1982, 1984, 1988, Habel & Ikeuchi 1985, Varnas 1986, Christodoulou 1988, Steiman–Cameron 1990) proposes that the gravitational potentials of S0 galaxies are slightly triaxial in nature. This small departure from axisymmetry will lead a fraction of all dissipative disks accreted by S0s to settle into the polar orientation, because dissipative interactions among elements of a twisted gas disk will lead to the transport of angular momentum, causing the radial inflow of material and the settling of the disk into a steady state, or "preferred" orientation. In triaxial galaxies the polar orientation is also preferred. If the figure of the potential is static, then a completely settled ring will be orthogonal to the underlying S0 disk. If the figure is very slowly rotating, then the ring will be slightly inclined to the polar orientation and may be slightly warped away from the pole at large radii.

So the general picture is that large PRs around S0s indicate the presence of dark matter halos, whose shape is probably flattened, either axisymmetric or triaxial.

Recently, Whitmore *et al.* (Polar Ring Catalogue, PRC, 1990) have published a survey of polar ring galaxies and systems possibly connected with them, in order to enlarge the statistics on these objects. An analysis performed by Whitmore (1991) on the data published in the PRC indicates the presence of two classes of PR: the first one, whose prototype is the system NGC 4650A – called wide polar ring – and a

second one, where the central component is round and the ring appears narrow and contained in the optical radius of the central component, called narrow polar ring. This second class provides the opportunity to study the intrinsic shape of the hot stellar system, since the PR probes the gravitational field at smaller radii.

This thesis deals with the subjects stressed in the above presentation, both theoretically and observationally. In the first part of the thesis (Chap. 2) we have analysed the dynamics of PRs, considered as a probe for the intrinsic shape of the potential well around galaxies (Arnaboldi & Sparke 1992).

We have developed a numerical code which simulates the evolution of massive rings, modelled as a series of circular wires, concentric with the underlying galaxy, embedded in a axisymmetric or triaxial potential. We find that tilted massive rings cannot be stable in a static triaxial potential: the torque of the gravitational potential with respect to the line of nodes causes the structures to wobble, *i.e.* to change its inclination with respect to the equatorial plane of the potential, and then to change the sense of precession. The stability of tilted rings is possible if the triaxial potential is tumbling: in this case PR configurations are possible for lighter mass than in the correspondent axisymmetric oblate case. We also find that, in the limit of the ring mass going to zero, tilted rings away from the equatorial plane are possible in the triaxial rotating case, but not in oblate potential. The warped solutions found for the tumbling triaxial case with mass going to zero, bend towards the equator, and are the massive analogies of the anomalous retrograde orbits (Schwarzschild 1982). For intermediate masses the rings are found either near the pole or near the equatorial plane, reproducing the statistic of the orientations observed in polar ring systems. Stable solutions near the pole are warped and they bend towards it, away from the equator.

From the point of view of spectroscopic observations, the warping of gas rings may effect the rotation curve produced by the galactic potential due to projection effects: the rotation curve may appear rather complex, even if the underlying potential is smooth. We develop a code (Arnaboldi & Galletta 1992) which computes the projected rotation curves at different slit positions on a given warped structure. The numerical code and several applications to different galactic systems are described in Chap. 3.

We applied these theoretical and numerical tools to study the prototype of the "Narrow Polar Ring" class, the AM 2020–504 system (Arnaboldi *et al.* 1991, 1992a,b). We acquired new photometric and spectroscopic data which revealed the peculiarity of this system. In this case the host galaxy is an E4 with a dynamically decoupled core; this fact, together with the difference in color between the material

in the ring and that in the host galaxy, and the huge amount of HI detected in the system, unusual for an elliptical galaxy, support the accretion/merging scenario for PR. Rotation curves for the gas in the ring have successfully been reproduced with a self gravitating warped structure in an oblate potential, the relevant parameters of the model are presented and discussed in Chap. 4.

The inferred accretion scenario for narrow PR deduced from the observations of the "prototype" AM 2020–504 is highly testable, since the possible new material accreted from the galaxy during its evolution would lead to a second burst of star formation. This new burst will affect the spectral energy distribution (SED) of the underlying elliptical galaxy and perturb it in the UV part. To test the proposed evolutionary scenario for narrow polar rings we acquired new IUE data to investigate the UV part of the spectrum of AM 2020–504 (Arnaboldi *et al.* 1992c). The UV spectrum of AM 2020–504 clearly shows the presence of a recent burst of star formation: the data and model for the SED are described in Chap. 5. The model for the star burst also gives a lower limit to the age of the PR in AM 2020–504, indicating that the structure is quite young.

Work is still in progress: we have acquired new spectroscopic data for AM 2020–504 to investigate its decoupled core. There is some evidence for non–circular motions but we are still analysing the data from the August 1992 run at the ESO 2.2m telescope. In addition other photometric and spectroscopic data have been acquired for another narrow PR system, ESO 603–G21, and the system ESO 474–G26, which has two rings at orthogonal angles. All these round galaxies with narrow gas rings appear surrounded by small companion galaxies, and are found in the center of small clusters of galaxies. In the case of ESO 603–G21, the narrow band image centered on the Hα emission line shows ionized gas clouds that seem to be settling down in the ring: perhaps this is a snap shot of the on–going formation of the ring in the system.

Acknowledgements– I would like to thank my Supervisors, Prof. Sciama, Prof. Capaccioli, and Prof. Sparke for their help and support during the realization of this work. Special thanks are given to Linda Sparke for the assistance and the friendship she offered me while I was in Madison, Wisconsin USA. Moreover, I would like to thank M. Ferrario, R. Corradi, N. Caon, M. D'Onofrio, G. Mackie, R. Lee, E. Cappellaro, E. Held and L. Buson for their help during my training as an observing astronomer and with data reduction packages. I gratefully acknowledge the help and the support of Prof. Galletta in dealing with rotation curves of warped structures and projection effects, and of Prof. Barbaro regarding the model of star–bursts in elliptical galaxies. I would like to thank the heads of the Depts. of Astronomy at the University of Padova and of Wisconsin–Madison, where a significant part of this work has been realized.

I gratefully acknowledge the "Sandra and Enea Mattei" Foundation for partial financial support which allowed me to develop part of my Ph. D. research at the University of Wisconsin–Madison.

I would like to end with special thanks to Fabio Gnidica and my family for their moral support.

Bibliography

[1] Arnaboldi M., Capaccioli M., Barbaro G., Buson L., Longo G., 1992c, A&A, submitted

[2] Arnaboldi M., Capaccioli M., Cappellaro E., Held E.V., Sparke L.S., Mackie G., 1991, The Polar Ring Galaxy AM 2020–504. In: 7^{th} Annual Florida Workshop in Non Linear Astronomy: Astrophysical Disks, in press

[3] Arnaboldi M., Capaccioli M., Cappellaro E., Held E.V., Sparke L.S., 1992a, A&A in press

[4] Arnaboldi M., Capaccioli M., Cappellaro E., Held E.V., Sparke L.S., 1992b, The Polar Ring Galaxy AM 2020–504. In: Structure and Chemical Evolution of Early Type Galaxies, in press

[5] Arnaboldi M., Galletta G., 1992, A&A, submitted

[6] Arnaboldi M., Sparke L.S., 1992, in preparation

[7] Bertola F., Galletta G., 1978, ApJ 226, L115

[8] Christodoulou D.M., 1989, Thesis, Lousiana State University

[9] Habe A., Ikeuchi S., 1985, ApJ 289, 540

[10] Lausten S., West R.M., 1980, J. Ap. Astron. 1, 177

[11] Monet D.G., Richstone D.O., Schecter P.L., 1981, ApJ 245, 454

[12] Sackett P.D., Sparke L.S., 1990, ApJ 361, 408

[13] Schwarzschild M., 1982, ApJ 263, 599

[14] Schweizer F., Whitmore B.C., Rubin V.C., 1983, AJ 88, 909

[15] Sparke L.S., 1986, MNRAS 219, 657

[16] Steiman–Cameron T.Y., 1990, preprint

[17] Steiman–Cameron T.Y., Durisen R.H., 1982, ApJ 263, L51

[18] Steiman–Cameron T.Y., Durisen R.H., 1984, ApJ 276, 101

[19] Steiman–Cameron T.Y., Durisen R.H., 1988, ApJ 325, 26

[20] Varnas S.R., 1986, Thesis, Monash University

[21] Whitmore B.C., 1984, AJ 89, 618

[22] Whitmore B.C., 1991, A Few Statistics from the Catalog of Polar Ring Galaxies. In: Casertano S., Sackett P., Briggs F. (eds.) Warped Disks and Inclined Rings around Galaxies. Cambridge University Press, p. 60

[23] Whitmore B.C., Mc Elroy D., Schweizer F., 1987a, ApJ 314, 439

[24] Whitmore B.C., Mc Elroy D., Schweizer F., 1987b, AM 2020–504: an Elliptical Galaxy with an Outer Ring. In: de Zeeuw T. (ed.) Proc IAU Symp. No. 127, Structure and Dynamics of Elliptical Galaxies. Reidel, Dordrecht, p. 413 (WMSb)

[25] Whitmore B.C., Lucas R.A., Mc Elroy D.B., Steiman–Cameron T.Y., Sackett P.D., Olling R.P., 1990, AJ 314, 439 (PRC)

Chapter 2

Ring Dynamics

2.1 Introduction

As pointed out by Sackett and Sparke (1990) the dark halo around a polar ring galaxy may not be spherical, and the dynamics of precessing rings can help in understanding whether the intrinsic shape of the flattened potential is axisymmetric or triaxial. In this chapter we are going to analyse the dynamics of rings around matter distributions with different three-dimensional shapes. We will briefly describe the equations of motions following Goldstein (1980) in Section 2.2; the gravitational potential (de Zeeuw & Pfenniger 1988) used to model the potential well around galaxies is discussed in Section 2.3 and a suitable computational method to evaluate the torques exerted by the gravitational field on the precessing ring is presented in Section 2.4. Following Sparke (1986), gravitational interactions between rings is taken into account to study the evolution of the ring structures: two different methods to compute forces between rings are described and compared in Section 2.5. Then the evolution of massive rings in axisymmetric and triaxial potentials is discussed in Section 2.6 and conclusions stated in Section 2.7.

2.2 Equations of motions

Let us consider a ring of radius r and linear density σ embedded in a potential $\Phi(x,y,z)$, where x,y,z are the cartesian coordinates in the galaxy system of reference $\Sigma(x,y,z)$. The potential $\Phi(x,y,z)$ contains both the potential $\Phi_g(x,y,z)$ generated by the matter distribution in a galaxy and the mutual potential $\Phi_m(x,y,z)$ due to the interaction with other massive rings. The ring plane Π has an inclination θ respect

to the xy–plane and its line of nodes is at an angle φ from the x–axis. In the ring system of reference $\Sigma'(x', y', z')$, the points on the ring are given by:

$$\begin{cases} x' = & r\cos\eta \\ y' = & r\sin\eta \\ z' = & 0 \end{cases} \tag{2.1}$$

where r is the radius and η is the parameter angle of the ring. We can express the coordinates x', y', z' in the galaxy system of reference $\Sigma(x, y, z)$ through the orthogonal transformation $x' = Tx$ where $T = C \cdot D$ and

$$C = \begin{pmatrix} 1 & 0 & 0 \\ 0 & \cos\theta & \sin\theta \\ 0 & -\sin\theta & \cos\theta \end{pmatrix} \tag{2.2}$$

$$D = \begin{pmatrix} \cos\varphi & \sin\varphi & 0 \\ -\sin\varphi & \cos\varphi & 0 \\ 0 & 0 & 1 \end{pmatrix} \tag{2.3}$$

(Goldstein 1980, p.146). So the coordinates of the points along the ring becomes

$$x = T^{-1}x' = D^T \cdot C^T \cdot x' \tag{2.4}$$

where

$$\begin{array}{lll} T^{-1}(1,1) = \cos\varphi & T^{-1}(1,2) = -\sin\varphi\cos\theta & T^{-1}(1,3) = \sin\varphi\sin\theta \\ T^{-1}(2,1) = \sin\varphi & T^{-1}(2,2) = \cos\varphi\cos\theta & T^{-1}(2,3) = -\sin\theta\cos\varphi \\ T^{-1}(3,1) = 0 & T^{-1}(3,2) = \sin\theta & T^{-1}(3,3) = \cos\theta \end{array} \tag{2.5}$$

So the ring coordinates in the system of reference $\Sigma(x, y, z,)$ are given by:

$$\begin{cases} x = & r(\cos\eta\cos\varphi - \sin\eta\sin\varphi\cos\theta) \\ y = & r(\sin\varphi\cos\eta + \sin\eta\cos\varphi\cos\theta \\ z = & r\sin\eta\sin\theta \end{cases} \tag{2.6}$$

Following Goldstein (1980), we derive the equations of motion for the ring precessing in the potential $\Phi(x, y, z,)$. In $\Sigma'(x', y', z')$ the ring lies in a plane perpendicular to z' and rotates at a rate $\dot{\psi}$ about that axis. The ring has a moment of inertia $I_3 = mr^2$,

where m is the ring mass, about z', and $I_1 = mr^2/2$ about the x', y' axes. The component of the vector angular velocity in the frame $\Sigma(x, y, z)$ are:

$$\begin{cases} \omega_x = & \dot{\theta}\cos\varphi + \dot{\psi}\sin\varphi\sin\theta \\ \omega_y = & \dot{\theta}\sin\varphi - \dot{\psi}\sin\theta\cos\varphi \\ \omega_z = & \dot{\psi}\cos\theta + \dot{\varphi} \end{cases} \tag{2.7}$$

The kinetic energy from the precession is then:

$$T = \frac{I_1}{2}(\dot{\varphi}^2\sin^2\theta + \dot{\theta}^2) + \frac{I_3}{2}(\dot{\varphi}\cos\theta + \dot{\psi})^2. \tag{2.8}$$

Considering only the potential energy of the ring due to the matter distribution of the galaxy:

$$V_g(\theta, \varphi) = \int_{ring} \Phi_g dM \tag{2.9}$$

the lagrangian of the ring precessing in the galactic potential is:

$$L = \frac{I_1}{2}(\dot{\varphi}^2\sin^2\theta + \dot{\theta}^2) + \frac{I_3}{2}(\dot{\varphi}\cos\theta + \dot{\psi})^2 - V_g(\theta, \phi). \tag{2.10}$$

In the general case we are exploring, the potential energy is an explicit function of the Euler angles θ, φ, so the only cyclic coordinate is ψ, which implies the its conjugate momentum is a constant of motion. The canonical momenta are:

$$\begin{aligned} P_\psi = & \frac{\partial T}{\partial \dot{\psi}} = I_3(\dot{\psi} + \dot{\varphi}) \\ P_\varphi = & \frac{\partial T}{\partial \dot{\varphi}} = I_1\dot{\varphi}\sin^2\theta + P_\psi\cos\theta \\ P_\theta = & \frac{\partial T}{\partial \dot{\theta}} = I_1\dot{\theta} \end{aligned} \tag{2.11}$$

Expressing the angular speeds $\dot{\psi}$, $\dot{\varphi}$, and $\dot{\theta}$ through their conjugate momenta, we can compute the hamiltonian for the system, given by:

$$H = \frac{P_\theta^2}{2I_1} + \frac{1}{2I_1}\frac{(P_\varphi - P_\psi\cos\theta)^2}{\sin^2\theta} + \frac{P_\psi^2}{2I_3} + V_g(\theta, \varphi) \tag{2.12}$$

and then the equations of motion for the ring precessing in the general potential energy $V_g(\theta, \varphi)$ are:

$$\begin{aligned}
\dot{\theta} &= \frac{P_\theta}{I_1} & \dot{P}_\theta &= -\frac{1}{I_1}\frac{(P_\varphi - P_\psi \cos\theta)(P_\psi - P_\varphi \cos\theta)}{\sin^3\theta} - \frac{\partial V_g}{\partial \theta} \\
\dot{\varphi} &= \frac{P_\varphi - P_\psi \cos\theta}{I_1 \sin^2\theta} & \dot{P}_\varphi &= -\frac{\partial V_g}{\partial \varphi} \\
\dot{\psi} &= \frac{P_\psi}{I_3} - \frac{\cos\theta(P_\varphi - P_\psi \cos\theta)}{I_1 \sin^2\theta} & \dot{P}_\psi &= 0
\end{aligned} \tag{2.13}$$

If we consider an axisymmetric potential, the lagrangian will depend explicitly only from the θ angle and P_φ becomes a constant of motion.

2.2.1 Steady precession

In an axisymmetric potential the condition for steady precession requires that the inclination angle θ should be a constant. Using the Lagrange's equation of motion for the θ coordinate:

$$\frac{d}{dt}\left(\frac{\partial L}{\partial \dot{\theta}}\right) - \frac{\partial L}{\partial \theta} = 0 \tag{2.14}$$

we obtain

$$I_1\ddot{\theta} - I_1\dot{\varphi}^2 \sin\theta\cos\theta + I_3\dot{\varphi}\sin\theta(\dot{\psi} + \dot{\varphi}\cos\theta) = -\frac{\partial V_g}{\partial \theta} \tag{2.15}$$

The conditions for steady precession are $\ddot{\theta} = \dot{\theta} = 0$, which simplifies eq. 2.15 to:

$$I_1\dot{\varphi}^2 \sin\theta\cos\theta - \dot{\varphi}\sin\theta P_\psi - \frac{\partial V_g}{\partial \theta} = 0 \tag{2.16}$$

In the case of slow precession, *i.e.* when in eq. 2.16 $\dot{\varphi}^2$ becomes negligible respect to $\dot{\varphi}$, the relation between the precession rate and the torque from the galactic potential becomes:

$$\dot{\varphi} = \frac{1}{P_\psi}\frac{\partial V_g}{\partial \cos\theta} \tag{2.17}$$

In the steady precession the sum of the angular momenta and the hamiltonian are conserved.

2.3 Potential–density pair

We would like to use in our model a potential obtained from a realistic density distribution via the integration of the Poisson's equation. For triaxial systems, the general case we are interested in, few explicit solutions of Poisson's equation are known. The most famous of these is the family of models where the density is stratified on similar concentric ellipsoids. We will use a class of triaxial density distributions for which Poisson's equation can be solved also by one–dimensional quadratures, We are interested in models which have a smooth density distribution that falls off not faster than $1/r^2$ at large radii, so that they are well suited for a description of galaxies with massive halos (de Zeeuw & Pfenninger 1988). The smooth density distribution in $\Sigma(x,y,z)$ is given by:

$$\rho(x,y,z) = \rho(m^2) = \frac{\rho_0}{1+m^2} \qquad m^2 = \frac{x^2}{a^2} + \frac{y^2}{b^2} + \frac{z^2}{c^2} \tag{2.18}$$

where $a : b : c$ are the axis ratios, and $a \geq b \geq c$, and the central density is equal to ρ_0. The total mass inside the ellipsoid $\tilde{m}$ is:

$$M(\tilde{m}) = 4\pi abc\rho_0(\tilde{m} - \arctan\tilde{m}) \tag{2.19}$$

So the total mass of the spheroid results infinite. The gravitational potential $\Phi_g(x,y,z)$ inside a density distribution $\rho = \rho(m^2)$ can be derived by means of the classical theory in Chapter 3 of Chandrasekhar (1969); it can be written:

$$\Phi_g = \pi Gabc \int_0^\infty \frac{du}{\Delta(u)} \int_0^{m^2(u)} \rho(m'^2) dm'^2 \tag{2.20}$$

where

$$m^2(u) = \frac{x^2}{a^2+u} + \frac{y^2}{b^2+u} + \frac{z^2}{c^2+u} \qquad \Delta(u) = \sqrt{(a^2+u)(b^2+u)(c^2+u)} \tag{2.21}$$

Using the density stated in eq. 2.18, the potential can be rewritten as:

$$\Phi = \pi G\rho_0 abc \int_0^\infty \ln[1+m^2(u)] \frac{du}{\Delta(u)} \tag{2.22}$$

2.3.1 Ellipsoidal coordinates

For the evaluations of the integrals in eq. 2.22 it is useful to change from cartesian coordinates (x,y,z) to confocal ellipsoidal coordinates (λ,μ,ν) (de Zeeuw 1985) defined

as the three roots for τ of the equation $m^2(\tau) = -1$ with $c^2 \leq \nu \leq b^2 \leq \mu \leq a^2 \leq \lambda$, otherwise rewritten to:

$$\frac{x^2}{a^2+u} + \frac{y^2}{b^2+u} + \frac{z^2}{c^2+u} = -1 \tag{2.23}$$

This equation becomes:

$$\tau^3 + A\tau^2 + B\tau + C = 0 \tag{2.24}$$

where

$$\begin{aligned} A &= -(\lambda+\mu+\nu) = -(a^2+b^2+c^2+r^2) && (2.25)\\ B &= \lambda\mu+\mu\nu+\nu\lambda = a^2b^2+c^2b^2+a^2c^2+ && (2.26)\\ &\quad x^2(b^2+c^2)+y^2(c^2+a^2)+z^2(b^2+a^2) \\ C &= -\lambda\mu\nu = -(a^2b^2c^2+a^2b^2z^2+x^2b^2c^2+a^2c^2y^2) && (2.27) \end{aligned}$$

Now, let us define the following quantities Q, R, η as:

$$\begin{aligned} Q &= \frac{A^2-3B}{9} && (2.28)\\ R &= \frac{2A^3-9AB+27C}{54} && (2.29)\\ \eta &= \arccos\left(\frac{R}{Q^{3/2}}\right) && (2.30) \end{aligned}$$

and η is always real; the value of the ellipsoidal coordinate τ is:

$$\tau = -2\sqrt{Q}\cos\left(\frac{\eta}{3}+\frac{2n\pi}{3}\right) - \frac{A}{3} \quad n = 0,1,2 \tag{2.31}$$

For the oblate case, $a = b$, then $\mu = b^2$ and

$$\begin{aligned} -\tilde{B} &= \lambda+\nu = a^2+c^2+r^2 \\ \tilde{C} &= \lambda\nu = a^2c^2+\omega^2c^2+a^2z^2 \quad \omega^2 = x^2+y^2 && (2.32) \end{aligned}$$

In the general triaxial case, the coordinate surfaces are ellipsoids (λ) and hyperboloid of one (μ) and two (ν) sheets. In terms of ellipsoidal coordinates the quantity $1+m^2(u)$ becomes:

$$1+m^2(u) = \frac{(\lambda+u)(\mu+u)(\nu+u)}{(a^2+u)(b^2+u)(c^2+u)} \tag{2.33}$$

and the expression for the density of our model can be rewritten as:

$$\rho(\lambda,\mu,\nu) = \rho_0\left(\frac{a^2b^2c^2}{\lambda\mu\nu}\right) \tag{2.34}$$

2.3.2 Force components

Following de Zeeuw and Pfenniger (1988), upon transformation of the integral in eq. 2.22 to ellipsoidal coordinates we find that the potential takes the very simple form:

$$\Phi_g = F(\lambda) + F(\mu) + F(\nu) \qquad F(\tau) = \pi G \rho_0 abc \int_0^\infty \ln(\tau + u) \frac{du}{\Delta(u)} \tag{2.35}$$

where we have neglected an additive constant in Φ_g. There is no known closed form for the integral in eq. 2.35; it has to be evaluated by numerical quadrature. Indeed the simple form for Φ_g results in a very simple expressions for the forces, which can be expressed in terms of Carlson's (1979) symmetrize version of the incomplete elliptic integral of the third kind, R_j, as follows:

$$\frac{\partial \Phi_g}{\partial \tau} = F'(\tau) = \frac{2}{3} \pi G \rho_0 abc R_j(a^2, b^2, c^2, \tau) \tag{2.36}$$

For $a = b$ the model defined in eq. 2.18 is stratified on oblate spheroids. In this case $\mu = a^2$ and the ellipsoidal coordinates reduce to prolate spheroidal coordinates (λ, ϕ, ν) with the $z-$axis as symmetry axis. The function $F(\tau)$ still requires numerical integration but its derivative is elementary and is given by:

$$F'(\tau) = \frac{f(\tau) - f(a)}{\tau - a^2} \quad \text{with } f(\tau) = -\frac{2\pi G \rho_0 a^2 c}{\sqrt{\tau - c^2}} \arctan \frac{\sqrt{\tau - c^2}}{c} \tag{2.37}$$

It follows that the force components can be expressed in terms of elementary functions. For $c = b$ the ellipsoids are prolate spheroids. Since $\nu = b^2$ the ellipsoidal coordinates reduces to oblate spheroidal coordinates (λ, μ, ν), that have the $x-$axis as symmetry axis. The expression for the force term becomes:

$$F'(\tau) = \frac{g(\tau) - g(b^2)}{\tau - b^2} \tag{2.38}$$

where

$$g(\omega) = -\frac{2\pi G \rho_0 a b^2}{\sqrt{a^2 - \omega}} \operatorname{arctanh} \left(\frac{\sqrt{a^2 - \omega}}{a} \right) \qquad \omega = \mu, b^2 \tag{2.39}$$

and

$$g(\lambda) = -\frac{2\pi G \rho_0 a b^2}{\sqrt{\lambda - a^2}} \arctan \left(\frac{\sqrt{\lambda - a^2}}{a} \right) \tag{2.40}$$

2.3.3 Potential energy and torques of a precessing ring

The potential energy of a precessing ring with a given radius r in the galaxy potential is:

$$V_g(\theta,\varphi) = \int_{ring} \Phi_g dM = \frac{M}{2\pi}\int_0^{2\pi} P(\lambda,\mu,\nu)d\eta \tag{2.41}$$

and its general increment is

$$\Delta V_g(\theta,\varphi) = \int_{ring} \Phi_g dM = \frac{M}{2\pi}\int_0^{2\pi} \left\{\frac{\partial P}{\partial\lambda}\Delta\lambda + \frac{\partial P}{\partial\mu}\Delta\mu + \frac{\partial P}{\partial\nu}\Delta\nu\right\} d\eta \tag{2.42}$$

where $\Delta\lambda, \Delta\mu, \Delta\nu$ are increments of the ellipsoidal coordinates, and $\partial P/\partial\tau$ are the general force terms respect to them. The torques exert by the potential on the precessing ring can be expressed according to:

$$\frac{\partial V_g(\theta,\varphi)}{\partial(\theta,\varphi)} = \frac{M}{2\pi}\int_0^{2\pi} \left\{\frac{\partial P}{\partial\lambda}\frac{\partial\lambda}{\partial(\theta,\varphi)} + \frac{\partial P}{\partial\mu}\frac{\partial\mu}{\partial(\theta,\varphi)} + \frac{\partial P}{\partial\nu}\frac{\partial\nu}{\partial(\theta,\varphi)}\right\} d\eta \tag{2.43}$$

then, to obtain the torques, we have to evaluate the derivatives of the ellipsoidal coordinates respect to the Euler angles (θ,φ), which can be derived through the equation $m^2(\tau) = -1$.

2.3.4 Derivatives of the ellipsoidal coordinates respect to the Euler angles (θ,φ)

In the general triaxial case, since the radius r of the precessing ring is constant with respect to a variation of (θ,φ), we can derive a relation between the derivatives of the ellipsoidal coordinates, *i.e.*:

$$\lambda+\mu+\nu = a^2+b^2+c^2+r^2 \Longrightarrow \frac{\partial\lambda}{\partial(\theta,\varphi)} + \frac{\partial\mu}{\partial(\theta,\varphi)} + \frac{\partial\nu}{\partial(\theta,\varphi)} = 0 \tag{2.44}$$

In the case of the oblate potential, eq. 2.44 and eq. 2.32 easily leads to:

$$\frac{\partial\lambda}{\partial\theta} = \frac{r^2(a^2-c^2)\sin^2\eta\sin 2\theta}{\nu-\lambda} \tag{2.45}$$

$$\frac{\partial\lambda}{\partial\varphi} = 0 \tag{2.46}$$

$$\frac{\partial\nu}{\partial\theta} = -\frac{\partial\lambda}{\partial\theta} \tag{2.47}$$

In the triaxial case, the evaluation of the derivatives of the ellipsoidal coordinates is more complicated; using the following system of equations

$$\begin{aligned} 0 &= \Delta\lambda + \Delta\mu + \Delta\nu && (2.48)\\ \Delta B &= \Delta\lambda(\mu+\nu) + \Delta\mu(\lambda+\nu) + \Delta\nu(\lambda+\mu) && (2.49)\\ \Delta(-C) &= \Delta\lambda(\mu\nu) + \Delta\mu(\nu\lambda) + \Delta\nu(\lambda\mu) && (2.50) \end{aligned}$$

Rewriting them as

$$\begin{aligned} a_1\Delta\lambda + a_2\Delta\mu + a_3\Delta\nu &= \Delta B && (2.51)\\ b_1\Delta\lambda + b_2\Delta\mu + b_3\Delta\nu &= \Delta(-C) && (2.52) \end{aligned}$$

and with a little algebra we obtain:

$$\begin{aligned} (a_1-a_2)\Delta\mu + (a_1-a_3)\Delta\nu &= -\Delta B && (2.53)\\ (b_1-b_2)\Delta\mu + (b_1-b_3)\Delta\nu &= -\Delta(-C) && (2.54) \end{aligned}$$

Solving the system of equations via substitution, the variation of the ellipsoidal coordinates with respect to an increment of the Euler angles (θ, φ) may be expressed as

$$\begin{aligned} \Delta\lambda &= \frac{(\nu-\mu)(\lambda\Delta B - \Delta(-C))}{\nabla} && (2.55)\\ \Delta\mu &= \frac{(\lambda-\nu)(\mu\Delta B - \Delta(-C))}{\nabla} && (2.56)\\ \Delta\nu &= \frac{(\mu-\lambda)(\nu\Delta B - \Delta(-C))}{\nabla} && (2.57) \end{aligned}$$

where

$$\nabla = \lambda^2(\mu-\nu) + \mu^2(\nu-\lambda) + \nu^2(\lambda-\mu) \qquad (2.58)$$

Since B, C are explicit functions of cartesian coordinates, their increments as the ring tilts can be expressed in terms of $\Delta(z^2)$ and $\Delta(x^2-y^2)$. Recalling that

$$B = a^2b^2 + c^2b^2 + a^2c^2 + a^2(r^2-x^2) + b^2(r^2-y^2) + c^2(r^2-z^2) \qquad (2.59)$$

then

$$\begin{aligned} \Delta B = &-a^2\Delta(x^2) - b^2\Delta(y^2) - c^2\Delta(z^2) - \frac{(a^2+b^2)}{2}\Delta(x^2+y^2)\\ &-\frac{(a^2-b^2)}{2}\Delta(x^2-y^2) - c^2\Delta(z^2) \qquad (2.60) \end{aligned}$$

Since $r^2 = (x^2+y^2)+z^2$ is constant with respect to increments in (θ,φ) coordinates, it implies $\Delta(x^2+y^2) = -\Delta(z^2)$, so:

$$\Delta B = \left[\frac{(a^2+b^2)}{2} - c^2\right]\Delta(z^2) - \frac{(a^2-b^2)}{2}\Delta(x^2-y^2) \tag{2.61}$$

where the coefficient of $\Delta(z^2)$ is a measure of the oblateness, while that of $\Delta(x^2-y^2)$ is related to the non–axisymmetry of the potential. Using the same procedure, from the definition of C

$$-C = a^2b^2c^2 + a^2b^2z^2 + x^2b^2c^2 + a^2c^2y^2 \tag{2.62}$$

we can derive its variation, given by:

$$\Delta(-C) = \left[a^2b^2 - c^2\frac{(a^2+b^2)}{2}\right]\Delta(z^2) - c^2\frac{(a^2-b^2)}{2}\Delta(x^2-y^2). \tag{2.63}$$

The increments in B, C are all functions of the increments in the Cartesian coordinates, which amount at:

$$\Delta(z^2) = -2r^2\sin^2\eta\cos\theta\Delta(\cos\theta) \tag{2.64}$$

for $\Delta(z^2)$, depending just on the θ angle, while x^2-y^2 depends both (θ,φ):

$$\frac{\partial(x^2-y^2)}{\partial(\cos\theta)} = -2r^2\sin\eta[\cos\theta\cos 2\varphi\sin\eta + \sin 2\varphi\cos\eta] \tag{2.65}$$

$$\frac{\partial(x^2-y^2)}{\partial\varphi} = -2r^2[\sin 2\varphi(\cos^2\eta - \cos^2\theta\sin^2\eta) + \cos 2\varphi\cos\theta\sin 2\eta] \tag{2.66}$$

In the prolate case, we have $b = c$, which implies $\nu = c^2$, $\lambda+\mu = a^2+c^2+r^2 = const.$ $\longrightarrow$ $d\lambda = -d\mu$ and

$$(\lambda-\mu)d\mu = (c^2-a^2)d\mu \tag{2.67}$$

which is just function of the x^2 increment with respect to θ,φ,

$$\frac{\partial x^2}{\partial\theta} = -r^2\sin\theta[\cos\theta\sin^2\eta(1-\cos 2\varphi) - \sin 2\varphi\cos\eta\sin\eta] \tag{2.68}$$

$$\frac{\partial x^2}{\partial\varphi} = r^2[\sin 2\varphi(\cos^2\theta\sin^2\eta - \cos^2\eta) - \cos\theta\sin 2\eta\cos 2\varphi] \tag{2.69}$$

and change of the ellipsoidal coordinates can be evaluated.

2.4 Torques as function of the Euler angles (θ, φ)

If we had the potential energy $V_g(\theta, \varphi)$ of the precessing ring, we could express it as a series of spherical harmonics and then use this decomposition for the numerical evaluation of the force terms. The problem with the above class of potential and the pseudo–isothermal one in particular is that the potential energy has not a closed form: we have an analytic form just for the force terms with respect to the ellipsoidal coordinates.

2.4.1 Oblate case

Starting from the oblate case for the matter–density distribution, the axisymmetric properties of the potential implies the following decomposition of the torque with respect to the θ angle

$$\frac{\partial V_g}{\partial \theta} = -\sin\theta \sum_{n=0}^{k} A_n P_n(\cos\theta) \tag{2.70}$$

where P_n are the Legendre polynomials and A_n are the coefficient of the decomposition given as:

$$A_n = \frac{M}{2\pi} \int_0^{2\pi} d\theta P_n(\cos\theta) \int_0^{2\pi} \left\{ \frac{\partial P}{\partial \lambda} \frac{\partial \lambda}{\partial(\cos\theta)} + \frac{\partial P}{\partial \nu} \frac{\partial \nu}{\partial(\cos\theta)} \right\} d\eta \tag{2.71}$$

where $\partial P/\partial \tau$, $(\tau = \lambda, \nu)$ are given by simple analytical functions and the integral is evaluated via Gaussian integration. Since the potential is symmetric with respect to the equatorial plane, it will be function just of even Legendre polynomials: this implies that the force terms would be given by odd Legendre polynomials. The terms in the series of eq. 2.70 are computed till convergence is achieved, *i.e.*:

$$\epsilon = \frac{\left(\frac{\partial V_g}{\partial \theta}\right)_{\theta_0} - \left[-\sin\theta \sum_{n=0}^{k} A_n P_n(\cos\theta_0)\right]}{\left(\frac{\partial V_g}{\partial \theta}\right)_{\theta_0}} \leq 10^{-5} \tag{2.72}$$

for the most flattened halo with $c/a = 0.5$ and $\theta_0 \in [0, \pi/2]$. This condition is fulfilled when the terms are evaluated up to $k = 9$; coefficients A_n are evaluated up to $k = 9$ also for the less flattened case.

2.4.2 Triaxial case

In the more general triaxial case, we have to cope with the dependence of the potential on the φ angle; applying the same procedure to the force terms with respect to the ellipsoidal coordinates as in the oblate case, the coefficients A_n are no longer constants, but functions of φ:

$$\begin{aligned}\frac{\partial V_g}{\partial \theta} &= -\sin\theta[A_0(\varphi) + A_1(\varphi)P_1(\cos\theta) + A_2(\varphi)P_2(\cos\theta) + \\ &\quad \cdots + A_9(\varphi)P_9(\cos\theta)] \qquad (2.73)\\ \frac{\partial V_g}{\partial \varphi} &= [B_0(\varphi) + B_1(\varphi)P_1(\cos\theta) + B_2(\varphi)P_2(\cos\theta) + \\ &\quad \cdots + B_9(\varphi)P_9(\cos\theta)]. \qquad (2.74)\end{aligned}$$

So a suitable orthogonal base should be found in order to project the φ–dependence of the A_n, B_n coefficients. The convergence is reached when the parameter ϵ satisfies:

$$\epsilon = \frac{\left(\frac{\partial V_g}{\partial(\theta,\varphi)}\right)_{(\theta_0,\varphi_0)} - \left[\sum_{n=0,k=0}^{i,g} F_k(\varphi_0)P_n(\cos\theta_0)\right]}{\left(\frac{\partial V_g}{\partial(\theta,\varphi)}\right)_{(\theta_0,\varphi_0)}} \leq 10^{-5} \qquad (2.75)$$

for a strongly triaxial potential, $(b/a = 0.8, c/a = 0.6)$. At first we tried to project the $A_n(\varphi)$, $B_n(\varphi)$ coefficients onto the orthogonal base of the Legendre polynomials $P_i(\cos\varphi)$, but even for $i = 10$, ϵ turns out to be 10^{-2}: this is not a suitable orthogonal set for the above functions. Then we tried with the orthogonal set $\cos 2k\varphi$, $\sin 2k\varphi$, according to:

$$\begin{aligned}A_n(\varphi) &= C_{n0} + C_{n1}\cos(2\varphi) + \cdots + C_{nk}\cos(2k\varphi) + \cdots \qquad (2.76)\\ &+ D_{n0} + D_{n1}\sin(2\varphi) + \cdots + D_{nk}\sin(2k\varphi) + \cdots \qquad (2.77)\\ B_n(\varphi) &= C'_{n0} + C'_{n1}\cos(2\varphi) + \cdots + C'_{nk}\cos(2k\varphi) + \cdots \qquad (2.78)\\ &+ D'_{n0} + D'_{n1}\sin(2\varphi) + \cdots + D'_{nk}\sin(2k\varphi) + \cdots \qquad (2.79)\end{aligned}$$

where C_{nk}, D_{nk} are defined as

$$\begin{aligned}C_{n0} &= \frac{1}{2\pi}\int_0^{2\pi} A_n(\varphi)d\varphi \qquad (2.80)\\ C_{nk} &= \frac{1}{\pi}\int_0^{2\pi} A_n(\varphi)\cos(2k\varphi)d\varphi \qquad (2.81)\end{aligned}$$

$$D_{n0} = 0 \tag{2.82}$$

$$C_{nk} = \frac{1}{\pi}\int_0^{2\pi} A_n(\varphi)\sin(2k\varphi)d\varphi \tag{2.83}$$

and the same definitions hold for C'_{nk}, D'_{nk}, substituting $A_n(\varphi)$ with $B_n(\varphi)$. This time, evaluating the C and the D coefficients up to $i = 4$ gives $\epsilon \leq 10^{-5}$ for $b/a = 0.8, c/a = 0.6$.

The symmetry of the triaxial potential with respect to the principal planes put constraints on the expected values of the coefficients coming from the φ decomposition. The plane $\varphi = \pi/2$, which contains the intermediate and the short axis is the one which contains the long axis orbits and should be a minimum with respect to the φ–component of the torque $\partial V_g/\partial\varphi$, while on the plane $\varphi = 0$, which contains the long and the short axis, we have a maximum for this component of the torque. So we expect a dependence on $\sin(2k\varphi)$ for the φ–component of the torque, while for the θ–component of the torque, $\partial V_g/\partial\theta$, we expect a $\cos(2k\varphi)$ dependence. The computed coefficients agree with these predictions.

We also tested which was the more accurate order of projection, *i.e.* whether it would give better results projecting first the θ–dependence, and then the φ–dependence, or the other way around. We find that the sequence – projection on the Legendre polynomials $P_n(\cos\theta)$ and then the projection of the derived coefficients on the $\sin(2k\varphi), \cos(2k\varphi)$ – is the more accurate: the other way around gave bigger values for ϵ. The dependence of the triaxial potential on the θ angle is stronger than the one on the φ angle: we have to account for the behaviour in θ first and then we can treat the φ dependence as a perturbation.

The computation of the coefficients C_{nk}, D_{nk} and of the primed ones proceeds as follows: the interval $\varphi \in [0, 2\pi]$ is divided in a grid G_φ of 80 points, and for each value $\varphi_\beta \in G_\varphi$, the code evaluates the coefficients $A_n(\varphi_\beta)$, $B_n(\varphi_\beta)$, given by eq. 2.71. The gaussian integration over angle θ at fixed ϕ is done using a modified routine (Subroutine Gauleg) in double precision from Numerical Recipes, and uses a grid G_θ of 100 points in the interval $\theta \in [-\pi, \pi]$. The functions $A_n(\varphi_\beta)$, $B_n(\varphi_\beta)$ are then projected on the trigonometric functions $\sin(2k\varphi)$, $\cos(2k\varphi)$ using the Newton–method for integration.

The biggest time expenses are relative to the first decomposition, since the function to be evaluated for each θ_α, φ_β pair is the average torque along the ring given by eq. 2.43, which requires the evaluation of an elliptic integral. This is done through a standard NAG routine that implements Carlson's algorithm for computing those integrals. Since the force term respect to the elliptical coordinates is proportional to

the elliptic integral $R_j(a^2, b^2, c^2, \tau)$ defined as

$$R_j(a^2, b^2, c^2, \tau) = \frac{3}{2}\int_0^\infty \frac{dt}{(t+\tau)\sqrt{(t+a^2)(t+b^2)(t+c^2)}} \tag{2.84}$$

in our code we tabulate this function at the beginning for values of $\tau \in [0, \lambda_{max}]$ and then we approximate them through a spline function. The number of tabulated points is such that the relative error between $R_j(a^2, b^2, c^2, \tau)$, evaluated at τ_0, and the value of the interpolated spline function at τ_0 is less then 10^{-6}. When the suitable spline function is determined, the first decomposition on Legendre polynomials through Gaussian integration uses the spline approximated function instead of the elliptic integral.

This procedure has sensibly reduced the CPU time required for the evaluation of the coefficients since the NAG routine is called just at the beginning to tabulate its values and then the spline function is computed using a Numerical Recipes routine.

2.5 Gravitational interaction between rings

The mutual gravitational interaction between massive rings can be computed using two different methods which are presented and discussed in the following sections. The first is used in Sparke (1986) and is derived from Binney and Tremaine (1987) p.73, and the second is derived by R. James. The two methods are compared, taking into account the approximation used in our model for the Polar Ring, in order 1) to check the two numerical codes one respect to the other and 2) optimize the CPU time.

2.5.1 L. Sparke formulation of inter–ring forces

Potential energy of two rings with the same lines of nodes

Let us consider a ring of mass m', radius r' and choose carthesian coordinates (ξ, τ, ζ), with ζ perpendicular to the plane of the ring. The potential due to the ring at a point $\vec{x}$ is given by:

$$\Phi(x) = -\frac{GM'}{2\pi}\int_0^{2\pi} \frac{d\eta'}{|\vec{x} - \vec{x'}|} \tag{2.85}$$

where $\vec{x'}$ is a point on the ring. Let the point $\vec{x}$ to have coordinates (ξ, τ, ζ) with $\rho^2 = \xi^2 + \tau^2$ then (Binney & Tremaine 1987, p.73) the potential can be rewritten to:

$$\Phi(x) = -\frac{2GM'}{\pi} \int_0^1 \frac{dx}{\sqrt{(1-x^2)(1-k^2x^2)}} \frac{1}{\sqrt{(\rho + r')^2 + \zeta^2}} \tag{2.86}$$

since in this case $\vec{x'} = (r', \phi', 0)$ (in the ring polar coordinates) and

$$\begin{aligned} |\vec{x} - \vec{x'}|^2 &= \rho^2 + r'^2 - 2\rho r' \cos\phi' + \zeta \\ &= [(\rho + r')^2 + \zeta^2][1 - k^2 \cos^2(\frac{1}{2}\phi')] \end{aligned} \tag{2.87}$$

where

$$k^2 = \frac{4\rho r'}{(\rho + r')^2 + \zeta^2} \tag{2.88}$$

and the variable x of integration is equal to $\cos(\frac{1}{2}\phi')$; the integral over the x variable is the elliptic function $K(k)$. Using the definition of k^2 given in eq. 2.88 we can derive that

$$\rho r'[4 - 2k^2] = (r'^2 + r^2)k^2 \text{ where } r^2 = \rho^2 + \zeta^2 \tag{2.89}$$

and

$$\begin{aligned} \frac{1}{\sqrt{[(\rho + r')^2 + \zeta^2]}} &= \frac{k}{2\sqrt{\rho r'}} = \\ \frac{k}{2} \frac{2\sqrt{1 - \frac{k^2}{2}}}{k\sqrt{r^2 + r'^2}} &= \frac{\sqrt{1 - \frac{k^2}{2}}}{\sqrt{r^2 + r'^2}} \end{aligned} \tag{2.90}$$

hence

$$\Phi(x) = -\frac{2GM}{\pi} \frac{K(k)\sqrt{1 - \frac{k^2}{2}}}{\sqrt{r^2 + r'^2}} \tag{2.91}$$

The mutual potential energy between two rings is found by integrating this potential $\Phi(x)$ over a ring of radius r, with some inclination relative to the first ring.

If the point $\vec{x}$ is on another ring which has inclination θ to the z axis, and the same lines of nodes, then $\vec{x} = (\xi, \tau, \zeta)$ has $\zeta = r\sin(\theta - \theta')\sin\eta$ where η is an angle

round the ring r, and $\rho = r\sqrt{1 - \sin^2\eta \sin(\theta - \theta')}$. The total mutual potential energy due to the gravitational interaction between rings is then:

$$V_m(\theta, \theta') = -\frac{GMM'}{\pi^2} \frac{1}{\sqrt{r^2 + r'^2}} \int_0^{2\pi} K(k)\sqrt{1 - \frac{k^2}{2}} d\eta \tag{2.92}$$

and mutual forces can be found by differentiating V_m with respect to the Euler angles θ, θ', *i.e.*:

$$\dot{P}_{\theta,\theta'} = -\frac{\partial V_m}{\partial(\theta, \theta')} = \frac{GMM'}{\pi^2} \frac{1}{\sqrt{r^2 + r'^2}} \int_0^{2\pi} d\eta \frac{d}{dk}\left[K(k)\sqrt{1 - \frac{k^2}{2}}\right] \frac{\partial k}{\partial(\theta, \theta')} \tag{2.93}$$

Derivative of the elliptic integral K respect to the Euler angles θ, θ'

The explicit form of the integrand in eq. 2.93 can be derived through the following steps. We have

$$\begin{aligned} &\frac{d}{dk}\left[K(k)\sqrt{1 - \frac{k^2}{2}}\right] = \\ &\frac{d}{dk}\left[kK(k)\left(\frac{1}{k^2} - \frac{1}{2}\right)^{1/2}\right] = \\ &\frac{1}{k\sqrt{1 - \frac{k^2}{2}}}\left[\frac{E(k)(1 - \frac{k^2}{2})}{1 - k^2} - K(k)\right] \end{aligned} \tag{2.94}$$

since for the elliptical function $K(k)$ the following relation holds:

$$\frac{d}{dk}(kK(k)) = \frac{E(k)}{1 - k^2} \tag{2.95}$$

The other term $\partial k/\partial(\theta, \theta')$ of the product is given by:

$$\frac{\partial k}{\partial \theta} = \frac{1}{2k} \frac{\partial k^2}{\partial \rho} \frac{\partial \rho}{\partial \theta} \tag{2.96}$$

where

$$\frac{\partial k^2}{\partial \rho} = \frac{(1 - \frac{k^2}{2})^2}{(r^2 + r'^2)} 4r' \tag{2.97}$$

since $\rho^2 + \zeta^2 = r^2$, $\rho d\rho + \zeta d\zeta = 0$ and

$$\frac{\partial \rho^2}{\partial \theta} = -\frac{\zeta}{\rho} r \cos(\theta - \theta') \sin\eta \tag{2.98}$$

so that

$$\frac{\partial k}{\partial \theta} = -\frac{\zeta}{\rho}\frac{1}{2k} 4rr' \frac{(1-\frac{k^2}{2})^2}{(r^2+r'^2)} \cos(\theta-\theta')\sin\eta \tag{2.99}$$

Force terms

Using the set of equations derived in Section 2.5.1, we can derive the torque one ring exerts on the other one, when the two rings have the same lines of nodes. The torque respect to the θ angle of the ring with radius r', mass M' from the ring with radius r and mass M is:

$$\begin{aligned} -\frac{\partial V_m}{\partial \theta} &= \frac{GMM'}{\pi^2} \frac{-4rr'}{(r^2+r'^2)^{3/2}} \cos(\theta-\theta') \int_0^{2\pi} d\eta \frac{\zeta}{\rho} \\ &\quad \frac{(1-\frac{k^2}{2})^{3/2}}{2k^2} \left[\frac{E(k)(1-\frac{k^2}{2})}{1-k^2} - K(k) \right] \sin\eta \end{aligned} \tag{2.100}$$

Looking at the periodicity of the integrand, we have that k depends on η through the variable ρ, which is periodic of period π in η, with $\rho(\theta) = \rho(-\theta) = \rho(\pi - \theta)$, and

$$\frac{\zeta}{\rho} = \frac{r\sin(\theta-\theta')\sin^2\eta}{\rho} \tag{2.101}$$

It appears that the whole integrand repeats in each of the sector $(\frac{n}{2}\pi, \frac{n+1}{2}\pi)$ so the integral has to be performed on the interval $[0, \pi]$ to be sure. The integral becomes:

$$\begin{aligned} -\frac{\partial V_m}{\partial \theta} &= 4\frac{GMM'}{\pi^2} \frac{rr'}{(r^2+r'^2)^{3/2}} \cos(\theta-\theta') \int_0^{2\pi} d\eta \frac{-\zeta\sin\eta}{\rho} \\ &\quad \frac{(1-\frac{k^2}{2})^{3/2}}{k^2} \left[\frac{E(k)(1-\frac{k^2}{2})}{1-k^2} - K(k) \right] \sin\eta \end{aligned} \tag{2.102}$$

If the two rings do not have the same lines of nodes, the angle between the two normals to the respective ring planes is given by:

$$\cos\alpha = \sin\theta\sin\theta'\cos(\varphi - \varphi') + \cos\theta\cos\theta' \tag{2.103}$$

and the forces respect to the Euler angles of the two rings can by expressed as:

$$\dot{P}_{\theta,\theta',\varphi,\varphi'} = -\frac{\partial V_m}{\partial(\theta,\theta',\varphi,\varphi')} = -\frac{\partial V_m}{\partial\alpha}\frac{\partial\alpha}{\partial(\theta,\theta',\varphi,\varphi')} \tag{2.104}$$

When the line of nodes coincide, *i.e.* $\varphi = \varphi'$ we have

$$\frac{\partial V_m}{\partial\alpha} = \frac{\partial V_m}{\partial(\theta-\theta')} = \frac{\partial V_m}{\partial\theta} \tag{2.105}$$

so we can write the dependence of $\partial V_m/\partial\alpha$ according to

$$\begin{aligned} -\frac{\partial V_m}{\partial\alpha} &= -4\frac{GMM'}{\pi^2}\frac{rr'}{(r^2+r'^2)^{3/2}}\cos\alpha\int_0^{2\pi}d\eta\frac{\sin\alpha\sin^2\eta}{\sqrt{1-\sin^2\alpha\sin^2\eta}} \\ &\quad \frac{(1-\frac{k^2}{2})^{3/2}}{k^2}\left[\frac{E(k)(1-\frac{k^2}{2})}{1-k^2}-K(k)\right]\sin\eta \end{aligned} \tag{2.106}$$

where $\zeta = r\sin\alpha\sin\eta$, $\rho^2 = r^2-\zeta^2$ as before. Now $\partial V_m/\partial\alpha$ should multiply $\partial\alpha/\partial\omega$ where $\omega = \theta,\theta',\varphi,\varphi'$ to get the force components respect to the Euler angles:

$$\frac{\partial\alpha}{\partial\theta} = \frac{\sin\theta\sin\theta'\sin(\varphi-\varphi')}{\sin\alpha} \tag{2.107}$$

$$\frac{\partial\alpha}{\partial\varphi} = \frac{\sin\theta\sin\theta'\sin(\varphi-\varphi')}{\sin\alpha} \tag{2.108}$$

and similarly for the primed quantities. Now the force terms can be computed using eqs. 2.104, 2.106 and 2.107.

Numerical evaluation of the mutual force terms

To evaluate numerically the force terms we should perform the integral in the η variable in eq. 2.106, and we have to cope with the fact that the function to be integrated has a bad behaviour near $\eta = 0$, when $r \simeq r$ and $\theta \simeq \theta'$. A part from a multiplicative constant, the integrand behaves as

$$\lim_{\Delta r,\Delta\theta,\eta\to 0}\frac{\partial V_m}{\partial\alpha} = \frac{1}{\Delta\theta\sqrt{2}}\frac{\eta^2}{\frac{\Delta r^2}{r^2\Delta\theta^2}+\eta^2} = f(\eta) \tag{2.109}$$

which peaks at $\eta = 0$, when the ratio $\Delta r/\Delta\theta r$ is small. So we need to space points very closely to $\eta = 0$ when we are in the above conditions and have a compressed scale like $\Delta r/\Delta\theta r$.

Since near $\eta = 0$ the behaviour of the integrated function is given by eq. 2.109, we found that a suitable change of variable to perform the integration is:

$$\int F(\eta)d\eta = \int F(\eta(y))\frac{d\eta}{dy}dy \tag{2.110}$$

where

$$y = \frac{\arctan \eta \dfrac{r\Delta\theta}{\Delta r}}{\arctan \dfrac{\pi r\Delta\theta}{2\Delta r}} \tag{2.111}$$

and the "weight" $d\eta/dy$ is

$$\frac{d\eta}{dy} = \arctan\left(\frac{\pi r\Delta\theta}{2\Delta r}\right)\left[1 + \left(\frac{\eta r\Delta\theta}{\Delta r}\right)^2\right]\frac{\Delta r}{r\Delta\theta} \tag{2.112}$$

(since $d\eta/dy = 1/(dy/d\eta)$ and $dy/d\eta \sim f(\eta)$), so that we can use points evenly spaced in y, and every points in the trapezoidal sum is weighted by the value of $d\eta/dy$. Since the "weight" presents a peak at $\eta = \pi/2$, which becomes important when $\Delta r/r\Delta\theta < \pi/2$, the integration with the $y-$variable is performed up to:

$$y_{max} = \frac{\arctan\left(\eta^* \dfrac{r\Delta\theta}{\Delta r}\right)}{\arctan\left(\dfrac{\pi r\Delta\theta}{2\Delta r}\right)} \tag{2.113}$$

where

$$\eta^* = \frac{\Delta r}{r\Delta\theta\sqrt{2}}\sqrt{\left(\frac{\pi r\Delta\theta}{2\Delta r}\right)} \tag{2.114}$$

After performing the integral in the peak region $[0, y_{max}]$, the variable of integration is changed from y to η, and the newtonian method is used with points evenly spaced in η, up to $\eta_{last} = \pi$.

2.5.2 R. James formulation of inter–ring forces

We try a different approach to the evaluation of inter–ring forces, suggested by R. James in 1984. The rings have radii r_1, r_2, and masses M_1, M_2. We take the $x-$axis O_x in the plane of ring 1, perpendicular to the intersection of the ring planes. The $y-$axis O_y coincides with this intersection, and O_z with the normal to the ring 1 plane. Let's consider a point P on ring 2: the potential generated by a massive ring in a point P is

$$\Phi(P) = \frac{2GM_2}{\pi}\int_0^{\pi/2}\frac{d\eta}{\sqrt{\rho_1^2\cos\eta + \rho_2^2\sin\eta}} \tag{2.115}$$

and ρ_1, ρ_2 are the distances from P to the intersections of the plane through P and the normal to the ring plane, with the ring 1. The radius vector of P is at an angle η_2 (the angle round the ring 2) to the intersection of the ring 2 plane with the $x,z-$plane and denote by α the angle between the ring planes. The coordinate of P are $(r_2\cos\eta_2, r_2\sin\eta_2, 0)$ relative to the cartesian axes in ring 2 plane; in the reference system of ring 1 they becomes $(r_2\cos\eta_2\cos\alpha, r_2\sin\eta_2, r_2\cos\eta_2\sin\alpha)$. The plane through P and O_z, Π_{pz}, is normal to the vector $(-r_2\sin\alpha, r_2\cos\eta_2\cos\alpha, 0)$, and its equation is given by $x\tan\eta_2 = y\cos\alpha$ in the reference frame of ring 1. The plane Π_{pz} intersects ring 1 at

$$\begin{cases} x\tan\eta_2 &= y\cos\alpha \\ z &= 0 \\ x^2+y^2 &= r_1^2 \end{cases} \tag{2.116}$$

Defining $\Lambda = (1+\tan^2\eta_2\sec^2\alpha)^{-1/2}$, so that the coordinates of the intersections can be rewritten to:

$$x_{1,2} = \pm\Lambda r_1 \qquad\qquad y_{1,2} = \pm\Lambda r_1\tan\eta_2\sec\alpha \tag{2.117}$$

the $\pm$ being identical in these expressions. Thus we can rewrite ρ_1, ρ_2 as

$$\begin{aligned} \rho_{1,2}^2 &= (r_2\cos\eta_2\cos\alpha \mp \Lambda r_1)^2 + (r_2\sin\alpha \mp \Lambda r_1\tan\eta_2\sec\alpha)^2 + \\ r_2^2\cos^2\eta_2\sin^2\alpha &= r_1^2 + r_2^2 \mp \frac{2}{\Lambda}r_1r_2\cos\eta_2\cos\alpha \end{aligned} \tag{2.118}$$

and we use the $-$ sign for ρ_1^2 and $+$ for ρ_2^2. Thus we obtain

$$\begin{aligned} &\rho_1^2\cos^2\eta_1 + \rho_2^2\sin^2\eta_1 = \\ &r_1^2 + r_2^2 - \frac{2}{\Lambda}r_1r_2\cos\eta_2\cos\alpha\cos 2\eta_1 \end{aligned} \tag{2.119}$$

Then the potential energy for the ring 2 in the gravitational field of ring 1 is:

$$\Phi_{21} = \frac{2GM_1}{\pi}\int_0^{2\pi} d\eta_2\sigma_2 r_2 \int_0^{\pi/2} \frac{d\eta_1}{\sqrt{r_1^2 + r_2^2 - \frac{2}{\Lambda}r_1 r_2 \cos\eta_2 \cos\alpha \cos 2\eta_1}} \tag{2.120}$$

where $\sigma_2 r_2 = M_2/2\pi$ and

$$\frac{\cos\eta_2 \cos\alpha}{\Lambda} = \cos\eta_2 \cos\alpha\sqrt{1 + \tan^2\eta_2 \sec\alpha} = \sqrt{\sin^2\eta_2 + \cos^2\eta_2 \cos^2\alpha} \tag{2.121}$$

At the end the mutual potential energy becomes:

$$\Phi_{12} = \frac{GM_1M_2}{\pi^2}\int_0^{\pi/2}\int_0^{2\pi} \frac{d\eta_1}{\sqrt{r_1^2 + r_2^2 - 2r_1r_2\cos 2\eta_1}\sqrt{\sin^2\eta_2 + \cos^2\eta_2\cos^2\alpha}} \tag{2.122}$$

note that $(\sin^2\eta_2 + \cos^2\eta_2\cos^2\alpha)$ recapitulates in each η_2 quadrant the values it takes in the first; it is clearly periodic with period π in η_1, and the change $\eta_2 = \pi - \eta_2$ leads no change in the above quantity. Thus:

$$\Phi_{21} = \frac{4GM_1M_2}{\pi^2} = \int\int_0^{\pi/2} d\eta_1 d\eta_2 (r_1^2 + r_2^2 - 2r_1r_2\cos 2\eta_1\sqrt{\cos^2\eta_2\cos^2\alpha + \sin^2\eta_2})^{-1/2} \tag{2.123}$$

The expression is symmetric in r_1, r_2. Writing $r_1 = \gamma r_2$, the potential simplifies to:

$$r_2\Phi_{21} = \frac{4GM_1M_2}{\pi^2}(\gamma^2+1)^{-1/2} f(\beta,\alpha) \quad \text{where} \quad \beta = \frac{2}{\gamma + \gamma^{-1}} \tag{2.124}$$

and

$$f(\beta,\alpha) = \int\int_0^{\pi/2} d\eta_1 d\eta_2 (1 - \beta\cos 2\eta_1\sqrt{\cos^2\eta_2\cos^2\alpha + \sin^2\eta_2})^{-1/2} \tag{2.125}$$

Then the torque on ring 2, sense of α increasing is:

$$\frac{\partial\Phi_{12}}{\partial\alpha} = -4\frac{GM_1M_2}{\pi^2 r^2}(\gamma^2+1)^{-1/2}\frac{\partial f}{\partial\alpha} \tag{2.126}$$

Behaviour of $f(\beta,\alpha)$ near $\alpha = 0$

The dependence on the α angle goes through:

$$\sqrt{\cos^2\eta_2\cos^2\alpha + \sin^2\eta_2} = (1 - \cos^2\eta_2\sin^2\alpha)^{1/2} \tag{2.127}$$

and expanding in powers of $\sin^2\alpha$ it becomes

$$1-\frac{1}{2}\cos^2\eta_2\sin^2\alpha-\frac{1}{8}\cos^4\eta_2\sin^4\alpha- \\ \frac{1}{16}\cos^6\eta_2\sin^6\alpha-\frac{5}{128}\cos^8\eta_2\sin^8\alpha-\cdots \tag{2.128}$$

Thus

$$\left\{1-\beta\cos 2\eta_1\sqrt{\cos^2\eta_2\cos^2\alpha+\sin^2\eta_2}\right\}^{-1/2}= \\ (1-\beta\cos 2\eta_1)^{-1/2}\left(1+\frac{\beta\cos 2\eta_1}{1-\beta\cos 2\eta_1}\frac{1}{2}\cos^2\eta_2\sin^2\alpha+\right. \\ \left.\frac{1}{8}\cos^4\eta_2\sin^4\alpha+\frac{1}{16}\cos^6\eta_2\sin^6\alpha+\frac{5}{128}\cos^8\eta_2\sin^8\alpha+\cdots\right)^{-1/2} \tag{2.129}$$

We write

$$\Gamma=\frac{\beta\cos 2\eta_1}{1-\beta\cos 2\eta_1} \tag{2.130}$$

and expand to obtain:

$$\{\cdots\}^{-1/2}=(1-\beta\cos 2\eta_1)^{-1/2}(1- \tag{2.131}$$

$$\frac{1}{2}\Gamma\left(\frac{1}{2}\cos^2\eta_2\sin^2\alpha+\frac{1}{8}\cos^4\eta_2\sin^4\alpha+\right. \\ \left.\frac{1}{16}\cos^6\eta_2\sin^6\alpha+\frac{5}{128}\cos^8\eta_2\sin^8\alpha+\cdots\right) \\ +\frac{3}{8}\Gamma^2\left(+\frac{1}{4}\cos^4\eta_2\sin^4\alpha+\frac{1}{8}\cos^6\eta_2\sin^6\alpha+\frac{5}{64}\cos^8\eta_2\sin^8\alpha+\cdots\right) \\ -\frac{5}{16}\Gamma^3\left(\frac{1}{8}\cos^6\eta_2\sin^6\alpha+\frac{3}{16}\cos^8\eta_2\sin^8\alpha+\cdots\right) \\ +\frac{35}{128}\frac{1}{16}\cos^8\eta_2\sin^8\alpha) \tag{2.132}$$

We define

$$I_n^m=\int_0^{\pi/2}d\eta_1\frac{\beta^m\cos^m 2\eta_1}{(1-\beta\cos 2\eta_1)^n}\quad\text{and}\quad I_n=I_n^0 \tag{2.133}$$

thus

$$I_n^m=\int_0^{\pi/2}d\eta_1\frac{[1-(1-\beta\cos 2\eta_1)]^m}{(1-\beta\cos 2\eta_1)^n}=I_n-\binom{m}{1}I_{n-1}+\binom{m}{2}I_{n-2}+\cdots \tag{2.134}$$

Thus $(1-\beta\cos 2\eta_1)^{-1/2}$ integrates to $\pi/2I_{1/2}$; the coefficient of $\sin^2\alpha$,*i.e.*:

$$-\frac{1}{4}\frac{\beta\cos 2\eta_1}{(1-\beta\cos 2\eta_1)^{3/2}}\cos^2\eta_2 \tag{2.135}$$

integrates to $-\pi/16I^1_{3/2}$. Following this procedures, it is possible to rewrite $f(\beta,\alpha)$ near $\alpha=0$ as:

$$\begin{aligned} f(\beta,\alpha) &= \frac{\pi}{2}I_{1/2}-\frac{\pi}{16}I^1_{3/2}\sin^2\alpha + \\ &\frac{3\pi}{16}\left(\frac{1}{16}I^1_{3/2}+\frac{3}{32}I^2_{5/2}\right)\sin^4\alpha + \\ &\frac{5\pi}{32}\left(-\frac{1}{32}I^1_{3/2}+\frac{3}{64}I^2_{5/2}-\frac{5}{128}I^3_{7/2}\right)\sin^6\alpha + \\ &\frac{35\pi}{256}\left(-\frac{5}{256}I^1_{3/2}+\frac{15}{512}I^2_{5/2}-\frac{15}{256}I^3_{7/2}+\frac{175}{2048}I^4_{9/2}\right)\sin^8\alpha \end{aligned} \tag{2.136}$$

with the following recurrence relations:

$$I^1_{3/2} = I_{3/2}-I_{1/2} \tag{2.137}$$

$$I^2_{5/2} = I_{5/2}-2I_{3/2}+I_{1/2} \tag{2.138}$$

$$I^3_{7/2} = I_{7/2}-3I_{5/2}+3I_{3/2}-I_{1/2} \tag{2.139}$$

$$I^4_{9/2} = I_{9/2}-4I_{7/2}+6I_{5/2}-4I_{3/2}+I_{1/2} \tag{2.140}$$

The integrals $I_{n+1/2}$ are related to standard elliptic integrals and their numerical evaluations is quite easy.

2.5.3 Comparison between L. Sparke's and R. James' procedures

The goal of performing the numerical evaluation of gravitational forces between rings following both Sparke's and James' methods is to do a double check on the two codes and the optimization of CPU time. The results of the two codes are shown and compared in Fig. 2.1 and 2.2 for different values of the ring radii.

When rings have $r_2 \simeq r_1$ James' approximations gave the proper results up to $\Delta\alpha \simeq 20°$ between the two rings, and deviates strongly for bigger values. The discrepancy reduces when $r_2 \neq r_1$, and $r_2 \gg r_1$, but since we would like to approximate the polar ring around S0 or ellipticals with a series of circular wires, radii of adjacent

rings will be only slightly different, and in this case James' procedure is valid only for angles between rings less than 20°. Since we would like to study the time evolution of precessing rings forming whatever angles between them, Sparke's procedure is adopted, and the self gravity contribution from the ring mass is computed according to the previous discussion.

2.6 Polar Rings in axisymmetric and triaxial potential

Polar rings (PR) around S0 or elliptical galaxies are usually interpreted as material accreted from the outside the host galaxy, remnants of merger with a companion galaxy. These regular tilted structures seems surprising since the axially symmetric S0 or flattened ellipticals (possibly triaxial) would have a galactic gravitational field with a quadrupole component, which causes particle orbits to precess about the pole at a rate which depends on the radius and orbital inclination. Simple estimates suggest that differential precession will destroy the flatness of PR in much less than a Hubble time, implying that the observed structures have been formed only recently. Anyway severely warped PR are not common, and many of them look quite smooth and have time to form the observed stars. In Sparke (1986) the case of long lived PR and tilted dust lanes around an axisymmetric oblate galaxy had been described in detail. We will analyse the properties of PR and their tilts in a axisymmetric oblate pseudo isothermal potential and use these results to make a step behind and analyse the effects of triaxiality on the dynamics of such rings.

2.6.1 Massless PR in a axisymmetric potential

Consider a test particle of small mass m, traveling with angular speed Ω in a nearly circular orbit of radius r which is tilted by an angle θ from the equatorial plane of an axisymmetric galaxy. This orbit precesses about the symmetry axis at a rate

$$\dot{\varphi} \simeq \frac{1}{mr^2\Omega} \frac{\partial V_g(r,\theta)}{\partial(\cos\theta)} \tag{2.141}$$

where V_g is the potential energy of the particle, averaged over the circular orbit (Goldstein 1980). In an oblate galaxy, this rate is negative: it tends to zero as the orbits becomes polar ($\theta \to 90°$), and at large distances. The actual orbit will not be precisely circular and the particle will not move with exactly uniform speed, but

these effects are first order in the galactic oblateness and affect the precession only at a second order. To account for the effect of the flattening Ω is evaluated using the velocity derived from the average radial force along the orbit, *i.e.*:

$$\Omega = \frac{v_c}{r} \quad \text{where} \quad v_c = -r^2 \frac{m}{2\pi} \int_0^{2\pi} \frac{\partial V_g}{\partial r} d\eta \tag{2.142}$$

and η is the angle round the ring. A massless PR can be assembled as a collection of test particles in these tited orbits. If all the ring particles have the same inclinations then by eq. 2.141 those at small radii will regress most rapidly, and the ring will become twisted. Viscosity can act to prevent twisting but causes the ring to settle into the equatorial plane (Tohline *et al.* 1982). If particles at larger radii are in more nearly equatorial orbits, this will tend to equalize the precession rates. Orbits may be adjusted so that the regression rate is kept constant and the ring then precesses as a solid body, instead of being disrupted. Using our method to characterize the torque of the galactic potential in the oblate case the precession rate rewrites to:

$$\dot{\varphi} = -\frac{1}{m v_c r} \sum_{n=0}^{9} A_n P_n(\cos\theta) \tag{2.143}$$

and a PR will precess as a solid body if its inclination varies so that:

$$\sum_{n=0}^{9} A_n P_n(\cos\theta) \propto r \tag{2.144}$$

the closer to polar the inner orbits are the less the ring is warped. This kind of orbits are neutrally stable; if the angular momentum of one particle is increased, its orbits will tilt slightly, shifting the precession speed to slightly different value and this tend to break up the ring. A long lived massless PR about a axisymmetric galaxy, with the same shape at all radii, must be inclined to pole by an amount which varies roughly linearly with distance. If the outer radius of the PR is twice the inner radius, then at the outside its tilt respect to the pole must be double the tilt at the inner edge.

As pointed out by Sparke (1986) in IIZw73 and UGC 7576, this degree of warping may be excluded (Schechter *et al.* 1984). In a gravitational potential with the same shape at all radii, the PRs in those galaxies must be unstable if they are composed of test particles; but in the galaxy NGC 3718 (Schwarz 1985) the disc of neutral hydrogen lies perpendicular to the stellar disc at the centre, and warps by 90° to become nearly equatorial at the edges; its shape resembles that of the massless rings.

2.6.2 Massive rings in oblate potential

Sparke (1986) showed that in an oblate scale free potential of Monet–Richstone and Schechter (1981) the mutual attraction of its particles may force the ring to precess as a unit. We briefly summarize her method, which will be used for PR embedded in an oblate potential and we will extend it to investigate the case of PR embedded in a triaxial pseudo isothermal potential.

In this model the PR is approximated by a pair of thin uniform circular wires mutually tilted but concentric with a slightly oblate potential representing the rest of the galaxy. Let the wires have masses M, M', radii r, $r' > r$, and inclination θ, θ' to the galactic equatorial plane. There is then a mutual potential energy $V_m(r, \theta, r', \theta')$, as well as the energy $V_g(r, \theta)$ due to the galaxy, where V_m and V_g are evaluated according to the methods discussed in Section 2.3 and 2.5. Each wire spins about its own axis at a rate $\Omega(r)$ appropriate to a nearly circular orbit at that radius. We look for a solution in which both wires cross the equator on the same nodal lines, and precess uniformly about the pole. The first wire can now precess at the slow constant rate:

$$\dot{\varphi} = \frac{1}{mr^2\Omega} \frac{\partial}{\partial(\cos\theta)} \{V_m(r, \theta, r', \theta') + V_g(r, \theta)\} \tag{2.145}$$

The rate for the second wire is given by interchanging primed and unprimed quantities. The solid body rotation for the PR requires the two speeds to be equal: this fixes θ' as a function of θ.

Equilibrium configurations

We want the orbits of the two wires model to be adjusted so that the regression rate is kept constant, then the ring precesses as a solid body, instead of being disrupted. We look for equilibria such that the PR appears stationary in a system of reference rotating with an angular velocity equal to the regression rate. This condition is satisfied when for a given precession rate $\dot{\varphi}_0$, the torque with respect to the θ angle is null –no nutation–, *i.e.* $\dot{P}_\theta = 0$ for both the two wires forming the ring. The set of $\theta_{01,02}$, which satisfy $\dot{P}_{\theta 1,2} = 0$ for a given $\dot{\varphi}_0$, represent the equilibrium solution we are looking for.

When the model is extended to include more wires, the equilibrium solution is found by solving $\dot{P}_{\theta i} = 0$ for a given $\dot{\varphi}_0$ simultaneously for each wire. It consists in solving a system of n non–linear equations, where n is the number of wires used to

approximate the PR. The set θ_{0i}, solution of this system of equations, is found numerically using a Numerical Recipes routine for solving systems of non–linear equations.

Stability diagrams

The results for this simple model and the pseudo isothermal potential with axis ratio $a : b : c$ given by $1 : 1 : 0.7$ are illustrated in Fig. 2.4. The curves in the diagram are labelled with the value of the ratio of the combined mass M_R of the wires and the galactic mass (which amounts to 51.16 in arbitrary units) within the outer edge of the ring.

In the stability diagram of Fig. 2.4, for each value of the total ring mass of the two wires model there are two solution curves, the continuous lines on the stability diagram, one belonging to the family A and the other to the family B. The first family (A) passes through $(0°, 0°)$; the inner wire lies closer to the equatorial plane while the other is tipped towards the pole. The second family (B) starts from $(90°, 0°)$: in this case the inner wire is found nearer to the pole, while the outer one is closer to the equatorial plane. In both families, a point (θ, θ') on a continuous line is solution of the system of equations

$$\begin{cases} \dot{P}_\theta &= 0 \\ \dot{P}_{\theta'} &= 0 \end{cases} \tag{2.146}$$

for a given value of $\dot{\varphi_0}$; $\dot{\varphi_0}$ varies continuously along each curve.

The solutions belonging to the family A show that if the total mass of the ring $M_R = M + M'$ falls below a certain value – here is about 0.076 of the galactic mass contained within the ring – then the inner wire has a maximum tilt: as the outer wire becomes more inclined, the inner one falls back to the galactic plane. For larger masses, the angle between the wires reaches a maximum at some intermediate tilt, and then declines as both wires become nearly polar. The equilibria approach the curve $\theta = \theta'$ as the ring mass grows: self gravity becomes so strong that the galactic potential is irrelevant. What happens is that self gravity equalizes the regression rates, the outer wires tends to slow the regression of the inner one, while itself regressing more rapidly than it would in the galactic field alone, so that the PR remains intact.

For the solutions belonging to the family B, if the ring is massless, they are the solution already discussed. In this case the two wires may be quasi coplanar at the pole, but the angle between them increases near the equator: when the outer wire is almost equatorial, the inner wires is about 30° from the equator. As the ring mass grows, the difference in tilts grows larger, since the inner wire tugs on the outer, slowing its regression. If the outer wire is to keep up with the inner one, it must

become more nearly equatorial so as to increase the regression caused by the galactic field. At the same time the inner ring must become more polar, and the effect is stronger, as the ring mass grows. When the ring is heavy enough, the angle θ may exceed 90°; and the inner wire has its sense of spin reversed. If the combined mass M_R exceeds about 0.05 of the galaxy mass, then there are equilibria with the two wires lying on opposite sides of the pole. At larger mass these curves approach the limit $\theta = \theta' + 90°$, with the two wires perpendicular.

Stability in an axisymmetric oblate potential

None of these equilibria is of practical interest unless it is stable: the region of secular stability are limited by the dash dotted lines. A long lived PR corresponds to a steadily precessing equilibrium state E where θ, θ' and the difference $\varphi - \varphi'$ do not change with time: this is a stationary point in the space $(\theta, \theta', \varphi - \varphi', P_\theta, P_{\theta'}, P_-)$, where P_- is defined as the moment conjugate to $\varphi - \varphi'$. E is stable if small excursions from it do not grow large with time. A sufficient condition for stability is that the hamiltonian H is a minimum at E with respect to changes in these six quantities; E is then secularly stable. The regions of secular stability were found by calculating the forces numerically near each point at the equilibrium. If the equations of motion when linearized about E have exponentially growing solutions, then E must be unstable.

When self gravity is absent, the solutions are neutrally stable. When self gravity is present, equilibria with the two wires almost coplanar are stable: the mutual potential energy is near a minimum there. Some states in which the inner ring lies near the equatorial plane are also stable: these are related to warped galaxy disk. There are many unstable solutions: the equilibria of sequence B (with the inner ring more nearly polar) are unstable close to the pole: an example of time evolution of these unstable solutions is shown in Fig. 2.5.

Stable solutions with both wires near the pole are of the greatest observational interest. These have $\theta' > \theta$, so that the outer wire is more steeply inclined and $\theta \simeq \theta'$, *i.e.* the ring is not greatly warped. Such stable equilibria exist only when the total ring mass is larger that the critical value $m^* = 0.05$. For masses just above m^*, there are stable equilibria near the pole (see Fig. 2.6) and near the equatorial plane, but not at intermediate angles: if the mass is larger (than about 0.076 of the galaxy mass) there are solutions at any angle to the pole.

2.6.3 Massive rings in triaxial potentials

We investigate what happens to the solutions A and B for a massive two wires model when we go to a triaxial potential. We will treat models of triaxial potentials with different axis ratios but with the same total mass inside the outer radius of the ring, *i.e.* with $b_{tr}c_{tr} = b_{obl}c_{obl} = 0.7$. We will present in some detail models with triaxial potentials with axis ratios $1 : 0.95 : 0.7368$ and $1 : 0.9 : 0.7777$, the latter being the model with an higher degree of triaxiality. We will discuss what happens to a PR structure when it is embedded in a stationary triaxial potential or in a tumbling triaxial configuration.

Stationary triaxial potential

In a stationary triaxial potential, as the ring precess due to the $\partial V_g/\partial \cos(\theta)$ component of the torque, it is influenced by the $\partial V_g/\partial\varphi$ component as well, so P_φ is no more a constant of motion. In this case, the condition $\dot{P}_\theta = 0$ does not imply that $\dot{\varphi}_n$ will be constant for each wire in the model, because $\partial V_g/\partial\varphi$ is different from zero.

As stated before, a stable polar ring should appears stationary in a steadily rotating frame, but this condition cannot be fulfilled since $\partial V_g/\partial\varphi \neq 0$. Here again solutions are found with all wires having the same line of nodes[1] and with the $\partial V_m/\partial\varphi$ component equal zero for the inter-ring part of the potential. This means $\partial V_g/\partial\varphi = 0$: so either $\varphi_i = 0$ or $\pi/2$. The system of equations which determine the set of θ_{0i}, look the same as in the oblate potential.

In Fig. 2.7 the initial conditions for a 10–wires model are found by looking for a configuration where $\dot{P}_{\theta i} = 0$, $\theta_{i+1} > \theta_i$, $\varphi_i = \pi/2$ and the precession rates $\dot{\varphi}_i$ all equal to $\dot{\varphi}_0$, where $\dot{\varphi}_0$ is a given value. As wires precess, the PR starts to wobble, it reached the pole after 10 orbits, and it reverses it sense of precession. The structure oscillates between θ_{start} and $90° + \theta_{start}$, while changing its sense of precession every ~ 10 orbits. This behaviour does not satisfy our stability criteria.

In a stationary triaxial potential, stationary configurations for polar rings are not possible. The only way such a structure may persist is if the triaxial potential is tumbling around its minor axis and the wires have a precession rate (given by 2.145) equal to the angular velocity of tumbling.

[1]In principle there could be other type of equilibria, with wires having different lines of nodes

Tumbling triaxial potential

In a tumbling triaxial potential, solutions of the families A and B are found for $\varphi = \pi/2$, *i.e.* the plane where anomalous retrograde orbits (Schwarzschild 1982) intersects the plane containing the long and the middle axis. This plane, as described in Section 2.4.2, is a minimum for the $\partial V_g/\partial\varphi$ and solutions found according to previous prescription may be stationary, as the figure tumbles. In the case of a rotating triaxial potential, the precession rate of the ring has to be equal to the figure tumbling speed (Schwarzschild 1982, van Albada 1987) : so for a given model of the potential we will not have continuous lines in the diagram θ, θ', as for the oblate case, but just single solutions for each value of the ring mass (see Fig. 2.8). In Fig. 2.8 crosses indicate solutions found for precessing rings with different masses, embedded in a triaxial potential with axis ratios 1 : 0.95 : 0.7368, at three different values of the figure tumbling speed $\dot{\varphi} = -3 \cdot 10^{-2}$, $-1.5 \cdot 10^{-2}$, $-8 \cdot 10^{-3}$; the full triangles indicate solutions for precessing rings with different masses, embedded in a triaxial potential with axis ratios 1 : 0.9 : 0.7777 for four different values of the figures tumbling speed $\dot{\varphi} = -3 \cdot 10^{-2}, -1.5 \cdot 10^{-2}, -8 \cdot 10^{-3}, -4 \cdot 10^{-3}$ in arbitrary units. Solutions associated with higher precession rates (in absolute values) are found near the origin, and those lower values are found further out, near $(0°, 90°)$, $(90°, 90°)$ and $(90°, 0°)$.

Since we are interested in stable equilibria, we investigate the regions of secular stability for both triaxial potentials, using the figure tumbling rate as a free parameter. The stability regions for the families A and B in Fig. 2.9 and 2.10 are delimited by dash dotted lines. In both diagrams, the stability regions are found by evolving numerically the equilibrium configurations for the two wires model up to 140 orbits: those which remain unchanged are considered "secularly stable". Secularly stable solutions are those where the hamiltonian of the system has a minimum: *i.e.* the hessian of the second derivatives of the hamiltonian with respect to the phase space coordinates has all positive eigenvalues.

Going from oblate to the rotating triaxial case we found that the stability region for the family B is different: in the limit of $M_R \to 0$ the solutions with $\theta > \theta'$ become stable, close to the pole and at intermediate angles. These solutions are related to the anomalous retrograde orbits, which turn out to be stable also if we include the gravitational interaction between them. Regarding the A family, stable solutions with both wires near the pole exist for both triaxial potentials, and less mass is required: in the triaxial potential with axis ratios 1 : 0.9 : 0.7777, solutions with both wires near the pole are found already when the total ring mass is 0.05. The stability regions around $(0°, 90°)$ and $\theta' \sim \theta$ appear narrower than the corresponding ones in the oblate case: the triaxial model with the same mass as the oblate case has a "weaker" torque

with respect to θ, θ' $(\partial V/\partial \cos(\theta, \theta'))$, and solutions for family A have smaller $\Delta\theta$.

Equilibria belonging to families A and B are found also at $\varphi = 0$: the concentric wires intersect the equatorial plane of the potential at the $x-$axis, along the plane were $\partial V_m/\partial\varphi$ has its maximum. The equilibria there are unstable: Fig. 2.11 shows the evolution for a solution belonging to the A family, which starts to wobble after 5 orbits and the sense of precession is reversed after $\sim$ 10 orbits.

2.7 Conclusion

We have shown that polar ring around an axisymmetric oblate galaxy or a rotating triaxial system can be stabilized by self gravity, so that it is long lived. These stable rings curve towards the pole in both cases, and the total ring mass must exceed a minimum value, which increases using potential with less degree of triaxiality: in the cases we investigated we found that the minimum mass needed to find solutions near the pole is 0.05 for a rotating potential with the highest degree of triaxiality (axis ratios 1 : 0.9 : 0.7777), and should exceed this value in the corresponding oblate case. When the ring mass is too light, PR in the oblate case can be stable only near the equator plane, while in the rotating triaxial potential it can be stable also away from it, if the ring structure is bending towards the equator. These solutions found in the limit of ring mass going to zero, are related to the anomalous retrograde orbits of tumbling triaxial potentials (Schwarzschild 1982). Somewhat heavier rings may be stable either near the pole or near the equator, but not at intermediate angles. As its mass increases, the ring becomes more nearly planar, though tilted away from the pole. The amount of curvature decreases as 1) the ring becomes more nearly polar, 2) the ring becomes narrower, and 3) the ring mass increases in proportion to the galactic quadrupole moment for the oblate case, following eq. 6 of Sparke (1986). Referring to the stability diagrams for the cases presented above, the massive polar rings in rotating triaxial potentials are less warped than those in the oblate model, with the same total mass. Simulations of the time evolution of massive polar ring embedded in a stationary triaxial potential show that it is unstable: after few orbits, the ring begins to wobble between the initial value θ_{start} and $90° + \theta_{start}$, while its sense of precession is reversed.

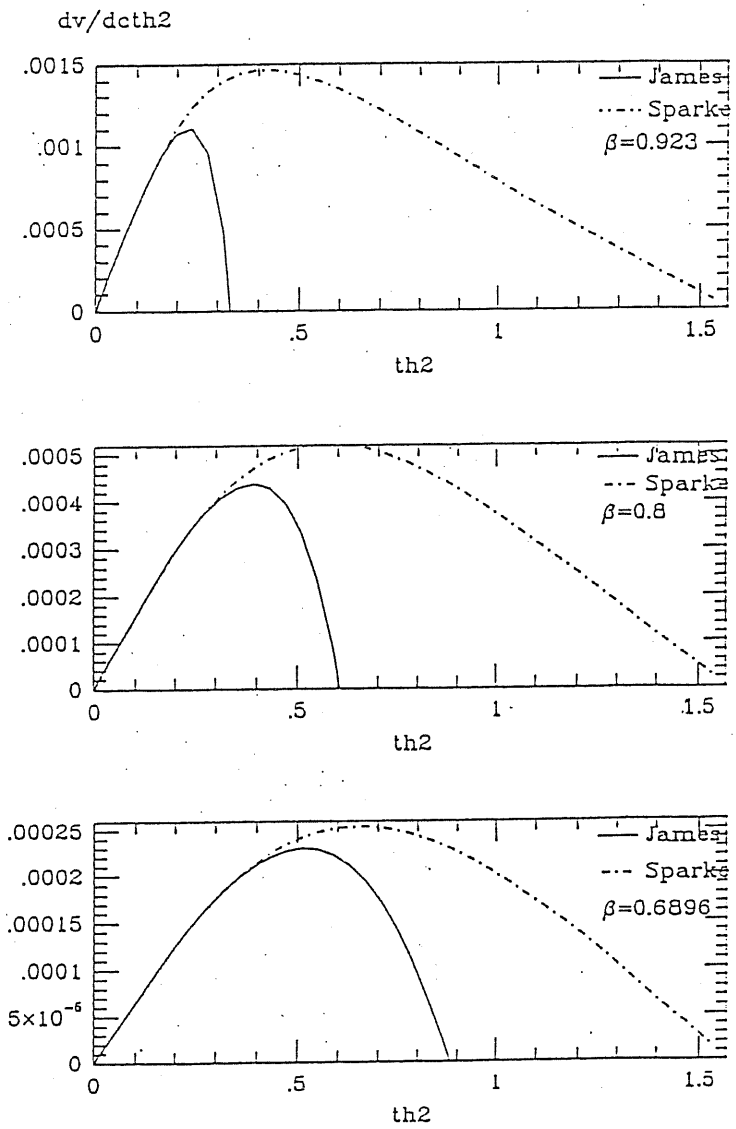

Figure 2.1: Comparison between Sparke's and James' procedures: torques between rings are computed for different values of ring radii, $r_2 = 1.5r_1$, $2r_1$, $2.5r_1$, *i.e.* $\gamma = 0.66, 0.5, 0.4$. For each γ, the torque $\partial V_m/\partial \cos(\theta_2)$ is plotted against θ_2 values. For $r_2 = 1.5r_1$, James' method holds for $\theta_2 \leq 0.2$ rad, and deviates strongly for larger values.

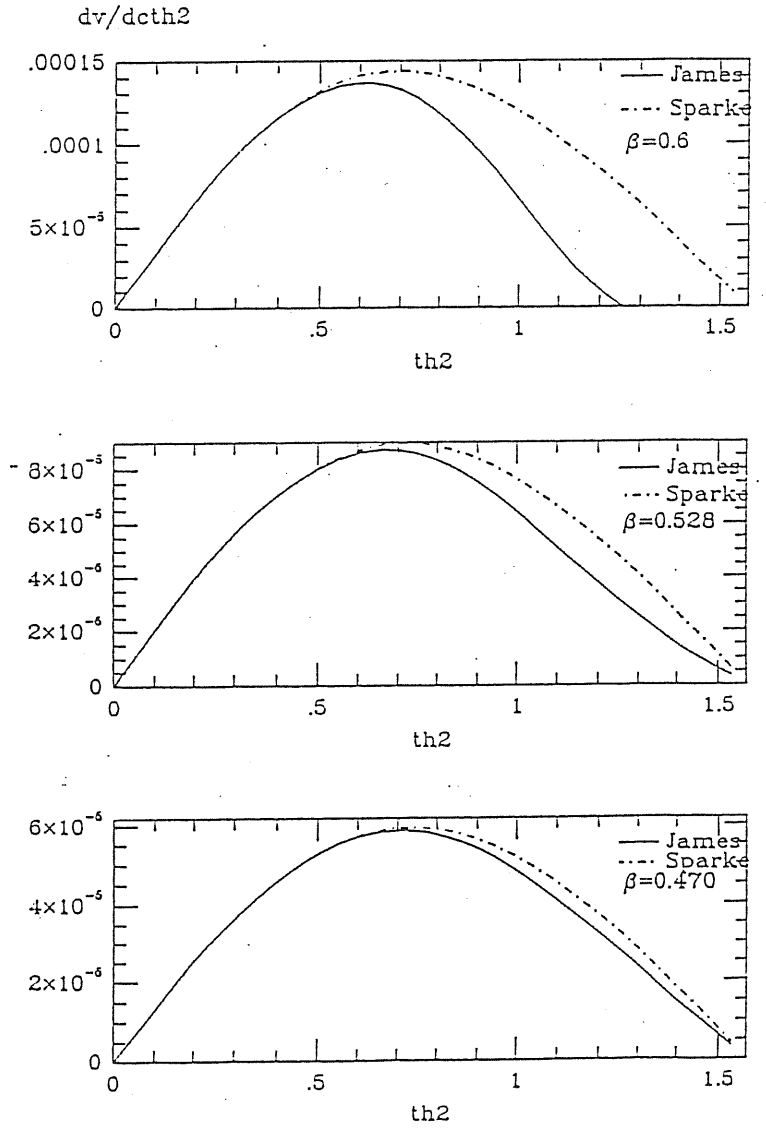

Figure 2.2: Comparison between Sparke's and James' procedures: torques are computed for $r_2 = 3r_1, 3.5r_1, 4r_1$. The discrepancy between the predicted values decreases as the difference in radius increases.

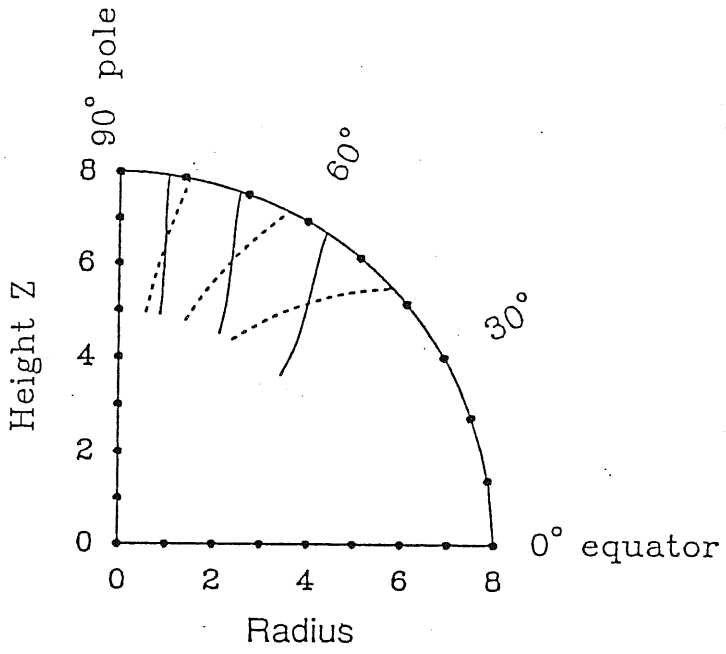

Figure 2.3: Sections through three massless polar rings (dotted lines); this shows how the orbital plane of the ring particles must vary with radius to maintain a constant precession speed about the z–axis. The potential is the pseudo isothermal potential with a total mass of 51.16 in arbitrary units inside the outer radius (8, inner radius is 5) of the PR, and axis ratios 1 : 1 : 0.7. The continuous lines show sections through three self–gravitating rings with the same precession speeds and total mass equal 4.5.

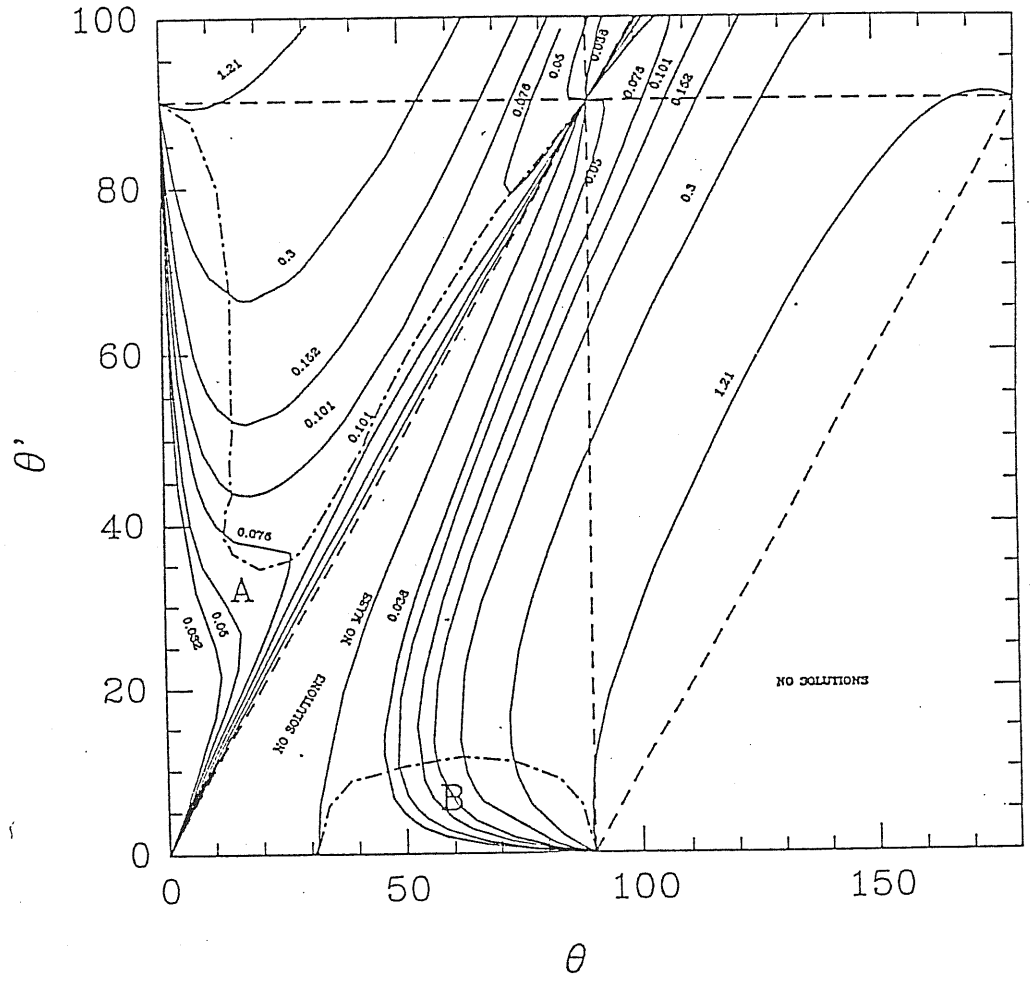

Figure 2.4: The inclination θ, θ' for a pair of steadily–precessing concentric massive wires in an oblate potential with axis ratios 1 : 1 : 0.7. When $\theta = \theta'$, the wires are coplanar but tilted with respect to the galaxy. Along each curve the mass of wires is kept constant, while the precession rate varies. Regions of secular stability are limited by dash dotted lines; the two families A and B are discussed in the text. The wires have radii of 5.75 and 7.25 units with the same mass (*i.e.* with linear density decreasing as $1/r$). Curves are labelled with values of the ratio between the combined mass M_R of the wires and the galactic mass of 51.16 within the outer edge of the ring.

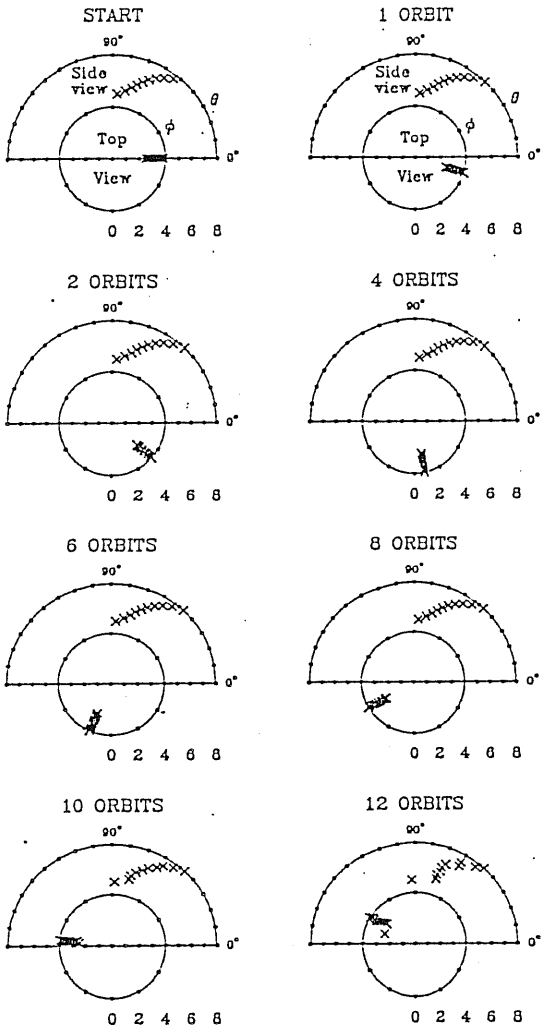

Figure 2.5: Time–development of a B solution near to the pole, followed using a 10–wires model, in an oblate potential (axis ratios 1 : 1 : 0.7). At each stage, the outer semi–circular frame shows the inclination θ; the equator is horizontal, and the radial scale is marked. The inner frame shows the azimuth φ, with the radial scale shrunk to half that of the outer frame. The total mass of the ring is 0.3. Times are given in terms of the orbital period P at radius 6.37, in the middle of the ring, which is 15 time units. To start, the precession speed at each radius was chosen so that the torque in the θ direction was zero (no nutation). The ring is unstable and after 13 orbits it breaks in sub–ring.

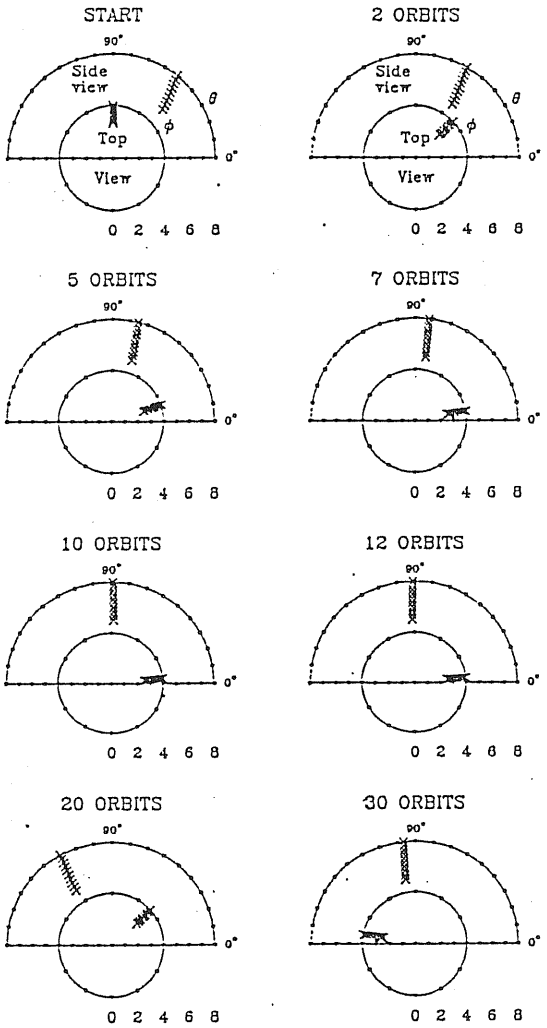

Figure 2.7: Time-evolution of a polar ring, followed using a 10–wires model. The potential is stationary and has axis ratios given by 1 : 0.9 : 0.7777; the ring has a mass of 3.9. The structure wobbles and is sense of precession changes due to the $\partial V_g/\partial\varphi$ torque of the galactic potential.

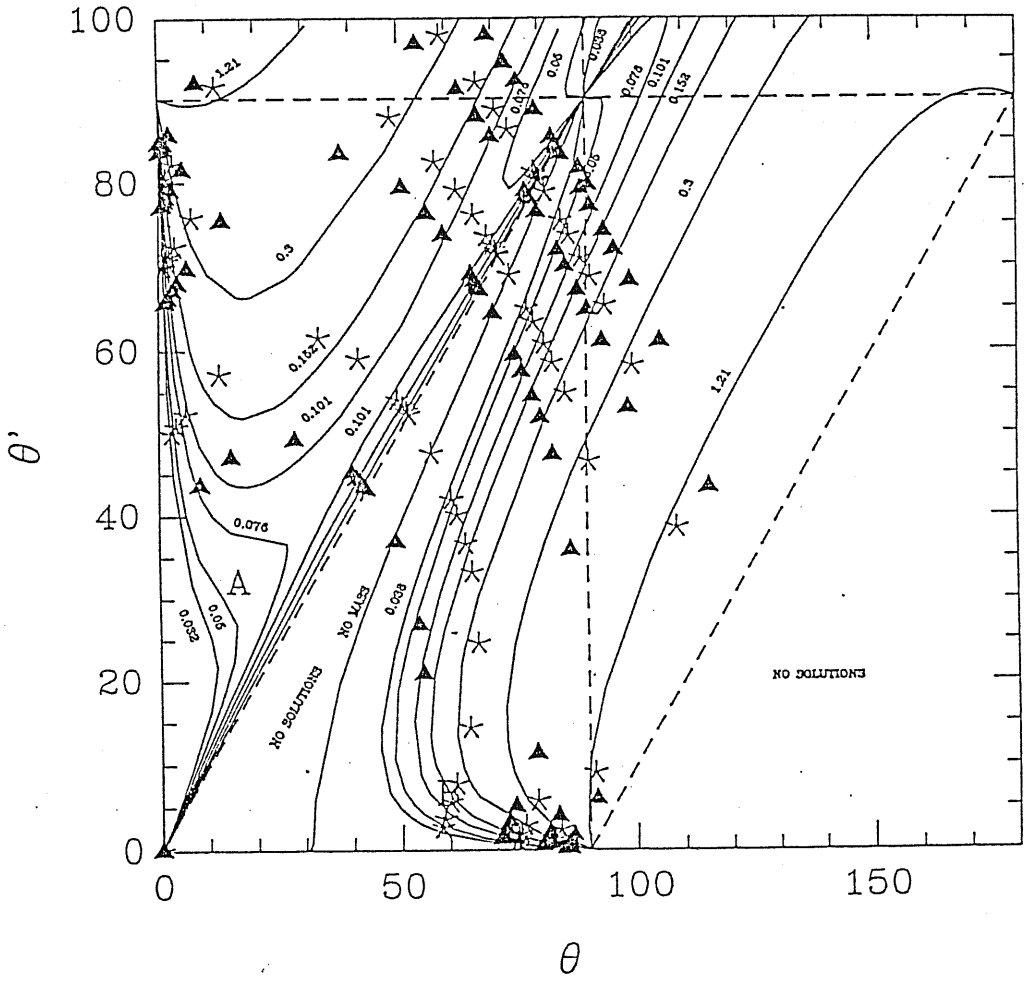

Figure 2.8: Comparison between the solutions θ, θ' found for a pair of steadily–precessing concentric massive circular wires in an oblate potential with axis ratio 1 : 1 : 0.7, and for tumbling triaxial potentials with axis ratios 1 : 0.95 : 0.7368 (crosses) and 1 : 0.9 : 0.7777 (full triangles) respectively. The precession rates, at which solutions are found, are described in the text. Solutions for the first case (crosses) are nearer to the equilibria computed for the oblate case.

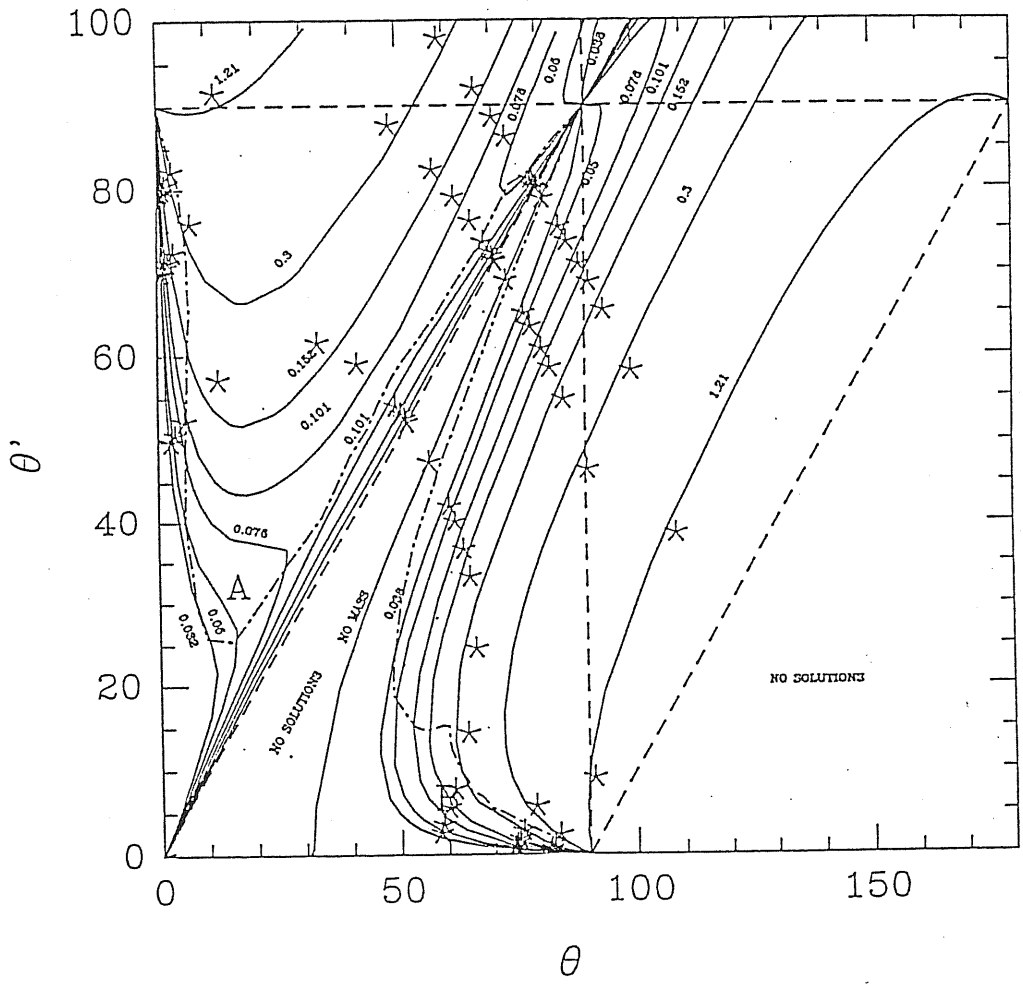

Figure 2.9: Comparison between the solutions θ, θ' found for a pair of steadily–precessing concentric massive circular wires in an oblate potential (axis ratios 1 : 1 : 0.7) and for a rotating triaxial potential with axis ratios 1 : 0.95 : 0.7368 (crosses). Going from the origin to outwards, solutions are found for different values of the figure tumbling speed, $\dot{\varphi} = -3 \cdot 10^{-2}, -1.5 \cdot 10^{-2}, -8 \cdot 10^{-3}$ respectivcly. The dash dotted lines indicates regions were stable solutions are found.

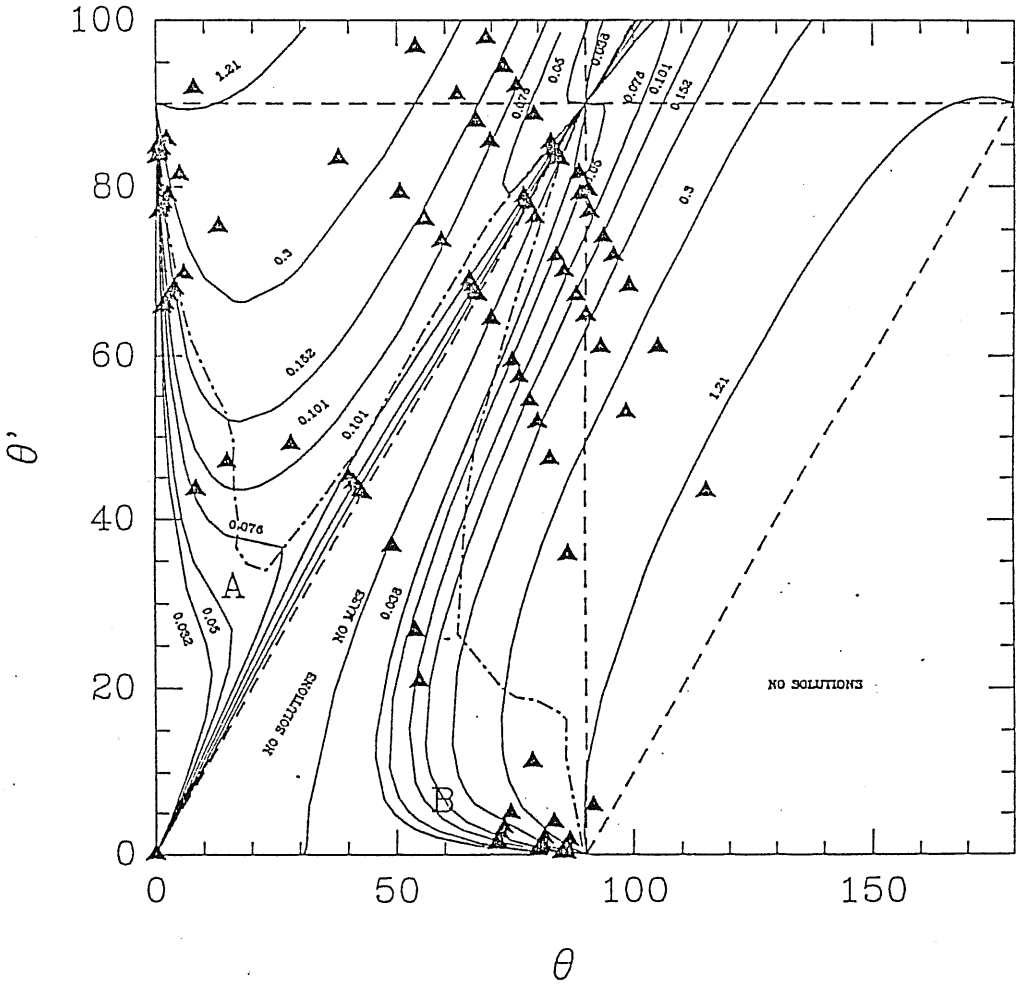

Figure 2.10: Comparison between the solutions θ, θ' found for a pair of steadily–precessing concentric massive circular wires in an oblate potential (axis ratios 1 : 1 : 0.7) and for a tumbling triaxial potential with axis ratios 1 : 0.9 : 0.7777 (full triangles). Solutions are found for different values of the figure tumbling speed, $\dot{\varphi} = -3 \cdot 10^{-2}, -1.5 \cdot 10^{-2}, -8 \cdot 10^{-3}, -4 \cdot 10^{-3}$ respectively. The dash dotted lines indicates regions of stable solutions.

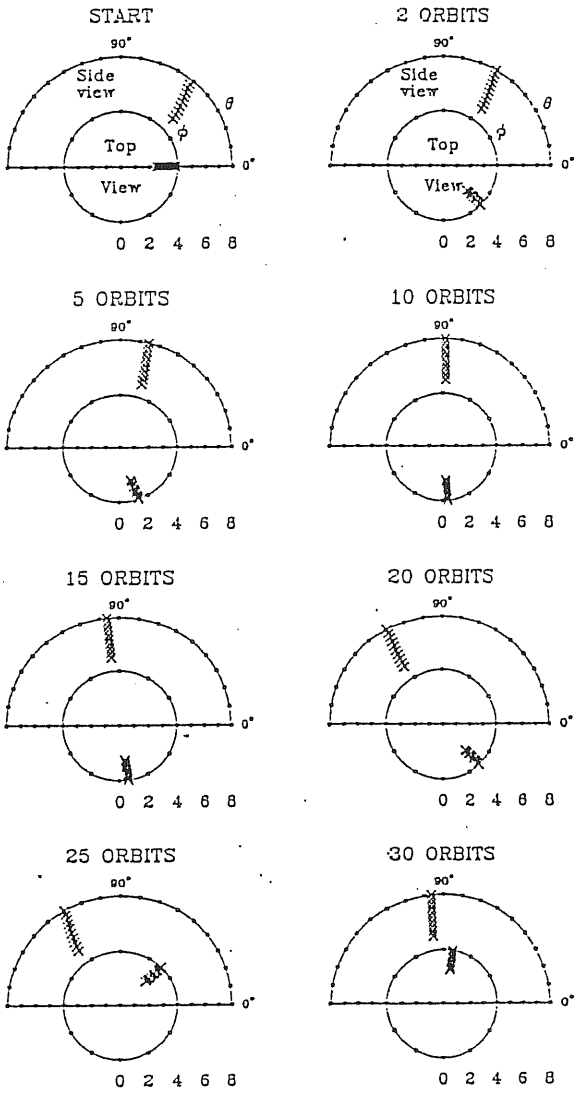

Figure 2.11: Time-evolution for an equilibrium (A) found at $\varphi_i = 0$, $i = 1, \cdots, 10$ and with a ring mass equal to 2.17 (in arbitrary units). The potential has axis ratios equal to 1 : 0.9 : 0.7777, and a total mass inside the outer ring radius of 51.16 (in arbitrary units). The ring starts to wobble and its sense of precession is reversed after $\sim$ 10 orbits.

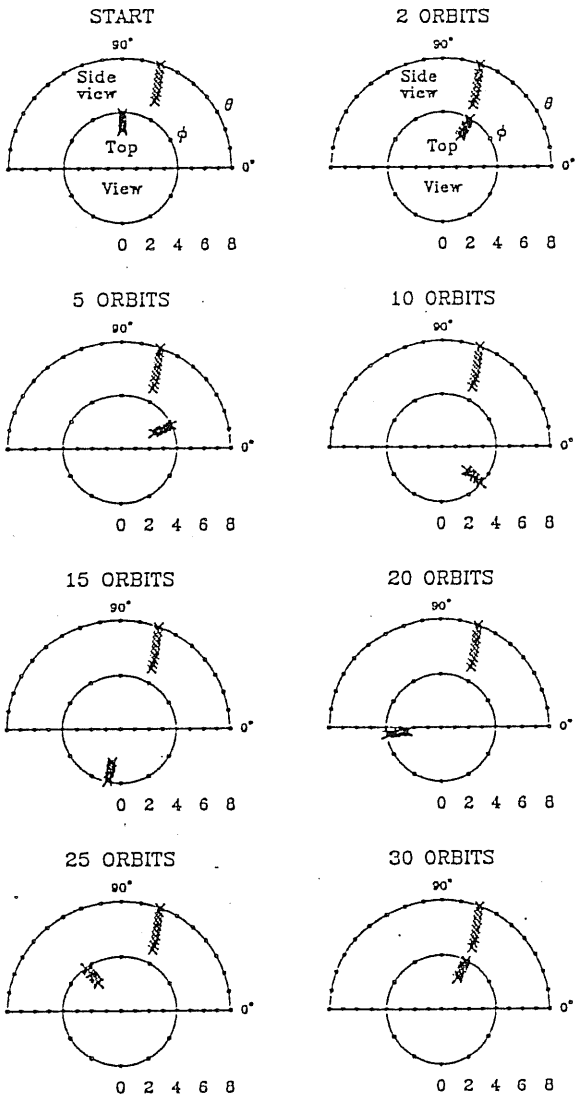

Figure 2.12: Time–evolution for an equilibrium (A) found at $\varphi_i = \pi/2$, $i = 1, \cdots, 10$ and with a ring mass equal to 3.9. The potential is the same as in the previous figure. The solution is stable, and the wires precess all with the same speed.

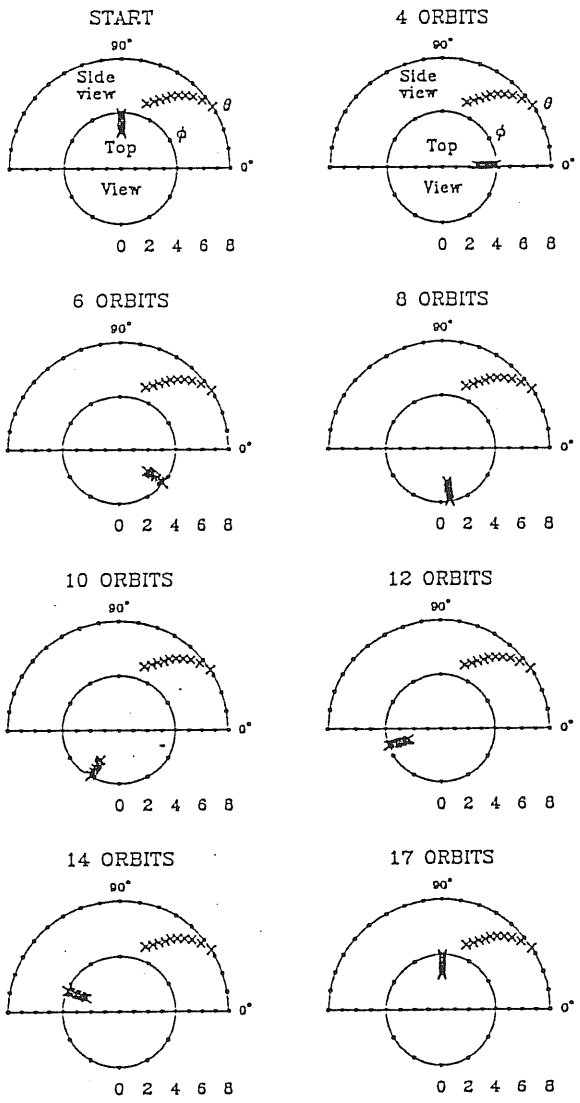

Figure 2.13: Time–evolution for an equilibrium (B) found at $\varphi_i = \pi/2$, $i = 1, \cdots, 10$ and with a ring mass equal to 0.3. The solution is stable, and the wires precess all with the same speed.

Bibliography

[1] Binney J., Tremaine S., 1987, Galactic Dynamics, Princeton Univ. Press

[2] Carlson B.C., 1979, Num. Math. 33, 1

[3] Chandrasekhar S., 1969, Ellipsoidal Figures of Equilibrium, New Haven, Yale Univ. Press.

[4] de Zeeuw T., 1985, MNRAS 216, 273

[5] de Zeeuw T., Pfenniger D., 1988, MNRAS 235, 949

[6] Goldstein H., 1980, Classical Mechanics, 2^{nd} ed., Addison–Wesley, Reading, Massachusetts.

[7] Monet D.G., Richstone D.O., Schecter P.L., 1981, ApJ 245, 454.

[8] Sackett P.D., Sparke L.S., 1990, ApJ 361, 408

[9] Schecter P. L., Sancisi R., van Woerden H., Lynds C. R., 1984, MNRAS 208, 111

[10] Schwarz U.J., 1985, A&A 142, 273

[11] Schwarzschild M., 1982, ApJ 263, 599

[12] Schweizer F., Whitmore B.C., Rubin V.C., 1983, AJ 88, 909

[13] Sparke L.S., 1986, MNRAS 219, 657

[14] Tohline J.E., Simonson G.F., Caldwell N., 1982, ApJ 252, 92

[15] van Albada T.S., 1987, N-Body Simulations of Elliptical Galaxies. In: de Zeeuw T. (ed.) Proc IAU Symp. No. 127, Structure and Dynamics of Elliptical Galaxies. Reidel, Dordrecht, p. 291

Chapter 3

Kinematical properties of warped structure

3.1 Introduction

Recent observations indicate that many galaxies possess warped gas planes, detectable not only at 21 cm (Sancisi 1976) but also in visible light. The categories of polar ring S0s (Schweizer *et al.* 1983, Whitmore *et al.* 1990) and dust-lane ellipticals (Bertola & Galletta 1978, Hawarden *et al.* 1981) now include many tens of galaxies with such structures. The gas kinematics of these galaxies require more complex hypotheses than the conventional approach of coplanar, circular orbits for the gas motions, and need new approaches, which are simple enough to be used in the analysis of many different systems.

This chapter, we will show how is possible, with a simple geometric and kinematic model, to reproduce and interpret spectroscopic observations of gas in galaxies with warped structures. Contrary to the usual analysis, which makes use of 2-D maps of the velocity field (by 21 cm or Fabry-Perot data), this model only needs photometric data and long-slit spectra to put constrain to the warps.

We apply this procedure to several specific cases, to show the flexibility of our model, which can be used in two different ways. The first is an heuristic approach, in the sense that it can give a better estimate of the rotation curve and thus of the galaxian mass. The second is to check the predictions of N-body codes (Steiman–Cameron & Durisen 1988) or dynamical code for precessing rings (Sparke 1986) with regard to producing warped and twisted gas structures.

3.2 The model

3.2.1 The geometry of the stellar structure

To describe the geometry of a warped structure in a galaxy, we need to first establish a reference frame. We use the equatorial plane of the stellar structure as a reference. In the case of a disk galaxy, whose structure is presumed to be axisymmetric (oblate) or only slightly triaxial (Magrelli *et al.* 1992), this plane is clearly identified by the galaxy symmetry plane. Hereafter, we call this plane the (x', y') plane in the reference frame $\hat{O}X'Y'Z'$, and call (y'', z'') the plane of the sky in the reference frame $\hat{O}X''Y''Z''$. In the latter, the line-of-sight corresponds to the X'' axis and is inclined with respect to the galaxy reference frame by the zenith- and the azimuthal- angles i and ϕ. These angles correspond to the inclination ($i = 90°$: edge-on) and the P.A. of the line-of-nodes, referred to an arbitrary "north" direction.

The oblate case is the most widely adopted in the literature as a model of the stellar structure of polar-ring galaxies. Assuming a mean disk flattening of c/a=0.25 (Sandage *et al.* 1970), the mean observed axial ratio of the galaxy isophote $(b/a)_{oss}$ gives the inclination i of the galaxy through the equation:

$$\sin i = \sqrt{\frac{1-(b/a)^2_{oss}}{1-(c/a)^2}} \tag{3.1}$$

In elliptical galaxies, where the intrinsic shape is probably triaxial, an accurate analysis of the isophote parameters (apparent axial ratios and position angles of the isophote major axes) is needed to determine the range of the intrinsic axial ratios c/a, b/a and the orientation angles i, ϕ with respect to the line-of-sight, where the equatorial plane is generally defined as that which contains the major and intermediate axes (a, b), with the X' axis of the reference system oriented toward the galaxy major axis. The relations between the intrinsic parameters and the observed ones for the general case of triaxial structure have been discussed by several authors (Stark 1977; Binney 1978; Benacchio & Galletta 1980; Galletta 1983). Applications to real galaxies are presented by Williams (1981), and Caldwell (1984),

3.2.2 Definition of the ring reference frame

Once the parameters of the host galaxy are defined, it is possible to deduce the inclination angle(s) of the gas structures (*i.e.* rings or disks). In this work, we approximate

the warped gas distribution with a series of circular wires. This choice is justified by the facts that closed orbits in the meridian plane of a flattened potential are only slightly elliptical (Williams & Schwarzschild 1978), and in the case of the gas the collisions between clouds tend to circularize the orbits, driving the gas to closed paths, and smoothing the velocities along each orbit.

In our model, the N circular wires are inclined with respect to the galaxy equatorial plane (x', y') by an angle δ_n, $n = 1, ..., N$. We assume these wires have radii r_n on the (x, y) plane in a reference frame of orthogonal axes $\hat{O}XYZ$. The line of nodes of the n-th ring, defined as the intersection between the ring plane and the equatorial plane of the galaxy, forms an angle α_n with respect to the X' axis of the galaxy reference frame.

The matrix which transforms the coordinates of the ring from its reference frame to the sky frame is given by[1]:

$$x''_i = R''_{ij} x_j \quad (x_i = x, y, z) \tag{3.2}$$

where

$$R''_{ij} = R'_{ik} R_{kj}, \tag{3.3}$$

R'_{ik} is the rotation matrix from $\hat{O}X'Y'Z'$ to $\hat{O}X''Y''Z''$ and R_{kj} is the transformation from the ring reference system to the galaxy one. The coefficients of the global transformation for each ring are:

$$\begin{array}{lcll}
R''_{11} & = & \cos(\alpha_n - \phi)\sin i \cos\delta_n + \sin\delta_n \cos i & = \tilde{R}''_{11} \\
R''_{12} & = & -\sin(\alpha_n - \phi)\sin i & = \tilde{R}''_{21} \\
R''_{13} & = & -\cos(\alpha_n - \phi)\sin i \sin\delta_n + \cos i \cos\delta_n & = \tilde{R}''_{31} \\
R''_{21} & = & \sin(\alpha_n - \phi)\cos\delta_n & = \tilde{R}''_{12} \\
R''_{22} & = & \cos(\alpha_n - \phi) & = \tilde{R}''_{22} \\
R''_{23} & = & -\sin(\alpha_n - \phi)\sin\delta_n & = \tilde{R}''_{32} \\
R''_{31} & = & -\cos(\alpha_n - \phi)\cos i \cos\delta_n + \sin i \sin\delta_n & = \tilde{R}''_{13} \\
R''_{32} & = & \sin(\alpha_n - \phi)\cos i & = \tilde{R}''_{23} \\
R''_{33} & = & \cos(\alpha_n - \phi)\cos i \sin\delta_n + \sin i \cos\delta_n & = \tilde{R}''_{33}
\end{array} \tag{3.4}$$

where $\tilde{R}''_{ij}$ is the matrix for the inverse transformation, i.e.

$$x_i = \tilde{R}''_{ij} x''_j \tag{3.5}$$

[1]We omit the index n, referring to the n-th ring, in the R_{ij} coefficients for simplicity

The *P.A.* of the major axis of the projected ellipses is obtained by the system of equations:

$$\begin{cases} x'' = 0 & \text{Sky plane} \\ z = 0 & \text{Ring plane} \end{cases} \tag{3.6}$$

since the ring is contained by the (x, y) plane of its reference frame. The equation for this plane in the sky frame becomes

$$z = \tilde{R}''_{31}x'' + \tilde{R}''_{32}y'' + \tilde{R}''_{33}z'' = 0 \tag{3.7}$$

So the P.A. on the sky, referred to an arbitrary "north" direction, of the n-th ring major axis, γ_n, is given by

$$\tan\gamma_n = \frac{z''}{y''} = -\frac{R''_{23}}{R''_{33}} = \frac{\sin(\alpha_n - \phi)\sin\delta_n}{\cos(\alpha_n - \phi)\cos i \sin i + \sin i \cos\delta_n} \tag{3.8}$$

The axial ratio $(b/a)_{ring}$ of the circular ring, projected on the sky, is easily derived by the relation: $b_{ring} = a_{ring}\cos i_n$, where $\cos i_n$ is the direction cosine between the line-of-sight X'' and the ring axis Z. From the [3.3], and the coefficients of the [3.4], we have:

$$(b/a)_{ring} = R''_{13} = -\cos(\alpha_n - \phi)\sin\delta_n \sin i + \cos i \cos\delta_n \tag{3.9}$$

and we have a closed system of equations which, for each wire, determines $\alpha_n - \phi$ and δ_n.

3.2.3 Projection of warped rings or disks

In reality it is hard to derive the orientation angles and flattening for each wire, because the single gas rings appear smeared in a smooth and slightly irregular structure. To compare the observed morphology of the rings with that obtained from the model we need to produce a synthetic image of the warped structure as it would appear on the sky at different line-of-sight orientations with respect to the galaxy.

In this synthesis every ring with a radius r_n is described by the intersection of the sphere

$$x^2 + y^2 + z^2 = r_n^2 \tag{3.10}$$

and the plane $z = 0$. Changing to the sky frame, the equation of the sphere is invariant, i.e.

$$x^2 + y^2 + z^2 = x''^2 + y''^2 + z''^2 = r_n^2 \tag{3.11}$$

while the equation for the $z = 0$ plane is given by equation [3.7], from which we have

$$x''^2 = y''^2 R''^2_{23} R''^{-2}_{13} + z''^2 R''^2_{33} R''^{-2}_{13} + 2R''_{23} R''_{33} R''^{-1}_{13} y'' z'' \tag{3.12}$$

which, substituted into equation [3.11], gives the projected ellipse

$$y''^2(R''^2_{13} + R''^2_{23}) + z''^2(R''^2_{13} + R''^2_{33}) + 2y''z''R''_{23}R''_{33} = r_n^2 R''^2_{13} \tag{3.13}$$

which can be directly compared with the shape of the ring as visible on the images. All the figures presented in this chapter have been obtained with this procedure.

3.2.4 Projection of the velocities

The previous equations describing the intrinsic structure of the rings and the underlying galaxy have involved photometric analysis only. If we want to compare the observed kinematics to the model we need to derive the projected velocities on the sky.

Since the n-th wire is confined in its (x, y) plane, i.e. $z = 0, \dot{z} = 0$, we can consider the motion in this plane introducing the polar coordinates (r, β, z). So we have

$$\begin{cases} \dot{x} &= \dot{r}\cos\beta - r\dot{\beta}\sin\beta \\ \dot{y} &= \dot{r}\sin\beta + r\dot{\beta}\cos\beta \end{cases} \tag{3.14}$$

where $\dot{r}$ is the expansion- or contraction- velocity within the galaxy and $\dot{\beta}$ is the angular velocity. The velocity vector in the sky frame would be given by

$$\begin{cases} \dot{x}'' &= R''_{11}\dot{x} - R''_{12}\dot{y} \\ \dot{y}'' &= R''_{21}\dot{x} + R''_{22}\dot{y} \\ \dot{z}'' &= R''_{31}\dot{x} + R''_{32}\dot{y} \end{cases} \tag{3.15}$$

Since x'' is the line of sight, the radial motion of the point y'', z'' with respect to the observer is:

$$\dot{x}'' = \dot{r}(R''_{11}\cos\beta + R''_{12}\sin\beta) + r\dot{\beta}(R''_{12}\cos\beta - R''_{11}\sin\beta) \tag{3.16}$$

which can be rewritten as

$$\dot{x}'' = V_{exp}(R''_{11}\cos\beta + R''_{12}\sin\beta) + V_{rot}(R''_{12}\cos\beta - R''_{11}\sin\beta) \tag{3.17}$$

V_{exp} and V_{rot} are the radial and tangential velocities with respect to the galaxy nucleus; these are generally functions of the distance r' from the nucleus, the azimuthal angle β and the height z' on the galactic equatorial plane. In the case of elliptical orbits, V_{exp} represents the radial component of the orbital velocity, while for circular orbits, as so far assumed in our model, V_{exp}=0.

3.3 Kinematical predictions

We can use the above treatment in different ways: if we have a good image of rings or warped disks, we can apply equation [3.13] to build a computer-generated image of the structure by varying the quantity of warping and/or twisting until a satisfactory reproduction of the main features is reached. At this point, assuming a typical rotation curve, we can extract the projected velocities on the sky. As we shall show, once a possible intrinsic structure is defined, complex assumptions about the rotation curves are not necessary and very simple trends (rigid then flat rotation) are able to reproduce complex observed velocity curves.

The specific approach to modelling the galaxy follows three steps: 1) Deduction of the inclination i from the apparent flattening $(b/a)_{obs}$ of the stellar component; 2) Evaluation of the warping (δ_n, n=1,..,N) and the twisting (α_n, n=1,...,N) using images of the warped structure in visible or narrow-band wavelengths (we conservatively assume a smooth trend $\Delta\delta, \Delta\alpha$ with radius), and 3) Deduction of the intrinsic rotation curve V_{rot} by means of comparison with the observed gas rotation curves. Steps 2) and 3) are iterated until a result consistent with all the observations is found.

Another use of this procedure is to verify dynamical models already presented in the literature, which predict both warped configuration in space and the gas rotation curve. The orientation angles (δ_n, α_n) and the rotation curve V_{rot} then arise from the assumption of a particular potential. With our model, we can compare the observed velocities curves at any position angle on the sky with those expected in the assumed configuration. The procedure to describe the system is similar to the one already discussed, but the parameters in steps 2) and 3) are assumed from a dynamical model and tested by comparison with the observed rotation curves.

To summarize, a single galaxy can be described in our model by the inclination angle(s) and mean intrinsic flattening(s) of its stellar body. Its warped structure will be identified by a set of orientation angles (δ_n, α_n) for N wires of radius r_n and by the kinematical function $V_{rot}(r_n)$.

3.3.1 Applications

To show the versatility of our approach we will produce a model for a suitable candidate: a galaxy taken from the literature whose morphology clearly indicates the presence of a warped structure, and the rotation curves at different P.A.s show peculiar characteristics. One of these nicely warped galaxies is NGC 660 (Benvenuti *et al.* 1976), shown in Fig. 3.1.

It has a bright stellar body, quite elongated with multiple dust lanes lying on its apparent major axis and at higher inclinations on one side of the stellar body. The central bright region is circled by a luminous ring–like feature, which resembles the polar rings visible around several S0s (like NGC 4650A). In fact, this galaxy is included in the Polar Ring Catalogue of Whitmore *et. al.* (1990), belonging to the class of system for which the external ring material may eventually evolve in a polar structure.

The rotation curves derived from the 21-cm emission of HI has been published by Gottesman and Mahon (1990). These curves are determined for a $P.A. = 46°$, the apparent major axis of the stellar component, and at $P.A. = 173°$, close to the elongation of the gaseous structure. The first rotation curve shows the presence of HI clouds at different projected velocities. Two features can be recognized: fast rotation at about 140 km s^{-1} and a second one whose projected velocities are nearly zero with respect to the systemic velocity. A third feature is visible in the center of the galaxy, where HI absorption against the strong central continuum source produces a vertical strip in the velocity diagram. This absorption profile is also present in the second rotation curve together with the faster rotating component of the HI gas. To model this galaxy we calculated the inclination of the stellar body by measuring its apparent flattening. This produced $b/a_{oss} = 0.3$, suggesting an inclination of $i = 80°$. Morphological considerations, based on the position of the nucleus with respect to the innermost horizontal dust lane, as it appears in our plates, led us to assume an inclination $i = 100°$, symmetric to the previous one, but on the other side of the galaxy equatorial plane. Thirty wires are used to approximate the gaseous structure; they are lying on the equatorial plane and their inclination increases monotonically from $\delta_1 = 0°$ up to $\delta_{30} = 63°$. The last angle is computed from eqns. 3.8 and 3.9 using the apparent $b/a_{ring} = 0.36 \pm 0.06$ and $\Delta P.A. = 55° \pm 2°$, derived for the elongated gas structure. The line–of–nodes is the same for every wire, and forms an angle of $\alpha = -60°$. These choices reproduce both the inner horizontal dark lanes, (see Fig. 3.2), and the outer inclined one. In addition, it produces the luminous, elongated gas structure. This configuration also reproduces the observed HI rotation curve (Fig. 3.3) assuming a very simple rigid+constant velocity curve, with a turning point at $\sim 4''$ and a maximum value (in the plateau) of 140 km s^{-1}.

The galaxy is assumed to be transparent at the HI wavelength (unlike the optical lines), so all the wires crossed by the line–of-sight produce velocities in our plots, even if hidden by the galaxy or the warped structure itself. The double rotation curve visible in Fig. 3.3 is the result of this transparency. The good agreement between morphology, rotation and model can be judged from these figures.

Another application of this modelling procedure is demonstrated using by the twisted and warped gas structure observed in the barred S0 galaxy NGC 2217 (Bettoni *et al.* (1990). In this case, the gas disk is perpendicular to the bar axis (assumed to be the x' axis) in the inner parts, where $\delta_1 = 0°$, and $\alpha_1 = 90°$, and it settles down towards the equatorial plane of the galaxy, with the last wire at $\delta_{30} = 90°$. The maximum twisting due to differential precession of the wire is $\Delta\alpha = 18°$. The general appearance of the gas structure and the good agreement of the projected emission–line rotation curve with the one produced by the model are shown in Fig. 3.4.

A detailed discussion of this galaxy with the application of this model, is presented by Bettoni *et al.* (1990).

This modelling procedure has also been used to verify the warped structure predicted by a dynamical code for the polar ring galaxy AM 2020–504. The geometry of the warped gas was obtained using the physical parameters derived from observations and the assumed underlying potential (Arnaboldi *et al.* 1992): the warped model reproduces the S–shape of the polar ring and the observed gas rotation curves showed in Fig. 3.5 for two different slit positions along the edges of the ring, no twisting is needed to reproduce the observed velocities. The procedure shows also that a coplanar circular corona produces rotation curves (dashed lines in Fig. 3.5) which are not in agreement with the observed ones.

3.4 Conclusions

We have shown with three different applications to real galaxies how a simple model can reproduce very complex structures, both in the morphology and the rotation curves of peculiar systems. In each case presented, the strange features in the gas rotation curves were due to projection effects and do not imply intrinsic non–circular motions.

In particular, NGC 660, a galaxy where the gas, probably acquired from the outside at $\delta \sim 60°$, is smeared in annulus which have settles down to the galaxy equatorial plane in the inner parts, is shown to have a rotation curve which is a simply rigid + constant rotation.

AM 2020-504 belongs to the same category as NGC 660, having accreted gas from the outside, and our model indicates that the accreted gas may possibly be in a warped stationary structure.

Finally, we infer from the gas kinematics of NGC 2217 that it has a warped and twisted gas disk. Here the elongated barred potential and the oblate potential of the disk are responsible of the distortion of the gas structure.

Obviously all these observed structures can be reproduced by complicated non circular orbits or more complex modelling, but the advantage of our model is that it is based on a minimum number of assumptions.

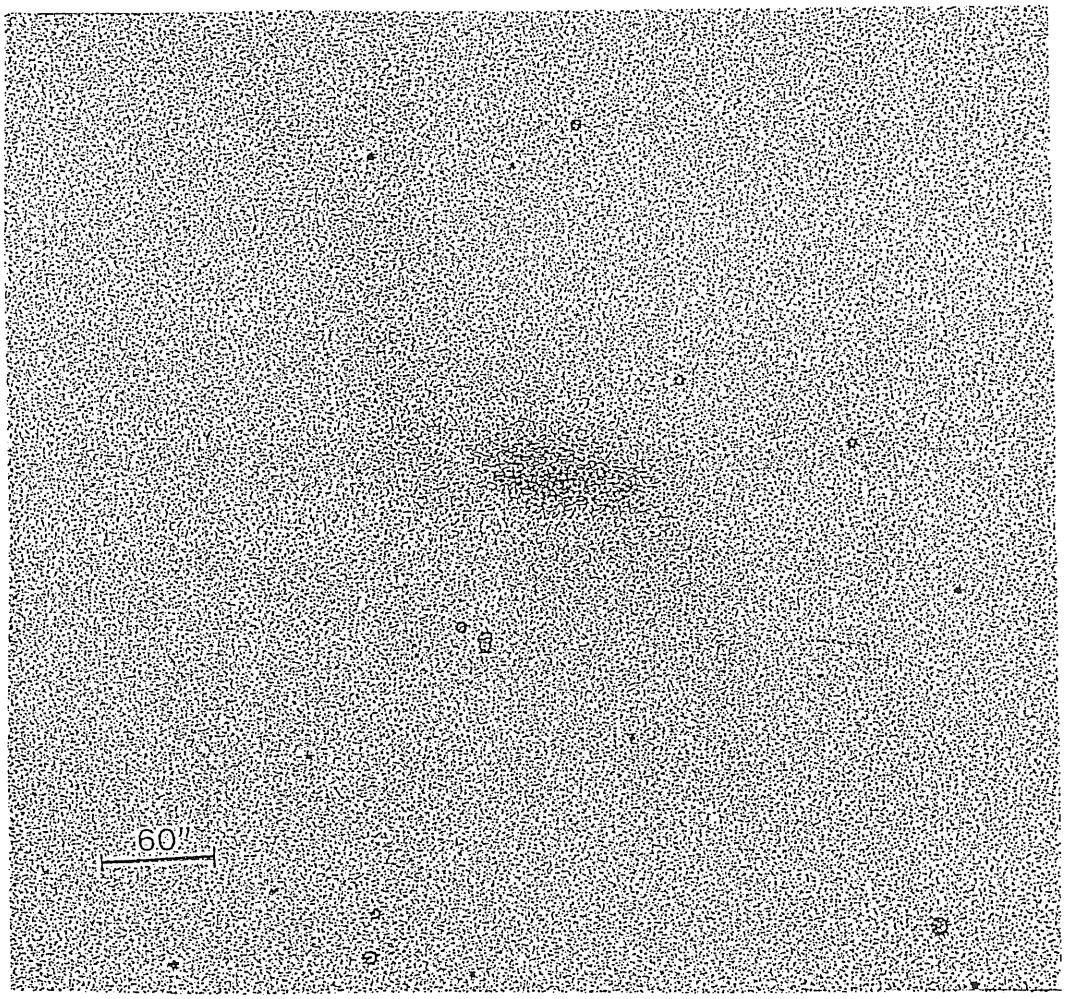

Figure 3.1: Blue image of NGC 660 taken at the 1.22cm telescope of Asiago, showing the many dust lanes and the faint warped structure. (Exposure 105^{min}).

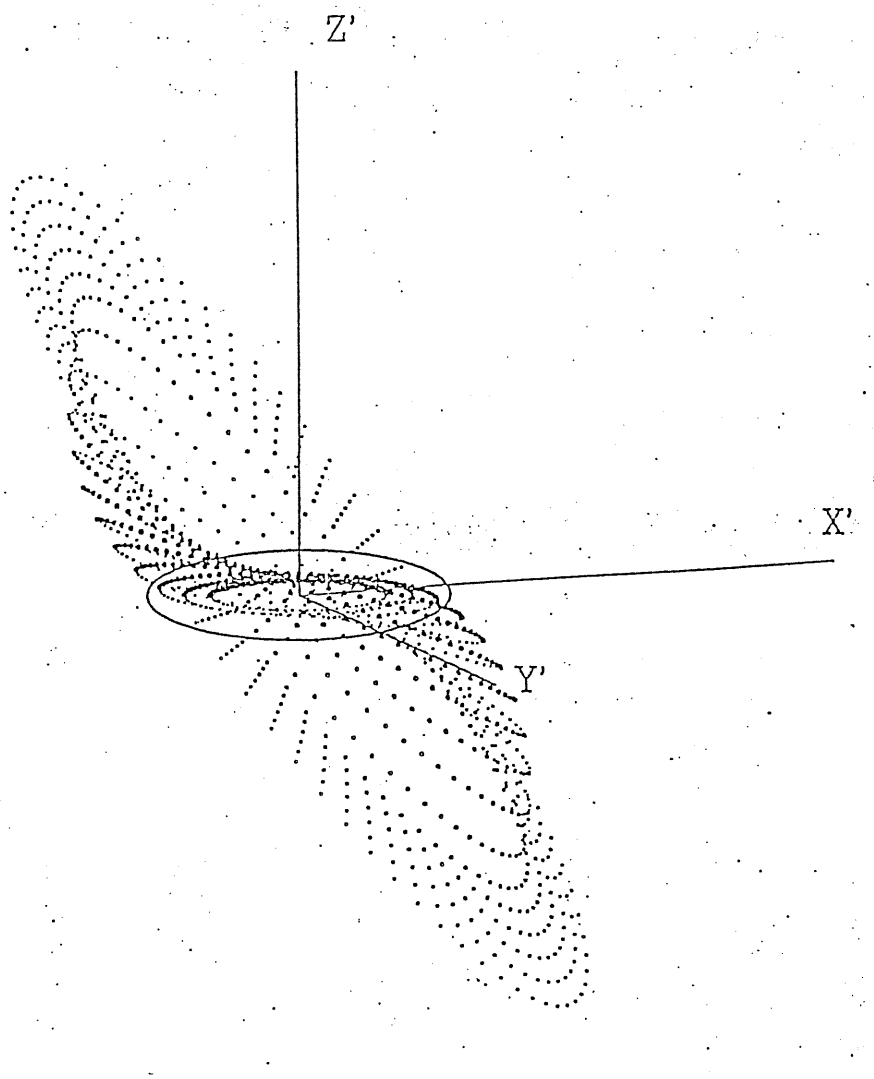

Figure 3.2: Computer-simulated image of NGC 660, projected at the same orientation angles of the real galaxy. The front side and the innermost portion of the rings is plotted with heavier dots.

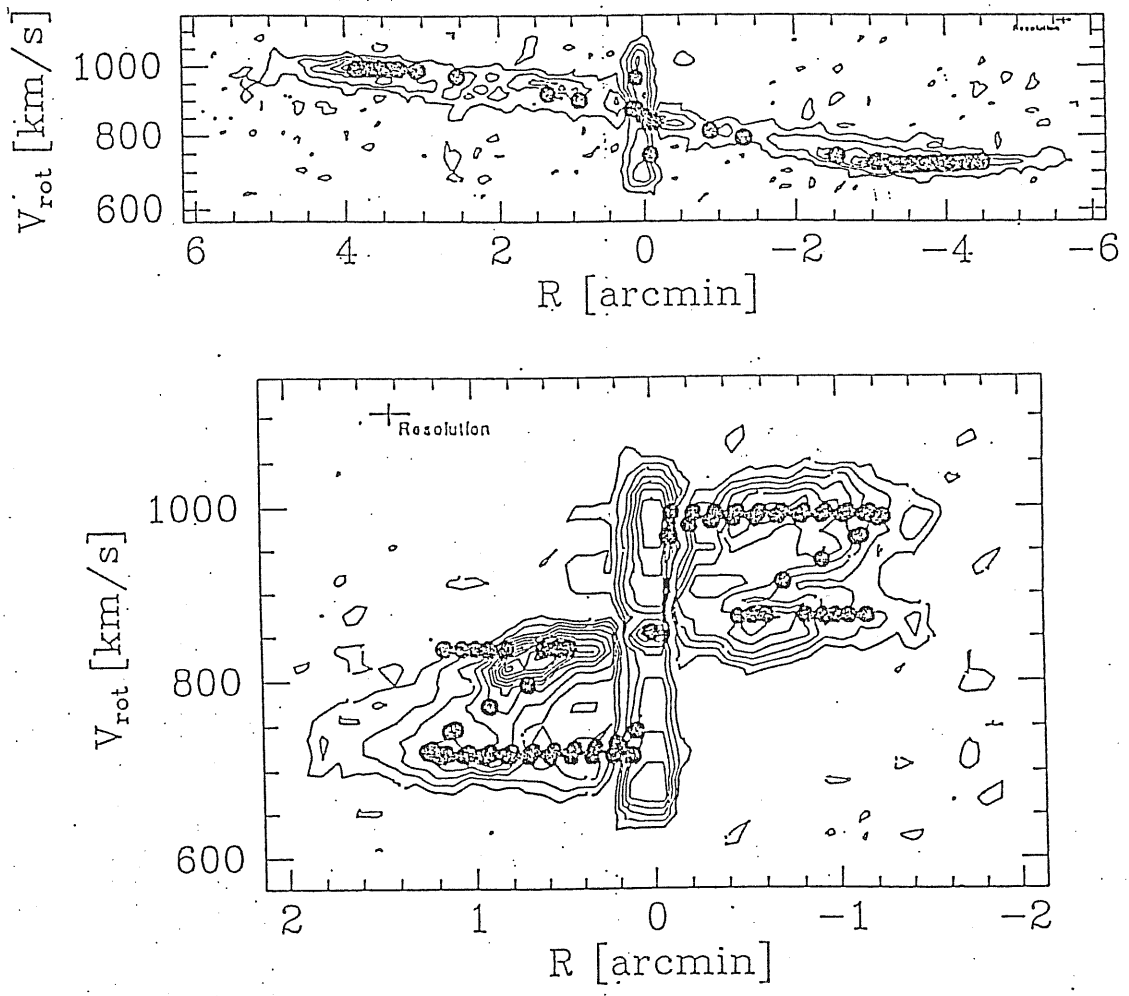

Figure 3.3: Upper panel: Axis velocity profile of HI through the center of NGC 660 at P.A. =46°, where multiple peaks are present. Lower panel: Axis velocity profile of HI through the center at P.A. =-7°. In both panels the predicted velocities at the different P.A.s from the warped gas structure are indicated with full dots, which follow exactly the multiple peaks, in HI intensity.

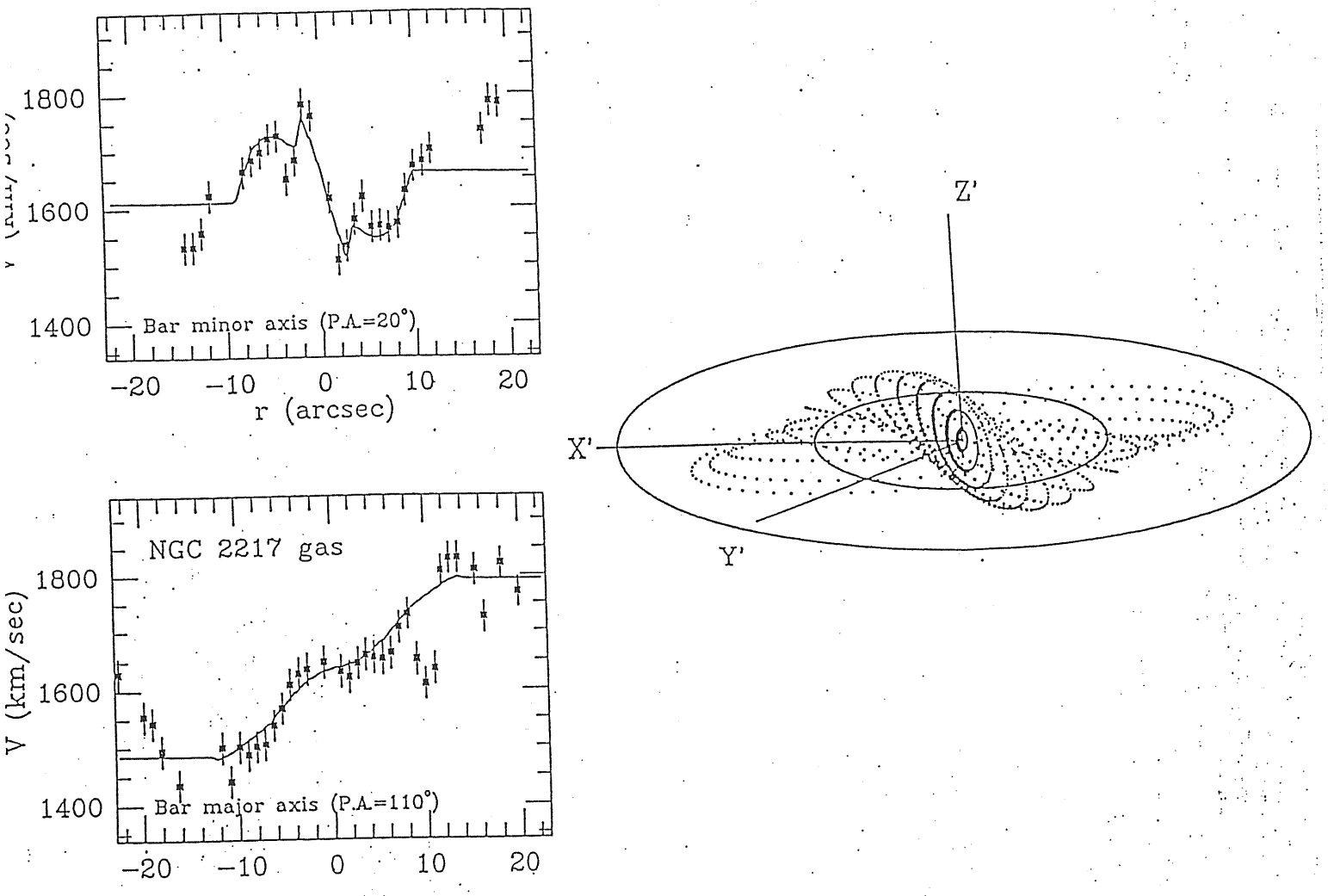

Figure 3.4: Left: Computer-simulated image of NGC 2217. Right: emission–lines rotation curves at different P.A.s and the projected velocity curves obtained from the warped structure.

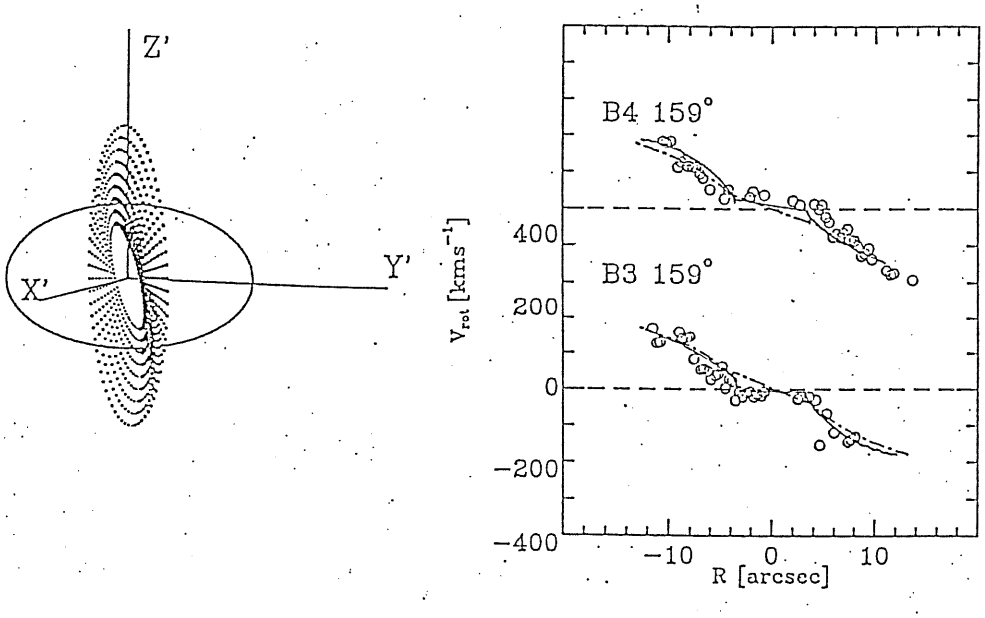

Figure 3.5: Left: Computer-simulated image of AM 2020–504, the front side of the warped structure is plotted with heavier dots. Right: open dots are data from the emission–lines rotation curves at P.A. = 159°, taken offset 2.5″ SW (B3) and NE (B4) from the nucleus. The continuous lines represent the predicted velocity curves expected from the self–gravitating warp structure; the dash-dotted lines represent the rotation curves obtained at the same slit position with no warp.

Bibliography

[1] Arnaboldi M., Capaccioli M., Cappellaro E., Held E.V., Sparke L.S., 1992, A&A, in press

[2] Benacchio L., Galletta G., 1980, MNRAS 193, 885

[3] Benvenuti P., Capaccioli M., D'Odorico S., 1976, A&A 53, 141

[4] Bertola F., Galletta G., 1978, ApJ 226, L115

[5] Bettoni D., Fasano G., Galletta G., 1990, AJ 99, 1789

[6] Binney J., 1978, MNRAS 183, 779

[7] Caldwell N., 1984, ApJ 278, 96

[8] Galletta G., 1983, Ap&SS 92, 335

[9] Gottesman S.T., Mahon M.E., 1989, H I Observations of the peculiar galaxy NGC 660. In: Sulentic J.W., Keel W.C., Telesco C.M. (eds.) Paired and Interacting Galaxies. Nasa, Washington D.C., p. 209

[10] Hawarden T.G., Elson R.A.W., Longmore A.J., Tritton S.B., Corwin H.G.J., 1981, MNRAS 196, 747

[11] Magrelli G., Bettoni D., Galletta G., 1992, MNRAS 256, 500

[12] Sancisi R., 1976, A&A 53, 159

[13] Sandage A., Freeman K.C., Stokes N.R., 1970, ApJ 160, 831

[14] Schweizer F., Whitmore B.C., Rubin V.C., 1983, AJ 88, 909

[15] Sparke L.S., 1986, MNRAS 219, 657

[16] Stark A.A., 1977, ApJ 244, 458

[17] Steiman–Cameron T.Y., Durisen R.H., 1988, ApJ 325, 26

[18] Whitmore B.C., Lucas R.A., Mc Elroy D.B., Steiman–Cameron T.Y., Sackett P.D., Olling R.P., 1990, AJ 314, 439

[19] Williams T.B., 1981, ApJ 244, 458

[20] Williams T.B., Schwarzschild M., 1978, ApJ 227, 56

Chapter 4

Observations and model for AM 2020–504

4.1 Introduction

Gas rings in early–type galaxies tend to occur in two different morphologies: rings in S0 galaxies are normally wide annuli extending out to large radii, while those in ellipticals are narrow and internal to the optical radius of the galaxy (Whitmore 1991). The rings are not inclined at random angles: they appear either near to the equatorial plane of the galaxy or near to the orthogonal plane.

Those systems where the ring is nearly orthogonal are classified as Polar Ring Galaxies (PRGs). The study of their dynamics gives a unique opportunity to acquire information on the amount and three-dimensional shape of the matter distribution generating the galactic potential, since the velocity field is mapped on two different planes (Schweizer *et al.* 1983; Whitmore *et al.* 1987a; Sackett & Sparke 1990). In particular, narrow polar rings in elliptical galaxies may help us gain insight into the still unsolved question of the intrinsic shape — triaxial, oblate or prolate — of the total galaxy potential (Merritt 1992). The inclination of the ring, and the warps and ripples in it, together with analysis of the stability of orbits in the ring plane, give constraints on the "evolutionary scenario" for the PRGs. They also help discriminate between recent merger or accretion of material from a companion or in a close encounter (Schweizer *et al.* 1983), and old rings stabilized either by self–gravity (Sparke 1986) or in a tumbling–triaxial potential (Steiman–Cameron & Durisen 1982).

In this chapter we present and model some new photometric and spectroscopic data for AM 2020–504, selected as the "*best case*" of the so–called narrow polar rings

from the Polar Ring Catalog (PRC) of Whitmore *et al.* (1990); see Arnaboldi *et al.* (1991). The system (Fig. 4.1) appears as an E4 galaxy with a luminous ring internal to the $\mu_B = 25$ mag arcsec^{-2} isophote; the ring plane is almost perpendicular to the apparent major axis of the galaxy. AM 2020–504 has a heliocentric redshift of $cz_0 = 5040$ km s^{-1} and a total blue magnitude $B_T = 14.5$ (PRC). Throughout this work we will assume $H_0 = 75$ km s^{-1} Mpc^{-1}, which makes d(AM 2020–504) = 67 Mpc, $1'' = 327$ pc.

Our new data for AM 2020–504 are presented in Section 4.2 and in Section 4.3 below; in Section 4.4 we produce photometric models for the parent galaxy and for the ring, which are analysed dynamically against the kinematical data in Section 4.5. The results are reviewed and the conclusions stated in Section 4.6.

4.2 Photometric Observations

Broad–band images of AM 2020–504 in the Johnson–Cousin B, V, and R bands, and Hα images (+ adjacent continuum) were secured with the CCD camera attached to the 1.54 m ESO–Danish telescope at La Silla, Chile, under fair seeing conditions (FWHM $\sim 1''.4 - 2''$). The narrow–band filters (FWHM= 8Å) were centered at $\lambda = 6672$Å (redshifted Hα) and $\lambda = 6772$Å (continuum). The CCD frames were bias subtracted and flat–fielded using the MIDAS data reduction package. The photometric zero–points of the B and V images were established by means of eight Landolt (1983) standard stars. We note that the corresponding sky surface brightness, $\mu_B = 21.77 \pm 0.03$ is just 0.1 mag fainter than the value required to make $B_T = 14.5$ as in PRC. Our B–light profiles are also in agreement with those published in PRC. No previous observations have been published for the V and R bands or in the narrow band filters.

The isophotal map reveals that the ring lies inside the $\mu_B = 25$ mag arcsec^{-2} isophote, *i.e.* well within the optical image of the galaxy, as shown also by the blue luminosity profile along the galaxy minor axis (Fig. 4.1). The polar ring (PR) shows up along the minor axis as secondary peaks in the B–light profile, North-West and South-East of the galaxy center. The light profile along the major axis looks perturbed on both sides close to the center, and no absorption dips are immediately evident.

In the central part of the image, the ring appears as a S–shape feature superimposed on the elliptical isophotes of the host galaxy, as would be expected from a slightly twisted ring. In order to disentangle the ring structure from the underlying, presumably smooth image of the host galaxy, we fitted ellipses to the isophotes in regions not perturbed by the ring. Excluding the inner part, where the ellipticity

Table 4.1: Major axis blue luminosity profile

Radius (arcsec)	μ_B	μ_B
0.944	19.46	19.46
1.044	19.92	19.69
1.477	20.37	19.98
1.926	20.47	20.32
2.089	20.64	20.43
2.381	20.62	20.66
2.515	20.63	20.75
2.839	20.6	20.89
3.218	20.63	21.04
3.478	20.7	21.05
3.843	20.83	21.04
4.378	21.02	21.06
4.869	21.21	21.16
5.429	21.4	21.35
6.075	21.62	21.52
6.812	21.84	21.77
7.611	22.04	21.98
8.416	22.28	22.19
9.443	22.55	22.46
10.53	22.8	22.7
11.74	23.06	22.92
13.08	23.3	23.13
14.6	23.62	23.36
16.29	23.86	23.68
18.18	24.07	24.01
20.25	24.37	24.29
22.58	24.64	24.42
25.18	24.8	24.65
28.1	24.84	24.77
31.35	25.34	25.05
34.98	25.66	25.46
39.01	26.03	25.68
43.51	26.13	26.08
48.52	26.25	26.46
54.09	27.44 NE	27.07 SW

data are meaningless given the limited resolution of our material and the dominant presence of the ring, the isophotes in the outer regions ($R \geq 8''$) are well reproduced by concentric ellipses with constant flattening, $b/a = 0.6 \pm 0.03$, and fixed orientation of the major axis, P.A.$= 72° \pm 2°$.

The $(B - R)$ map is shown in Fig. 4.2a. With respect to the host galaxy, the ring appears bluer and the image center redder. Lacking an absolute calibration for the R band, we assume that the color of the host galaxy spheroid is the mean color of an ordinary elliptical, $(B - R) \cong 1.6$ (Peletier *et al.* 1990). This would imply that the ring color is $(B - R) \cong 1.0$. The color profile along the galaxy major axis shows that the center is instead redder than the adopted average color by about $\Delta(B - R) \cong +0.4$.

It is not evident from the isophotal and color maps which is the front side of the ring. Color profiles parallel to the major axis and offset from the center are generally bluer in the NE side of the galaxy, but the asymmetry is marginal: $\Delta(B - R) = 0.03$ along the major axis. The approximate inner and outer radii for the ring are estimated by locating, in the color map, the boundaries of the region where the color is bluer than the galaxy mean color:

$$R_{in} = 3\farcs5 \pm 0\farcs5 \qquad\qquad R_{out} = 19\farcs0 \pm 0\farcs5$$

The Hα image (Fig. 4.2b) shows that the ionized gas lies along the minor axis of the galaxy. It is concentrated in clumpy structures following a S-shape stretched across the inner galaxy. The S-shape resembles a warped ring, such as that shown in Fig. 4.2c (see also Section 4.5 below). Bright Hα knots are present at the NW and SE edges of the ring, and structures of similar and stronger intensity are present along the major axis of the galaxy, close to the center ($R \leq 5''$).

4.3 Spectroscopic Observations

Spectra of AM 2020–504 were secured in two different observing runs at La Silla, Chile. During the first run, three long–slit deep spectra were taken with EFOSC at the ESO 3.6m telescope, two of them at $P.A. = 75°$ (coded E1), and a third at $P.A. = 165°$ (E2); these directions are within 3° of the galaxy major and minor axes. The spectra cover the range 5100–7100 Å with a dispersion of 2.0 Å pix^{-1}, and a spatial scale of $0\farcs67$ pix^{-1}. During the second run, four spectra were taken with the EMMI at the ESO NTT, two parallel to the minor axis ($P.A. = 159°$) and offset from the nucleus by $2\farcs5$ NE (B4) and SW (B3) respectively, one at $P.A. = 136°$

Table 4.2: Log of the spectroscopic observations

Instrument	Ident.	P.A.	Range [Å]	Time [sec]	Resolution [Å pix^{-1}]
EFOSC 3.6m	E1	75°	5100 – 7100	1800	2.0
EFOSC 3.6m	E1	75°	5100 – 7100	1800	2.0
EFOSC 3.6m	E2	165°	5100 – 7100	1800	2.0
EMMI NTT	B1	75°	4800 – 6100	3600	0.8
EMMI NTT	B3	159° (2.5″SW)	4800 – 6100	1800	0.8
EMMI NTT	B4	159° (2.5″NE)	4800 – 6100	1800	0.8
EMMI NTT	B5	136°	4800 – 6100	1800	0.8

(B5), and another along the major axis, *P.A.* = 75° (B1). The wavelength range is 4800–6100 Å, the dispersion 0.8 Å pix^{-1}, the spatial scale 0.″35 pix^{-1}, and the average seeing FWHM= 2″. With our own data, we discuss velocity measurements published by PRC and relative to the major axis of the ring (B2). A complete log of the observations is shown in Table 4.1

After proper pre–processing, the EFOSC spectra were wavelength calibrated using a longslit reduction package developed by one of us (EVH), while EMMI spectra were calibrated in the IRAF environment. For a graphical summary of our spectroscopic slit positions, see the sketch of Fig. 4.3; the spectra E1, B1, and E2 are displayed in Fig. 4.1.

Table 4.3: Major axis stellar velocity – (B1) NTT data

Radius (arcsec)	V_{rot} (km s^{-1})	Error (km s^{-1})	Radius (arcsec)	V_{rot} (km s^{-1})	Error (km s^{-1})
8.750 SW	63.61	20.47	-0.3471E-04	-14.13	9.114
8.400	61.92	18.11	-0.3500	-13.93	9.002
8.050	108.0	22.79	-0.7000	-16.33	10.36
7.700	103.3	20.76	-1.050	-46.58	11.69
7.350	121.9	50.81	-1.400	-42.68	9.692
7.000	81.95	31.60	-1.750	-43.85	11.51
6.650	80.18	28.32	-2.100	-78.91	10.07
6.300	54.90	17.99	-2.450	-110.6	19.81
5.950	95.32	16.73	-2.800	-68.70	19.16
5.600	68.18	18.62	-3.150	-96.46	15.61
5.250	116.7	19.29	-3.500	-94.62	12.95
4.900	96.97	14.38	-3.850	-86.59	12.70
4.550	125.2	15.77	-4.200	-135.8	15.80
4.200	123.4	18.61	-4.550	-105.3	16.25
3.850	100.3	20.77	-4.900	-79.48	19.19
3.500	116.0	10.45	-5.250	-113.2	12.15
3.150	86.63	9.406	-5.600	-111.7	7.132
2.800	101.7	12.55	-5.950	-64.12	8.491
2.450	88.29	13.14	-6.300	-82.77	9.179
2.100	63.52	12.64	-6.650	-72.20	6.910
1.750	64.85	18.70	-7.000	-51.63	11.94
1.400	11.19	20.18	-7.350	-101.2	30.34
1.050	55.91	12.06	-7.700	-122.6	23.77
.7000	-8.706	10.22	-8.050	-26.85	16.82
....	....	....	-8.400	8.438	34.31
....	....	....	-8.750	-22.10	18.95
....	....	....	-9.100 NE	-37.61	19.72

Table 4.4: Major axis stellar velocity – (E1) EFOSC data

Radius (arcsec)	V_{rot} (km s^{-1})	Error (km s^{-1})	Radius (arcsec)	V_{rot} (km s^{-1})	Error (km s^{-1})
20.65 SW	15.6	16.1	-0.7	-24.8	18.1
19.6	16.1	13	-1.05	-17.5	63.8
18.9	18.5	13.1	-1.4	-47.7	46.1
17.85	-13.4	36.9	-1.75	-111	61.4
17.5	-1.8	13.2	-2.1	-162	71
17.15	-1	18.4	-2.45	-135	64.5
16.8	-0.6999	15.2	-2.8	-118.3	76.3
16.45	10.7	37.1	-3.5	-96.3	74.8
16.1	2.2	12.4	-4.2	-75.3	73.3
15.4	-4.2	18.7	-4.55	-33.1	23
14.7	12	15.7	-4.9	-124.6	155.4
14	-4.9	15	-5.6	-101.8	40
12.95	-12.5	16.3	-8.05	11.3	15.4
12.6	-7.9	13.2	-8.4	-4.3	17.2
12.25	6	18.6	-8.75	1.8	15.3
11.2	8.6	13.1	-9.8	-0.9001	15.6
10.85	-7	16.2	-10.85	-1.2	12.7
9.8	2.7	16.5	-11.2	-8	14.4
9.45	-5.4	15.4	-11.55	-0.4001	14.2
8.4	10.7	14.9	-12.25	11.9	11.9
6.65	45.6	112.4	-12.6	0.4998	14
6.3	88.7	76.3	-14.35	-4	13.6
5.95	73.6	67.9	-14.7	11.2	13.3
5.6	105.3	77.9	-15.4	-11.1	12.9
4.9	139.4	69.8	-16.45	2.2	16.7
4.55	130.5	37	-17.5	23.8	22.2
4.2	49.5	72.8	-20.65 NE	1.6	12.8
3.85	82.8	44.8	....	...	....
3.15	58.6	40.8	....	...	....
2.8	119.1	44.9	....	...	....
2.45	95.2	22.2	....	...	....
2.1	118.7	28.4	....	...	....
1.75	56.3	23	....	...	....
1.4	66.4	24.3	....	...	....
1.05	4.4	20.1	....	...	....
0.7	11.3	29.3	....	...	....
0.35	-28.9	35.6	....	...	....
0	-62.6	33.5	....	...	....

Table 4.5: NTT data – Velocity dispersion

Radius (arcsec)	$\sigma(r)$ (km s^{-1})	Error (km s^{-1})	Radius (arcsec)	$\sigma(r)$ (km s^{-1})	Error (km s^{-1})
10.15 SW	89.16	56.29	-0.3471E-04	267.3	10.22
9.800	44.89	31.15	-0.3500	271.9	9.114
9.450	36.16	29.29	-0.7000	273.8	9.002
9.100	180.0	12.09	-1.050	223.0	10.36
8.750	147.4	20.47	-1.400	195.3	11.69
8.050	159.7	22.79	-1.750	240.7	9.692
7.700	136.5	20.76	-2.450	203.6	10.07
7.350	53.45	50.81	-3.150	188.0	19.16
7.000	126.8	31.60	-3.850	170.3	12.95
6.650	77.93	28.32	-4.200	184.9	12.70
5.250	147.3	19.29	-4.550	226.2	15.80
4.900	138.7	14.38	-5.250	115.4	19.19
4.550	136.9	15.77	-5.600	92.08	12.15
4.200	140.6	18.61	-6.300	111.4	8.491
3.500	164.0	10.45	-6.650	93.93	9.179
3.150	158.0	9.406	-7.000	144.5	6.910
2.800	181.0	12.55	-7.350	94.40	11.94
2.100	178.2	12.64	-7.700	101.5	30.34
1.750	152.8	18.70	-8.050	148.0	23.77
1.400	172.7	20.18	-8.400	96.32	16.82
1.050	238.1	20.18	-8.750	134.5	34.31
.7000	235.5	12.06	-9.100 NE	166.3	18.95

4.3.1 Major Axis Stellar Velocities

Kinematical information on the stellar component of AM 2020–504 are obtained from the major–axis absorption–line spectra (E1 and B1) in the range 5100–6100 Å (dominated by the Mgb and NaD features), using a Fourier Quotient package made available to us by G. Galletta. No change is introduced in the results from the EFOSC spectra by switching to the cross–correlation package developed by R. Bender (1988), or to the similar package developed by S. Levine for the IRAF environment. The velocities are plotted in Fig. 4.4 and 4.5. The interpolating curve, shown as a solid line, has been constrained to be symmetric about the nucleus. It has been computed from the folded rotational data, neglecting the EFOSC points in the innermost 9″, since their spatial resolution is lower than the NTT data.

The stellar radial velocities for the major axis confirm previous evidence of a fast rotating core inside $R = 9''$ (Whitmore *et al.* 1987b, hereafter WMSb), but they also reveal the presence of a very peculiar dynamics. First of all, due to the better spatial resolution of NTT data, the inner fast rotating core has been resolved into possible sub–components: see Fig. 4.5, where the data have been folded with respect to the center and to the systemic velocities. The rotation curve shows some evidence of two peaks, at $R = 4\farcs5$ and $7\farcs5$, reaching $|V_{rot}| = 122$ and 109 km s^{-1} respectively. Moreover, our deep EFOSC spectra disclose the presence, from $R = 9''$ and out to $20''$, of a non–rotating component. This implies a dynamical decoupling between the inner core and the surrounding bulge (see also WMSb). The decoupled core and its peculiar double–peaked rotation curve are probably related to the central color excess and to the concentration of Hα emission. This may represent material acquired when the ring formed, which has already settled down in the core and has turned into stars.

The EMMI spectrum reduced by means of the cross correlation package of Bender (1988) provided the velocity dispersion $\sigma(r)$ profile along the major axis of AM 2020–504. The velocity dispersion peaks at the center, $\sigma(0) = 270$ km s^{-1}, and decreases outwards; the same central value and the same general behaviour in the first 3″ from center are measured from the absorption lines present in the spectrum B5. Our measurements, folded about the center, are displayed in Fig. 4.5, along with those of PRC. Our central dispersion is significantly larger than the value of 153 km s^{-1} quoted in PRC; for $R > 5''$, however, our data are in agreement with PRC. The higher peak detected at the center is likely to be a consequence of our better spatial resolution. At best, *i.e.* even if the inner galaxy rotates with the same speed as the decoupled core, the ratio V_m/σ_0 is equal to 0.55 indicating that the parent galaxy is not rotationally supported (Davies *et al.* 1983).

4.3.2 Emission Lines

The gas kinematics in the ring were derived by measuring the Hα line in the EFOSC spectra and the [OIII] 5007$\AA$ line in the NTT spectra (Fig. 4.6). The fitting procedure gives an error of ± 5 km s^{-1} and ± 2 km s^{-1} on the EFOSC and NTT gas rotation curves respectively. The velocity curve from the EFOSC spectrum (E2) along the minor axis of the galaxy is asymmetric with respect to the heliocentric systemic velocity of the stellar component, $V_0 = 5040$ km s^{-1}. The velocities of the absorption lines apparent near the galaxy center in this spectrum are also larger that V_0, and are comparable with the redshift appropriate to the SW peak of the spinning core. This would suggest that our slit was offset by about 2″ from the nucleus towards the SW, an assumption consistent with the slit width and with the slit coordinates relative to a galaxy image taken simultaneously with EFOSC spectra.

The velocity curves of the gas obtained from the NTT spectra at $P.A. = 159°$ (B2-B4) are flat near the origin ($R \lesssim 0'.1$) and increasing slowly outwards, while the velocity curve at $P.A. = 136°$ is increasing rapidly near the origin and then flattens. We will consider all these rotation curves and the published one to derive a mass model for the galaxy AM 2020–504 in Section 4.5 below.

4.4 Geometrical Models

In order to produce a dynamical model for the gas in AM 2020–504, we must be able to model the host galaxy. This implies knowing whether the galaxy is intrinsically triaxial, oblate or prolate. If the figure of the galaxy is not tumbling, prolate structure is unlikely, given the presence of the fast rotating core aligned with the galaxy major axis. In fact, given a prolate structure, these orbits would lie in a plane perpendicular to the equatorial one, and they would be unstable (Binney & Tremaine 1987). If the intrinsic shape of the host galaxy is triaxial, the absence of twisting and the constant flattening of the isophotes imply one of the following two scenarios.

1. The orientation of the parent galaxy is such that the line–of–sight coincides with the long axis, but then the orbits corresponding to the PR should circle the intermediate axis and be unstable (Schwarzschild 1979).

2. We are seeing the galaxy along the intermediate axis, so the PR orbits are close to the stable long–axis orbits. Simulations of a self–gravitating PR in a stationary triaxial potential (Arnaboldi & Sparke 1992) show that it would be unstable: at first the PR begins to wobble and then it breaks up. However, the

Table 4.6: Hα line - P.A.= 165° (E2)

Radius (arcsec)	V_{rot} (km s^{-1})	Radius (arcsec)	V_{rot} (km s^{-1})
12.2 SE	−184	−0.5	−57
11.5	−185	−1.2	−31
10.9	−193	−1.8	−15
10.2	−182	−2.5	25
9.5	−166	−3.2	51
8.9	−179	−3.8	76
8.2	−172	−4.7	78
7.5	−175	−5.2	76
6.9	−182	−5.9	109
6.2	−155	−6.5	126
5.5	−143	−7.2	153
4.8	−146	−7.9	147
4.2	−136	−8.5	154
3.5	−135	−9.2	153
2.8	−127	−9.9	154
2.2	−132	−10.5	171
1.5	−94	−11.2	186
0.8	−80	−11.9	217
0.2	−86	−13.20	236
....	....	−13.90	241
....	....	−14.50	207
....	....	−15.20 NW	253

Table 4.7: OIII line – P.A.= 159° (B3)

Radius (arcsec)	V_{rot} (km s^{-1})	Radius (arcsec)	V_{rot} (km s^{-1})
−11.5 NW	169	−3.5	−30
−11.1	128	−3.1	−6
−10.8	131	−2.8	−21
−9.0	159	−2.4	−8
−8.7	142	−2.1	−6
−8.3	144	−1.7	−21
−8.0	147	−1.4	−13
−7.6	83	−1.0	−18
−6.9	54	−0.7	−7
−6.6	57	2.5	−26
−6.2	49	3.6	−21
−5.9	27	4.2	−30
−5.5	38	4.6	−155
−5.2	41	5.3	−67
−4.8	62	6.0	−120
−4.5	3	7.4	−245
−4.1	27	7.7	−239
−3.8	22	8.1 SE	−231

Table 4.8: OIII line – P.A.= 159° (B4)

Radius (arcsec)	V_{rot} (km s^{-1})	Radius (arcsec)	V_{rot} (km s^{-1})
−10.5 NW	183	2.5	22
−10.2	178	3.6	10
−9.8	183	4.1	12
−9.1	112	4.5	−1
−8.8	127	4.8	10
−8.4	131	5.2	−23
−8.1	115	5.5	−36
−7.7	112	5.9	−76
−7.4	112	6.2	−68
−7.0	95	6.6	−78
−6.7	83	6.9	−65
−6.0	52	7.3	−55
−4.6	27	7.6	−83
−4.2	51	8.0	−86
−2.1	31	8.3	−100
−1.8	47	8.7	−127
−0.7	37	9.0	−119
....	....	9.4	−107
....	....	9.7	−135
....	....	11.1	−167
....	....	11.5	−178
....	....	11.8	−174
....	....	13.6 SE	−192

Table 4.9: OIII line – P.A.= 136° (B5)

Radius (arcsec)	V_{rot} (km s^{-1})	Radius (arcsec)	V_{rot} (km s^{-1})
−6.3 NW	108	0.3	−16
−5.9	115	0.7	−6
−5.6	100	1.0	−41
−5.2	104	1.7	−48
−4.9	90	2.4	−68
−4.5	96	2.8	−96
−4.2	122	3.1	−98
−3.8	139	3.5	−106
−3.5	130	3.8	−99
−3.1	118	4.2	−102
−2.8	121	4.5	−125
−2.4	124	5.2	−74
−2.1	120	5.6	−61
−1.7	121	6.3 SE	−73
−1.4	105	....	....
−0.7	90	....	....
−0.3	55	....	....
−0.0	4	....	....

stability is recovered by introducing a slow rotation in the triaxial component along its short axis: the self–gravitating PR can be stable if its precession rate equals the figure tumbling–rate of the spheroid. In this case, according to Schwarzschild (1982) and van Albada (1987), the average rotation of stars should be comparable to the figure speed. The precession rate of the equilibrium model (Section 4.5) translates into a stellar rotation rate of ~ 5 km s^{-1} at $R = 16''$, which is too small to be detectable in our data. In conclusion, a tumbling triaxial host galaxy cannot be ruled out definitely by stability arguments, but absence of isophote *twisting* would imply that we must be looking at a triaxial system from a very particular angle. Therefore we restrict our analysis to a simple model in terms of an oblate spheroid.

To determine the orientation of the ring with respect to the galaxy, using the color map of Fig. 4.2a and the Hα image of Fig. 4.2b, we adopt the same assumptions (that the ring is circular and flat) and the same notation as in Whitmore (1984). The observed angle Φ between the major axis of the two components, and the angle θ_R of the ring from edge–on are:

$$\Phi \cong 87^\circ \pm 4^\circ; \qquad \theta_R = \pm \arcsin(b/a)_{ring} \cong \pm 18^\circ \pm 2^\circ.$$

Since the ring is close to edge–on, if we assume that the galaxy is also seen edge–on, then the angle between the equatorial plane of the galaxy and the plane of the ring, θ_I, is nearly equal to the observed elongation Φ. If the galaxy is not seen edge-on, it is intrinsically flatter than E4; then the implied value of θ_I is two–valued (depending on which side of the galaxy is in front). We find numerically that the ring does not depart by more than $\pm 12^\circ$ from polar orientation even if the galaxy is intrinsically as flat as E6/7; depending on the inclination of the galaxy, the ring could be exactly polar.

In absence of other indications, we assume that the galaxy is seen edge–on. In order to determine which is the front side of the ring, we wrote a code that computes the cumulative surface brightness of a spheroid together with an outer ring, and convolves the result with a Gaussian to simulate the effect of seeing. The photometric model contains the following components:

1. For the host galaxy we adopt an oblate Jaffe (1983) model with contours of constant luminosity density given by ellipsoids:

$$\zeta_G(x,y,z) = \frac{\zeta_G^0}{m^2\left(1+m^2\right)}, \qquad m^2 = \frac{x^2+y^2}{a^2} + \frac{z^2}{c^2}, \qquad (4.1)$$

where ζ_G^0 is the central value, and $a = r_J$ the Jaffe radius (the effective radius $r_e = 0.763 \times r_J$). The values of the parameters, found by fitting the model to the observed luminosity profiles in the outer regions, are $r_J = 16''.0 \pm 0''.5$ and axis ratio $c/a = 0.58 \pm 0.02$; the fit along the major axis is shown in Fig. 4.7a.

2. The emission from the ring is determined from the light distribution along the galaxy minor axis, after subtracting the contribution coming from the Jaffe model. The ring is taken to be azimuthally symmetric, so that its emission is just a function of the radius. We adopted a gaussian:

$$\zeta_R(r) = \zeta_R^0 \exp\left\{-\frac{1}{2}\left(\frac{r - r_R^0}{s_R}\right)^2\right\}, \tag{4.2}$$

and derived the parameters ζ_R^0, r_R^0, and s_R from fits to the luminosity profiles, ignoring the twisting of the ring (*cf.* Section 4.3.2). Under this assumption the parameters are $\zeta_R^0 = 2.0 \pm 0.7$, $r_R^0 = 13.7 \pm 0.05$, and $s_R = 5.5 \pm 0.05$.

3. We assume that the ring absorbs light from that portion of the host galaxy which lies behind it:

$$I_{obs} = e^{-\tau/\sin\theta_R} I_{em} \tag{4.3}$$

where I_{obs} is that part of the observed flux corresponding to an emission I_{em} of the host galaxy behind the ring. The optical depth τ was taken to be constant inside the ring region.

4. The photometric model is convolved with the appropriate Gaussian point spread function (FWHM= $1''.4$), and compared to the observed images.

In our composite model the surface brightness distribution in the two sides of the galaxy major axis intersected by the ring is clearly asymmetric when $\tau \neq 0$; a dip becomes evident where the ring passes in front of the galaxy. By comparison of the isophotal map for AM 2020–504 with the contour plot of the model, we see that the near side of the ring is to the NE of the galaxy nucleus. Good images of the system (PRC, Fig. 3e) seem to show a hint of an absorption lane on the NE side, supporting our contention that the NE side of the ring is in front.

In fitting the model to the observed photometric data (Fig. 4.7), we had to cope with some of its limitations:

1. In building the model we did not account for a possible central component of stars, gas and dust related to a kinematically decoupled core ($R < 9''$); see Section 4.3.1.

2. The innermost structures in our images are poorly resolved: the inner diameter of the ring along its minor axis is $2''.2$, while the seeing during observations was at best $FWHM = 1''.4$.

3. The ring appears to be twisted into an S–shape: the NW side passing SW of the core and the SE side passing to the NE are brighter than the NE and SW portions of the ring.

As a consequence we expect that the model will not be able to reproduce the observed profile along the galaxy major axis for $R \lesssim 9''$: in fact the V–band luminosity profile is less luminous there than the Jaffe profile (Fig. 4.7a). Therefore, the convolved model was compared with luminosity profiles obtained off the nucleus and parallel to the galaxy major axis. In Fig. 4.7c,d the model light profiles for the NE and SW sides (ring in front and beyond the galaxy) are plotted against the corresponding observed profiles at $3''$ SE of the nucleus and $7''$ NW respectively. By comparing the fits for the B and V images we estimate that the reddening coefficient of the ring material is $E(B-V)_R \sim 0.14$; note that the Galactic reddening is just $E(B-V) = 0.003$ (Burstein & Heiles 1982). Assuming $N_{HI}/E(B-V) = 5.1 \cdot 10^{21}$ cm^{-2}mag^{-1} (Knapp & Kerr 1974), the implied hydrogen mass would be $M_{HI} = 7.2 \cdot 10^8$ $M_\odot$: this is significantly less than the HI mass measured with the 64m Parkes telescope by O. Richter (private communication), $M_{HI} = 9 \cdot 10^9$ $M_\odot$.

Since AM 2020–504 has effective parameters $\mu_e = 22.9$ mag arcsec^{-2}, and $R_e = 4.0$ kpc, it falls in the region of the $\mu_e - R_e$ plane occupied by the so–called "bright family" of galaxies that are likely to have undergone merging or accretion phenomena (Capaccioli *et al.* 1992a,b).

4.5 Dynamical Model for the PR

The large HI mass indicates that self-gravity may play an important role in the dynamics of the ring (Sparke 1986). We have therefore tested whether the general shape of the PR in AM 2020–504 and its dynamics could be reproduced by a self–gravitating ring made up of a series of circular wires precessing in an oblate potential. We look for stable solutions with the inclination of the wires to the galaxy equator increasing with their radius (a condition required by the Hα morphology and not

permitted in absence of self–gravity; Sparke 1986), using the appropriate flattened potential to represent the galaxy.

4.5.1 The potential of the host galaxy

Since the photometry suggests an oblate spheroid as a good approximation for the light distribution, and the ring is close to being exactly polar, we will use a flattened potential to compute the velocity curve of polar orbits, integrating the equations of motion in the $xz-$plane, see Fig. 4.8. To find the velocity corresponding to a distance R from the center, we find the closed loop orbit which reaches its maximum $z-$height at that distance; the $x-$velocity at the peak height gives the speed of the material in each ring at its maximum distance from the center, corresponding to our measured rotation speed.

Under the hypothesis that light traces mass, the density law for the mass distribution is again an oblate Jaffe model:

$$\rho(x,y,z) = \frac{\rho_0}{m^2(1+m^2)}, \tag{4.4}$$

where the elliptic radius m is defined as in eq. 4.1; $a = r_j = 16''$ is the Jaffe radius, and the axis ratio $c/a = 0.6$ have the values derived in the previous section. The forces corresponding to this mass distribution may be found in terms of elementary functions using the prescription of de Zeeuw and Pfenniger (1988), Sections 5.1 and 2.7. The central density ρ_0 is to be determined from the best fit to the emission line rotation curve. The velocity curve obtained from the loop–orbits in the $xz-$plane is plotted against the data in Fig. 4.8. The predicted rotation curve deviates strongly from the observed one in the inner region, and reproduces the observed flat trend in the outer parts. The mass distribution of the Jaffe model is so strongly peaked at the center that loop orbits remain almost round even at small radii: at $0.1''$ the axis ratio of the orbits is still 0.85; and loop orbits exist also at smaller radii.

If the ring had a central hole and the inner gas orbits were seen nearly edge on, the projected radial velocity on the slit would have a shallow, linear gradient, whatever the underlying potential. Unfortunately, using our data we cannot say whether twisting is present in the ring gas distribution, changing from edge–on in the inner region to a $(b/a)_{ring} = 0.3$ in the outer parts. But if we attribute the shallowness of the inner rotation curve to twisting, our model implies a total mass inside $R = 16''$ of $1 \cdot 10^{11}$ $M_\odot$ and a mass–to–light ratio $M/L_B = 13.5$.

To investigate all the possible alternatives, we use a shallower density law for the

mass distribution, the pseudo-isothermal form:

$$\rho(x,y,z) = \frac{\rho_0}{1+m^2}; \tag{4.5}$$

the corresponding forces in the $xz-$plane are given in analytic form by de Zeeuw and Pfenniger (1988). The free parameters of the model are the core radius a and the central density ρ_0. When the system is flattened, the predicted minor-axis rotation curve is again computed integrating the equations of motions in the $xz-$plane. We obtain a good fit to the observed data using a core radius $a = 3''$ and a central density $\rho_0 = 3.48$ $M_\odot/pc^3$; integrating out to $R = 16''$, we obtain a mass of $1.8 \cdot 10^{11}$ $M_\odot$ and a mass–to–light ratio $M/L_B \sim 24$; see Fig. 4.8. For comparison, fitting a *spherical* pseudo-isothermal model to this rotation curve would give $a = 6''$ and $\rho_0 = 1.06$ $M_\odot/pc^3$, and $M/L_B \sim 12$; neglecting the oblateness of the galaxy reduces the estimated mass.

We checked the consistency of the model comparing the observed stellar velocity dispersion with the value predicted by the pseudo–isothermal model with isotropic velocity dispersion (eq. 4–124b of Binney & Tremaine 1987). The model gives $\sigma =$ 141 km s^{-1}, consistent with the quasi–flat portion of the velocity dispersion curve for $R > 2''$ along the major axis (see Fig. 4.5). The virial mass estimated using $R_h = R_e = 4$ kpc and $\langle\sigma\rangle = \sigma(0) = 270$ km s^{-1}, equals $1.7 \cdot 10^{11}$ $M_\odot$, which gives a total mass–to–light ratio of 15.

4.5.2 Warped model

The ring is assumed to extend between radii of $7''$ and $16''$; in the model it is represented as a series of concentric massive wires. We assume that each of our wires, which are equally spaced in radius, have the same mass; the surface density thus varies as $1/r$. In PR galaxies which have been mapped in HI with synthesis telescopes, the hydrogen is associated with the ring and not with the central galaxy (Schechter *et al.* 1984, van Gorkom *et al.* 1987); here we take the ring mass to be given by the measured HI mass of $M_{HI} = 9 \cdot 10^9$ $M_\odot$, as a lower limit.

Our computation followed the method of Sparke (1986). When the ring is not exactly polar, the wires exert gravitational torques on each other, as well as precessing in the gravitational field of the central galaxy. We searched for equilibrium states in which all the wires precess at the same rate, so that the ring maintains a rigid shape. In such equilibrium conditions, all the wires have the same line of nodes, crossing the galaxy equatorial plane at the same azimuth.

We computed a self-gravitating warp model in the oblate pseudo–isothermal potential with $a = 3''$, $\rho_0 = 3.48\ M_\odot/pc^3$ and with axis ratio $c/a = 0.6$. With our parameters, stable solutions are possible with a range of inclinations: one such model is displayed in Fig. 4.2c.

We check the consistency of the self-gravitating model with the observational data using a code developed by G. Galletta (Arnaboldi & Galletta 1992). This code computes the projected velocity curve along a slit at any given position for a warped disk made up of circular orbits, when the rotation speed and tilting of the orbits are specified as a function of radius. The geometry of the system is computed according to the assumption that the host galaxy is seen edge on, and that the apparent flattening $(b/a)_{ring} = 0.3$ and the position angle $\Phi = 87°$ of the apparent major axis of the ring refer to the outermost wires forming the ring. This fixes the viewing angle and the inclination $\theta_I(out)$ for the outer ring. From the possible equilibria computed with the self-gravity code we choose that with the outer wire having the inclination required by the observed geometry; in this state the ring warps through an angle $\Delta\theta = 11°$. To compute the velocity curves, the wires are positioned with their inclination to the galaxy equator increasing linearly (for the sake of simplicity) between the value $\theta_I(in)$ for the inner wire, given by the equilibrium solution, and the outer value $\theta_I(out)$, fixed by the observations. This run of inclination is close to that computed in the dynamical model itself.

The code requires the orbital velocity to be uniform along each wire; we compute this velocity using the radial force f_r due to the galaxy alone, averaged along the circular wire. The velocity v_c at radius r is given by $v_c^2 =< rf_r >$. We can then compute the velocity at different positions of the slit.

Fixing the geometry of the ring, we let the core radius a and the central density ρ_0 of the oblate spheroid modelling the host galaxy be free parameters; their values are determined from the best fits with all the emission–line rotation curves for the gas in the ring, at $P.A. = 165°$, offset SW (coded as E2 in Fig. 4.3), $P.A. = 159°$ (WMSb, PRC; B2), $P.A. = 159°$ taken offset on the two side of the ring (labelled B3 and B4), and $P.A. = 136°$ (B5). The warped ring model along with the slit positions is displayed in Fig. 4.3, the observed and computed velocity curves are shown in Fig. 4.6: the model reproduces both the symmetric curve B2 and the peculiar shapes of the other rotation curves (see Section 4.3.2). We obtain a good fit for all the rotation curves with a core radius $a = 3''$, and a central density $\rho_0 = 2.22\ M_\odot/pc^3$. This value of ρ_0 is lower than that obtained by fitting the velocities derived by integrating the elliptical orbits along the spectrum B2, but this is expected since the velocities computed according to $v_c^2 =< rf_r >$ are larger than the true minor-axis velocities.

We can verify the presence of the warp in the PR: we computed the rotation curves in the case of an unwarped disk, $\Delta\theta = 0$: this model failed to reproduce the complete sample of the emission lines rotation curves.

4.6 Discussion

This chapter deals with AM 2020–504, the prototype of a poorly known class of Polar Ring galaxies, formed by a roundish spheroid as central component and a narrow ring. The study of AM 2020–504 gives the opportunity of gaining information on the intrinsic shape of E galaxies and shedding light on the still unsolved question of the origin of PR. To this aim we collected a series of spectroscopic and photometric data in order to model the evolution and the dynamics of the system. As a first goal we were interested in determining the geometry of AM 2020–504 because of its crucial importance in any attempt to model the evolution of the polar ring. The absence of isophote twisting, the constant flattening of the isophotes in the host galaxy and some stability arguments indicate that the elliptical component is an oblate galaxy. With a detailed model of the surface brightness, assuming that the central component is seen edge-on, we were able to determine the geometry of the system: the luminosity profile of the central galaxy in AM 2020–504 is well described by an oblate Jaffe model with axis ratio $c/a = 0.6$ for $R \geq 9''$. The intrinsic inclination of the ring plane derived using the $(B-R)$ and Hα images is consistent with the ring being very nearly polar. The ring is warped and tilted 18° from edge on, passing with the NE side in front of the elliptical galaxy.

The spectroscopic data suggest that an accretion event occurred in the system. The better spatial resolution of the new spectroscopic data have confirmed previous indication of the peculiar dynamics of AM 2020–504, suggesting a possible double–peaked rotation curve in the inner core. More importantly, using the EFOSC spectrograph, we were able to obtain rotational velocities for the stellar component extending to much larger radii, thus showing the presence of a non–rotating bulge, decoupled from the rotating core. The peculiar dynamics of the stellar component, *i.e.* the core and the non–rotating bulge, together with the excess of reddening in the inner region and the bright Hα structures present in the nucleus, suggest that the rapidly spinning core might perhaps be the part of the ring already settled in the equatorial plane of the galaxy.

The large measured HI content, almost 10^{10} $M_\odot$, suggests that the gas in the ring is likely to be dynamically important. Taking the ring mass to be of the order of the measured HI mass, we find several stable self–gravitating equilibria in a potential

corresponding to the symmetric rotation curve along the minor axis of the galaxy, with its flattening given by the shape of the isophotes. We computed the predicted rotation curve along the galaxy minor axis under the hypothesis that light traces mass, *i.e.* integrating the equations of motion for polar orbits in the Jaffe potential, but the predicted curve looks different from the observed one, being nearly flat instead of rising. A pseudo–isothermal model for the galaxy was better able to reproduce the rotation curve. In this gravitational potential, we computed self–gravitating warped configurations for the polar ring, and found that these reproduce the S-shaped curve of the Hα distribution. Then we used the warped model consistent with the geometrical parameters of the system to compute rotation curves along various slit orientations for the gas in the ring. This model fits all the emission–line rotation curves obtained at different position angles and offsets, while the model with no–warping failed to reproduce them. Further work on dynamical modelling is in progress (Arnaboldi & Sparke 1992).

The derived total mass inside the polar ring is between $1 \cdot 10^{11}$ $M_\odot$ and $2 \cdot 10^{11}$ $M_\odot$, and the M/L_B ratio is between 13.5 and 24, depending on whether the gas orbits in the PR are assumed to be twisted. The virial mass computed using the central value for the velocity dispersion gives a total mass of $1.7 \cdot 10^{11}$ $M_\odot$ and a total $M/L_B = 15$.

This study performed on the polar ring galaxy AM 2020–504 supports the accretion scenario for its evolution because of the near-perpendicular orientations, large mass of HI (unusual for an elliptical), the color difference between the ring and the host galaxy, and the dynamical decoupling between the galaxy's inner core and the outer spheroid. The photometric analysis of the parent galaxy is consistent with the above statement: from its position in the $\mu_e - r_e$ plane it is found to belong to the "bright galaxy family", *i.e.* galaxies which are likely to have undergone a merging or accretion event (Capaccioli *et al.* 1992b).

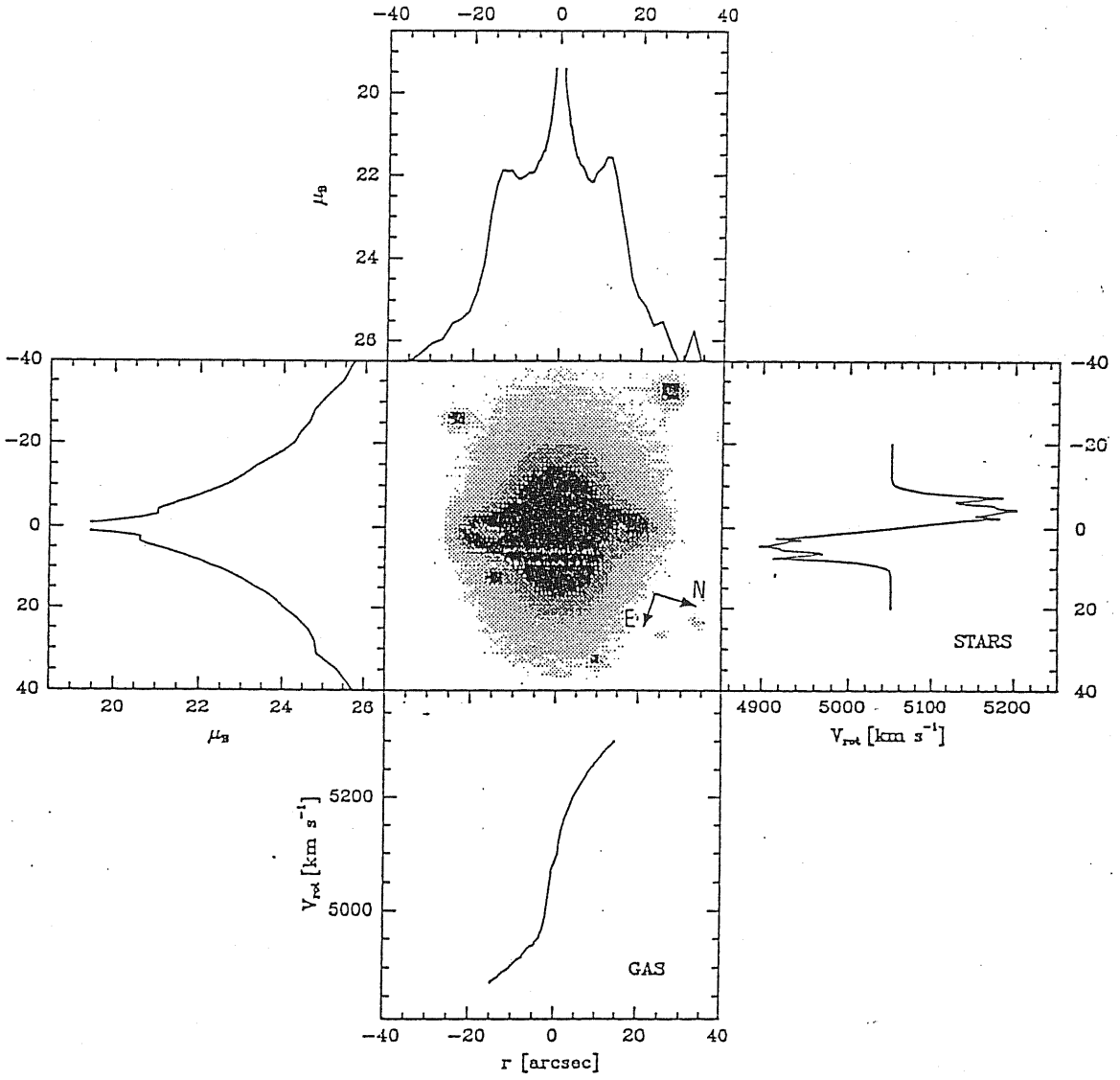

Figure 4.1: Photometric and kinematic data for AM 2020–504(central image). The upper and left panels show the blue luminosity profiles along the minor and the major axis. The rotation curves for the stellar and the gaseous component are displayed in the right and lower panels.

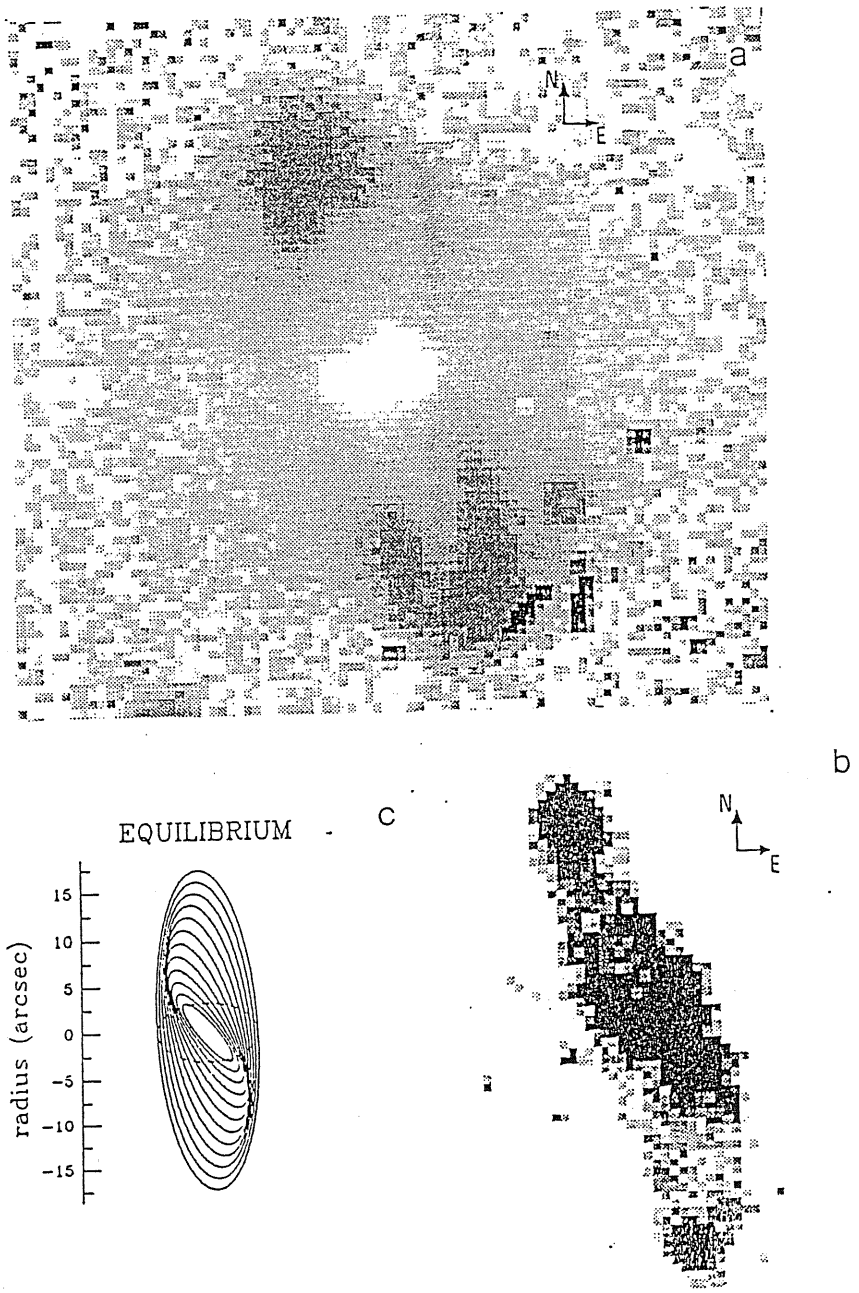

Figure 4.2: Clockwise from top left – (a) $B-R$ image: the bluer color of the material in the ring (dark upper and lower arcs) compared to the galaxy is immediately evident. The core appears much redder than the rest with an excess of reddening on the SW side. (b) Hα image: the nice overall S-shape appears together with bright knots at the edges of the ring, and strong Hα emission in the inner core of the elliptical. (c) Equilibrium model for precessing rings in an oblate potential (see text): the dashed line shows an isophote of the galaxy.

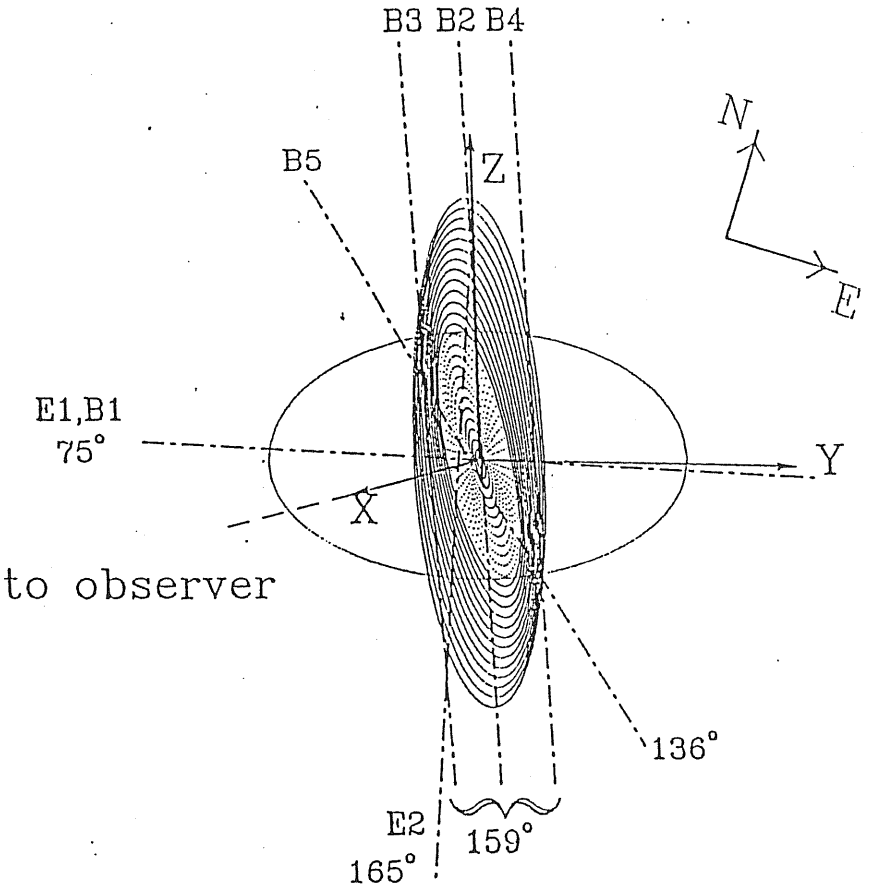

Figure 4.3: Warped model for the polar ring in AM 2020–504. The ring is represented by tilted circular orbits about the $z-$axis (see text); one isophote of the host galaxy is plotted for clarity. The positions of the slits (where spectra have been acquired and the rotation curves have been computed) are indicated with dash-dotted lines and labelled.

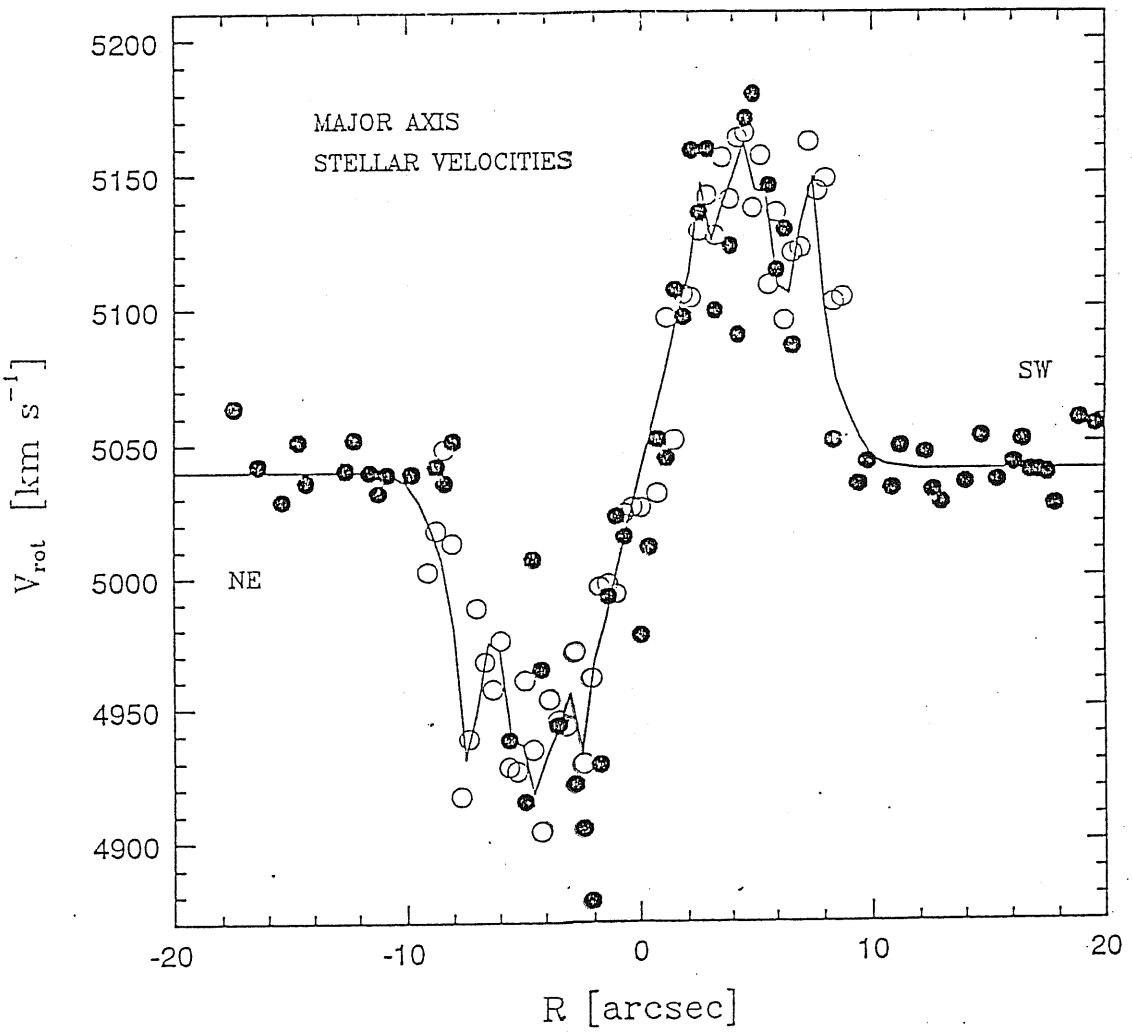

Figure 4.4: Rotation curve for the star component at P.A. = 75°. NTT data are indicated with open circles, EFOSC data are indicated with filled circles. The set of data has been fitted using a spline function (continuous line): two peaks are evident in the inner core. The average r.m.s. scatter of the observed velocities about the interpolating curve is 20 km s^{-1}.

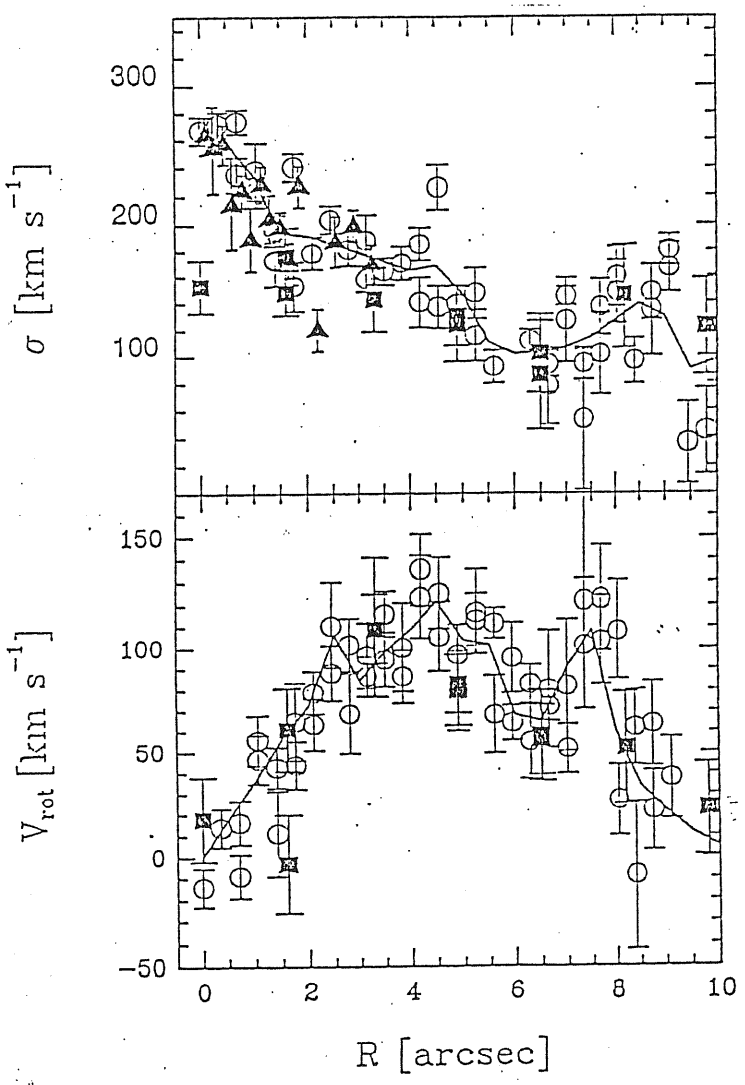

Figure 4.5: NTT data for the stellar kinematics. Upper panel: open circles represent the folded velocity dispersion data vs. radius at P.A. = 75°, black triangles represent the folded velocity dispersion data vs. radius at P.A. = 136° and PRC data are indicated with black squares; the solid line is a spline fit of the folded NTT data at P.A. = 75°. Lower panel: folded rotation curve for the stellar component at P.A. = 75°, together with the same spline interpolation as Fig. 4.4.

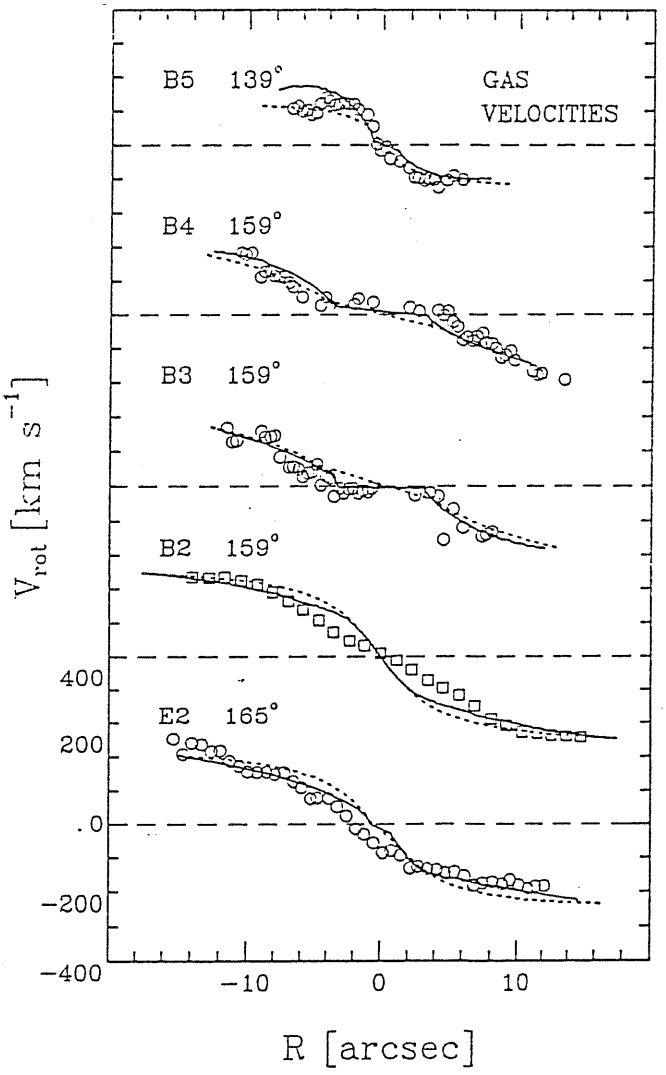

Figure 4.6: Emission line velocities in the polar ring, compared with predictions of the warped model. From the top: (B5), NTT data – OIII emission line at P.A.=136°, (B4), NTT data – OIII emission line at P.A.=159° offset 2.5" NE, (B3), NTT data – OIII emission line at P.A.=159° offset 2.5" SW, (B2), PRC data – Hα emission line at P.A.=159°, (E2), EFOSC data – Hα emission line at P.A.=165°.

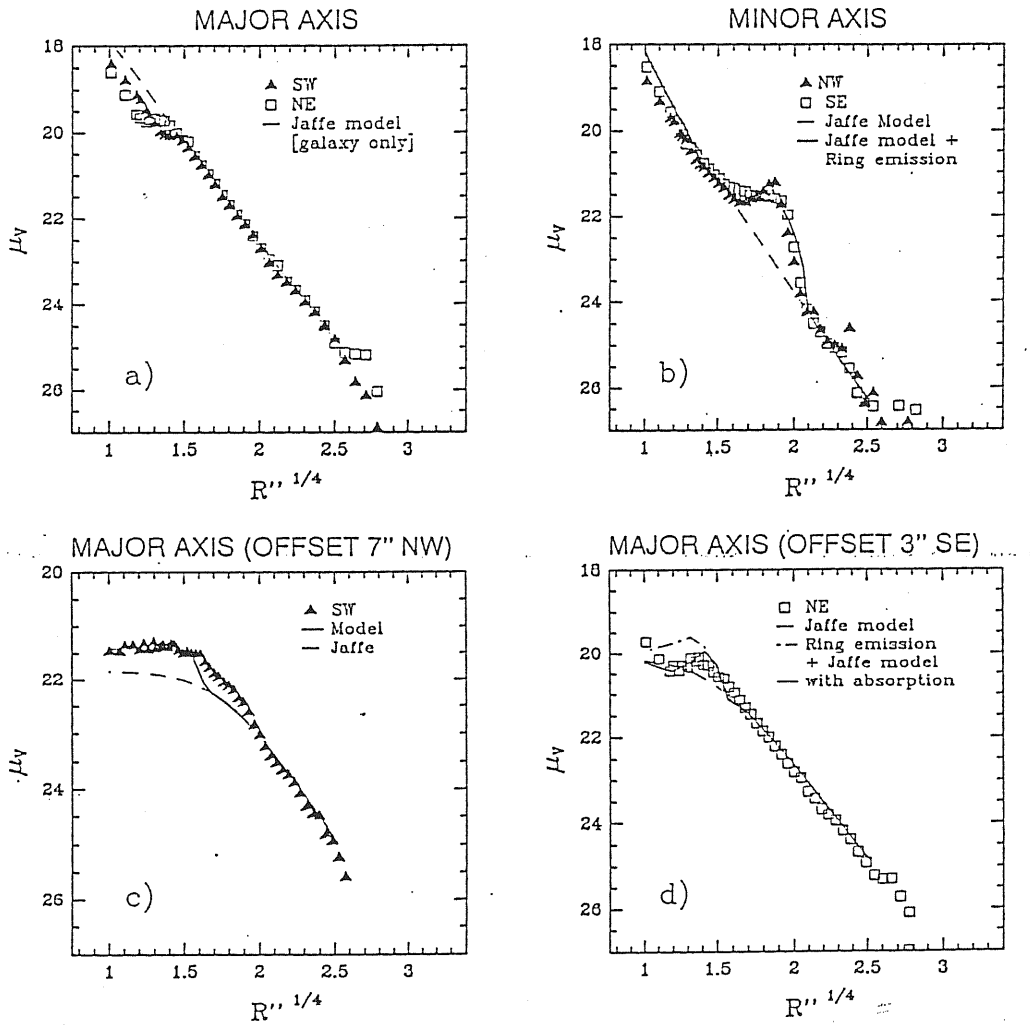

Figure 4.7: Luminosity profiles in the V–band and fits of the model to the surface brightness. The upper panels show the data and the fits along the major (a) and minor (b) axis; the lower panels show profiles taken parallel to and offset from the major axis. The SW side of the galaxy (c) is over–luminous respect to the model because the emission from the ring is concentrate in structures with different dimension; the NW side (d) shows the effect of absorption by the ring.

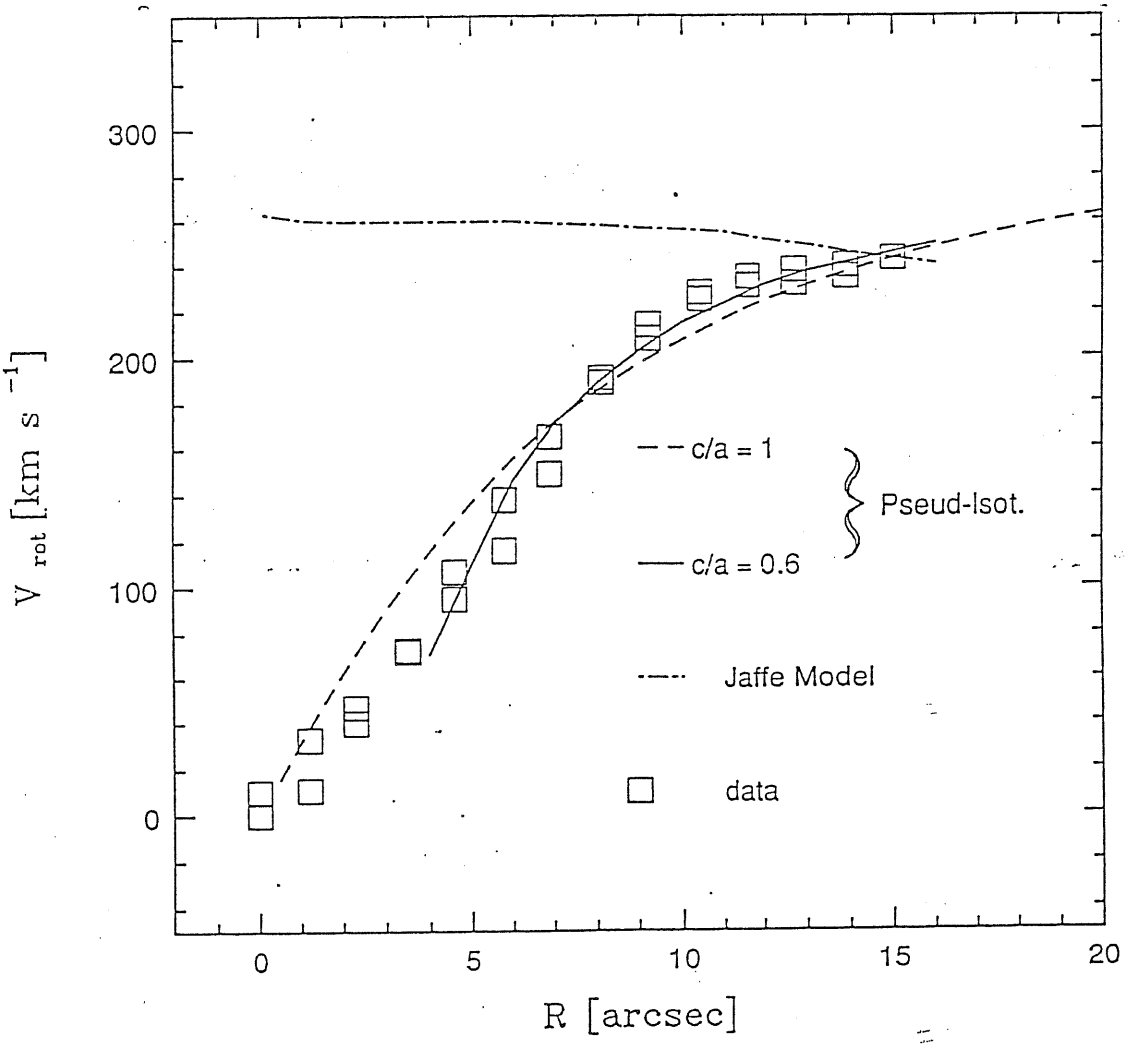

Figure 4.8: B2 data compared with the predicted rotation curves from the Jaffe model (dash-dotted line) and the pseudo-isothermal model in the spherical (dashed line) and in the flattened case (continuous line): the rotation curve predicted in the hypothesis that light traces mass (Jaffe model) has a completely different behaviour from the observed velocity curve.

Bibliography

[1] Arnaboldi M., Capaccioli M., Cappellaro E., Held E.V., Sparke L.S., Mackie G., 1991, Sissa preprint No. 181/91/a (December 91)

[2] Arnaboldi M., Galletta G., 1992, A&A submitted

[3] Arnaboldi M., Sparke L.S., 1992, in preparation

[4] Bender R., 1988, A&A 202, L43

[5] Binney J., Tremaine S., 1987, Galactic Dynamics, Princeton Univ. Press

[6] Burstein D., Heiles C., 1982, AJ 87, 1165

[7] Capaccioli M., Caon N., D'Onofrio M., Trevisani S., 1992a, New Results on Standard Candles. In: Caputo F.,(ed.) Mem. SAIt in press

[8] Capaccioli M., Caon N., D'Onofrio M., 1992b, MNRAS, in press

[9] Davies R.L., Efstathiou G., Fall S.M., Illingworth G., Schechter P.L., 1983, ApJ 266, 41

[10] de Zeeuw T., Pfenniger D., 1988, MNRAS 235, 949

[11] Jaffe W., 1983, MNRAS 202, 995

[12] Knapp G.R., Kerr F.J., 1974, A&A 35, 361

[13] Landolt A.U., 1983, AJ 88, 439

[14] Merritt D., 1992, Intrinsic Shapes of Elliptical Galaxies. In: Longo G., Capaccioli M., Busarello G. (eds.) Morphological and Physical Classification of Galaxies (Sant'Agata sui Due Golfi, Naples). Kluwer, Dordrecht, p. 309

[15] Peletier R., Davies R.L., Illingworth G.D., Davis L.E., Cawson M., 1990, AJ 100, 1091

[16] Sackett P.D., Sparke L.S., 1990, ApJ 361, 408

[17] Schechter P. L., Sancisi R., van Woerden H., Lynds C. R., 1984, MNRAS 208, 111

[18] Schwarzschild M., 1979, ApJ 232, 236

[19] Schwarzschild M., 1982, ApJ 263, 599

[20] Schweizer F., Whitmore B.C., Rubin V.C., 1983, AJ 88, 909

[21] Sparke L.S., 1986, MNRAS 219, 657

[22] Steiman–Cameron T.Y., Durisen R.H., 1982, ApJ 263, L51

[23] van Albada T.S., 1987, N-Body Simulations of Elliptical Galaxies. In: de Zeeuw T. (ed.) Proc IAU Symp. No. 127, Structure and Dynamics of Elliptical Galaxies. Reidel, Dordrecht, p. 291

[24] van Gorkom J.H., Schechter P.L., Kristian J., 1987, ApJ 314, 457

[25] Whitmore B.C., 1984, AJ 89, 618

[26] Whitmore B.C., 1991, A Few Statistics from the Catalog of Polar Ring Galaxies. In: Casertano S., Sackett P., Briggs F. (eds.) Warped Disks and Inclined Rings around Galaxies. Cambridge University Press, p. 60

[27] Whitmore B.C., Mc Elroy D., Schweizer F., 1987a, ApJ 314, 439

[28] Whitmore B.C., Mc Elroy D., Schweizer F., 1987b, AM 2020–504: an Elliptical Galaxy with an Outer Ring. In: de Zeeuw T. (ed.) Proc IAU Symp. No. 127, Structure and Dynamics of Elliptical Galaxies. Reidel, Dordrecht, p. 413 (WMSb)

[29] Whitmore B.C., Lucas R.A., Mc Elroy D.B., Steiman–Cameron T.Y., Sackett P.D., Olling R.P., 1990, AJ 314, 439 (PRC)

Chapter 5

The UV spectrum of AM 2020–504

5.1 Introduction

Whitmore (1991) has suggested that galaxies of the Polar Ring Catalogue (Whitmore *et al.* 1990) can be divided into different morphological classes:
1. — the "wide annulus" class, where an underlying S0 galaxy is circled by a wide band of gas, dust, and stars, aligned with its minor axis and extending much further out than its optical radius, and
2. — the "narrow ring" class, formed by a rounder host galaxy with a ring feature confined inside its optical boundaries.
The first class has been studied in some detail (Schweizer *et al.* 1983, Whitmore *et al.* 1987a, Sackett & Sparke 1990), being among the few tools to map the tri-dimensional shape of dark matter halos. The second class is only poorly known so far, although it appears as a good laboratory for investigating the intrinsic shape of ellipticals and accretion events.

Recent detailed observations of AM 2020–504, the "prototype" of the narrow polar ring class (Arnaboldi *et al.* 1992), have pointed out the peculiarity of this system, formed by an E4 galaxy and a blue ring. The new data have proven the occurrence of a dynamical decoupling between the inner core and the outer stellar halo, first noticed by Whitmore *et al.* (1987b). This fact, together with the great amount of HI ($\sim 9 \cdot 10^9$ $M_\odot$; O. Richter private communication) detected in the system and the different colors of the ring and the host galaxy, strongly supports the accretion scenario for the evolution of this class of polar rings. In this picture, the host galaxy

has acquired material from outside and after a period of instability, where part of this material falls into the galaxy core, the accreted gas may eventually settle down in a stable configuration (Steiman–Cameron & Durisen 1982, Sparke 1986, Arnaboldi *et al.* 1992). Such a scenario can be tested also by looking at the impact of the accreted material on the stellar population content of the host galaxy. In effect, the accretion is expected to generate a new burst of star formation and to modify the ultraviolet emission of the system by a measurable amount. UV emission may provide clues on bursts of star formation in early-type galaxies (Capaccioli 1982); with a detailed modelling, the epoch when the star burst occurred and the amount of mass involved can be estimated. These two data would provide direct information on the age of the polar ring and help discriminating whether it may be stable or just a transient phenomenon.

In this chapter we present the UV spectrum of AM 2020–504 obtained down to $\sim$ 1200 Å with the International Ultraviolet Explorer (IUE). Observations and comparison of the results are detailed in Section 5.2. In Section 5.3 we describe a model able to reproduce the smoothed trend of the IUE spectrum of AM 2020–504. The results are discussed in Section 5.4.

5.2 IUE observations

Four full–shift low–resolution spectra of AM 2020–504, two in the short–wavelength range (SWP) and two in the long–wavelength (LWP) range for a total coverage $\lambda\lambda$ 1200÷3300 Å, have been secured with IUE on June 12 to 15, 1992 at VILSPA. The long axis of the oval $10'' \times 20''$ aperture was at $27° \pm 2°$ to the polar ring major axis (see Fig. 5.1). Since the visual magnitude of the galaxy ($m_V \sim 13$) is beyond the imaging capabilities of the IUE FES, a standard blind offset technique from nearby stars was adopted to put the target into the slit. The log-book of the observations is reported in Table 5.1.

Table 5.1

Date	P.A.	Range (Å)	Exp. Time (min)
12/06/1992	4°	SWP [1000 - 2000]	380
13/06/1992	5°	SWP [1000 - 2000]	351
14/06/1992	6°	LWP [2000 - 3300]	370
15/06/1992	7°	LWP [2000 - 3300]	402

Our spectra have been consistently extracted from the so–called *line–by–line* spectra provided by the standard IUESIPS processing, which are already wavelength calibrated and photometrically linearized. Our subsequent processing includes removal of cosmic ray events and camera reseau marks as well as subtraction of a smoothed nearby background giving a time–integrated net spectrum. The final absolute flux calibrated spectrum is obtained by multiplying by the proper calibration function and dividing by the exposure time. Since our data have been processed with the current version of IUESIPS, the present LWP ITF2 calibration function (Cassatella *et al.* 1988) has been adopted for long–wavelength spectra. The short–wavelength data have been calibrated by means of the standard SWP function (Holm *et al.* 1982). The composite spectrum in the range $\lambda\lambda$ 1200÷3300 Å is shown in Fig. 5.2.

Given the faintness of the source, which is at the limit of the IUE capabilities, some words on the reliability of the UV spectral data are needed. In order to estimate the magnitude of the accidental errors, we have calculated the differences in flux between the two available spectra both in the short and in the long range. The standard deviation of the differences between pairs of 25 Å bins is $\sim$ 15% of the cumulative signal at any bins all over the IUE spectral range, with the exception of the low sensitivity intermediate region (1900 ÷ 2300 Å). The residual systematic pattern not removed by flat–fielding has been estimated using a SWP long exposure of the blank sky taken by one of us in a previous run. The magnitude of the effect is comparable with the accidental errors.

5.2.1 Comparison with other IUE spectra

The UV spectrum of AM 2020–504 appears flat in the LWP part and seems to increase in the SWP region; the spectrum is noisy in the $\lambda\lambda$ 2000÷2300 Å, owing to the low sensitivity of the LWP camera. The trend of this essentially flat UV spectrum is different from those of standard giant elliptical galaxies, which are regularly decreasing from the LW region towards shorter wavelengths and may show a UV–upturn shortwards of 2000 Å, whose amplitude depends on the metallicity of the old population (Burstein *et al.* 1988; but see also Longo *et al.* 1989).

To make a meaningful comparison of the UV spectrum of AM 2020–504 with those of other galaxies, we normalized the UV flux to the visual flux. For AM 2020–504 the magnitude inside the IUE aperture is $V = 14.54$; this figure has been obtained using a CCD frame acquired with the 1.54m Danish telescope at ESO, La Silla, on April 1991 (see Arnaboldi *et al.* 1992). The comparison of the logarithmic UV flux of AM 2020–504 with the normalized spectra of NGC 5102, M32 and NGC 4649 (Bertola *et al.* 1982, Burstein *et al.* 1988, Buson 1990) is shown in Fig. 5.3. NGC 5102 is a S0 galaxy with recent star formation, M32 is a low–metallicity dwarf galaxy with no evidence of star formation, and NGC 4649 is a high–metallicity UV–bright giant elliptical. The spectrum of AM 2020–504, though noisy, has the same flat behaviour as that of NGC 5102, being completely different from the spectrum either of M32 or NGC 4649.

5.3 Star burst model for the UV spectrum of AM 2020–504

This direct comparison between the IUE spectrum of AM 2020–504 and that of NGC 5102 suggests that at least a second burst of star formation occurred during the evolution of AM 2020–504: a detailed model of the UV spectrum can give information 1) on the epoch when the stellar burst begun, 2) for how long it lasted, and 3) how much mass was involved.

The UV spectra is modelled according to Barbaro & Olivi (1989); models are derived by the technique of evolutionary synthesis and all the phases from the main–sequence star (MS) to the post–asymptotic giant branch (p–AGB) stars are taken into account. The procedure requires 1) the computation of the spectral energy distribution (SED) of single generations of stars with different ages and chemical compositions, each of them characterized by a given metal abundance Z and helium content Y (the mass distribution function is that of Salpeter and the stellar mass range

is $0.01 - 100$ $M_\odot$), and 2) the computation of the SED of a galaxy by superposition of the fluxes of the generations, each of them weighted by the stellar birthrate. The composition of the generations forming the galaxy model is determined according to the chemical evolution theory. The contribution coming from the p–AGB is taken into account; details are discussed in Barbaro & Olivi (1989). This modelling produces the SED in a spectral range $\lambda\lambda$ 1000÷10000 Å, so it is possible to constrain the galaxy model using the observed UV spectrum and $B - R$ color, since the $B - R$ color predicted from the model can be evaluated form the optical part of the SED, through the appropriate calibration functions.

The mean color of AM 2020–504 within the centered IUE aperture stretching at $\langle$P.A.$\rangle \simeq 6°$ (mean value over the full run) is $B - R = 1.4$. In order to estimate the uncertainty associated with the above figure, we have computed the integrated color inside centered circular aperture with increasing radius $R = 5'', 7''.5, 10'', 12''.5$. Results ($B-R = 1.50$, 1.42, 1.37, 1.35) indicate that the color becomes bluer as bigger portions of the ring are enclosed into the aperture. Lacking an absolute calibration for the R band (*cf.* Arnaboldi *et al.* 1992) and because of the strong color gradient from the nucleus to the outer regions, we will assume an average $B - R \sim 1.41 \pm 0.05$.

The model assumes that a star burst took place in a E galaxy of 16 Gyr, with a birth–rate given by $\psi = \psi_0 \exp(-\beta t)$ and $\tau = 1/\beta = 1$ Gyr. The parameters of the model for the star burst are: the duration Δt, its intensity ψ_1, and the time T_{final} when the end of star formation occurred; the average metallicity Z is assumed to be equal to 0.03. The SED to be compared to the observed UV spectrum and color is the sum of the SEDs coming form the E galaxy and the star burst. The observed spectrum was corrected for extinction assuming an $E(B - V) = 0.14$ (Arnaboldi *et al.* 1992) and the extinction curve by Savage & Mathis (1979).

We obtained good agreement between the average UV spectrum of AM 2020–504 (see Fig. 5.4) and a model with $\Delta T = 1 \cdot 10^8$ yr, $\psi_1/\psi_0 = 3 \cdot 10^{-2}$, and the end of the star formation taken at $5 \cdot 10^7$ yr ago, which predicts a color index $B - R = 1.41$; the average UV spectrum of AM 2020–504 is listed in Table 5.2 and 5.3. The model gives a lower limit to the age of the polar ring in AM 2020–504 of $1.5 \cdot 10^8$ yr. The mass of the ring transformed in stars is $\sim 4 \cdot 10^8$ $M_\odot$, 1/20 of the HI mass detected in the ring.

Table 5.2

SWP average spectrum

Wavelenght (Å)	Flux (10^{-15} erg s^{-1} $Å^{-1}$)
1225	4.556
1250	2.581
1275	3.139
1300	2.07
1325	1.736
1350	2.471
1375	0.7866
1400	1.498
1425	1.104
1450	2.525
1475	1.72
1500	3.439
1525	2.546
1550	2.374
1575	2.045
1600	0.8169
1625	1.415
1650	1.64
1675	5.9395e-02
1700	1.509
1725	2.42
1750	2.623
1775	1.954
1800	1.901
1825	2.033
1850	1.573
1875	1.418
1900	1.816
1925	0.9952
1950	1.105
1975	1.602

Table 5.3

LWP average spectrum

Wavelenght (Å)	Flux 10^{-15} (erg s^{-1} $Å^{-1}$)	Wavelenght (Å)	Flux 10^{-15} (erg s^{-1} $Å^{-1}$)
1978	2.101	2728	1.461
2003	1.696	2753	1.377
2028	1.856	2778	1.189
2053	0.1767	2803	1.077
2078	1.812	2828	0.9265
2103	4.087	2853	1.197
2128	2.026	2878	1.409
2153	1.6	2903	1.149
2178	1.756	2928	1.521
2203	2.342	2953	1.599
2228	1.828	2978	1.044
2253	0.7476	3003	1.252
2278	1.438	3028	1.51
2303	1.024	3053	0.5473
2328	1.849	3078	0.9174
2353	1.541	3103	1.138
2378	1.298	3128	1.381
2403	1.501	3153	2.118
2428	1.422	3178	2.971
2453	1.957	3203	0.7755
2478	2.031	...	...
2503	1.651	...	...
2528	1.216	...	...
2553	1.01	...	...
2578	0.9377	...	...
2603	1.414	...	...
2628	1.239	...	...
2653	1.431	...	...
2678	1.615	...	...
2703	1.589	...	...

5.4 Conclusion

New IUE spectra acquired for the galaxy AM 2020–504 support previous evidence of an accretion event in this system. The UV spectrum in the range $\lambda\lambda$ 1200÷3200 Å shows a general flat trend and a slight rise towards the shorter wavelengths. The logarithmic flux of AM 2020–504, normalized with respect to the visual magnitude in the IUE aperture, closely resemble the spectrum of NGC 5102, a galaxy with strong evidence of recent star formation.

The UV SED is reproduced by a model consisting of an elliptical galaxy with a star burst, which started $1.5 \cdot 10^8$ yr ago and lasted for $1 \cdot 10^8$ yr, with an intensity $\psi_1/\psi_0 = 3 \cdot 10^{-2}$. This gives a lower limit of to the age of the polar ring ($1.5 \cdot 10^8$ yr) and is consistent with the structure being quite young.

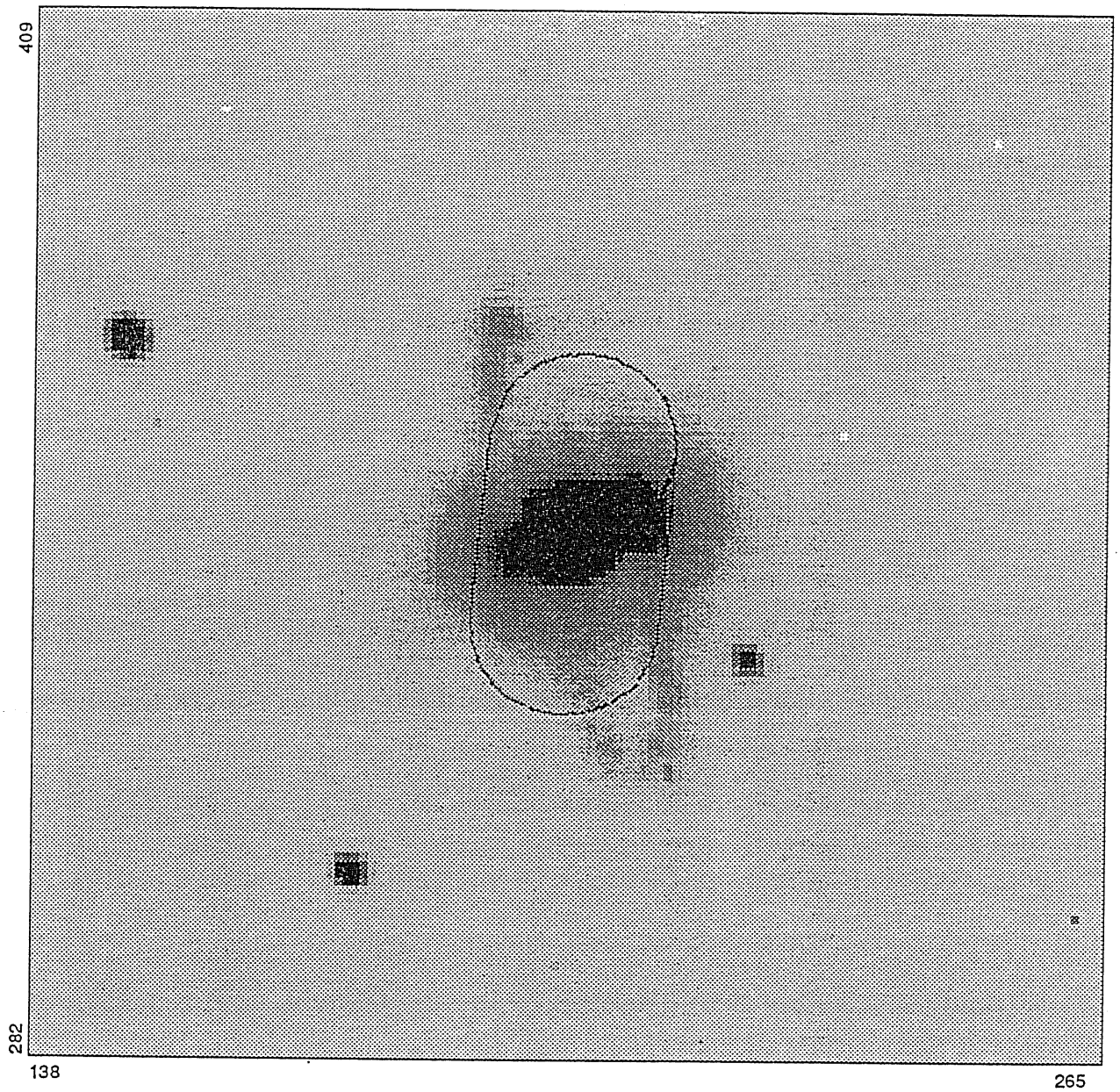

Frame : amv0001
Identifier : AM2020/V/30M
ITT-table : ramp.itt
Coordinates : 138, 282 : 265, 409
Pixels : 1, 1 : 512, 512
Cut values : 100, 750
User : EMMECI

Figure 5.1: CCD image of AM 2020–504 in the V band (15 min exposure). The black contour indicates the position of IUE aperture; North is up and East on the right.

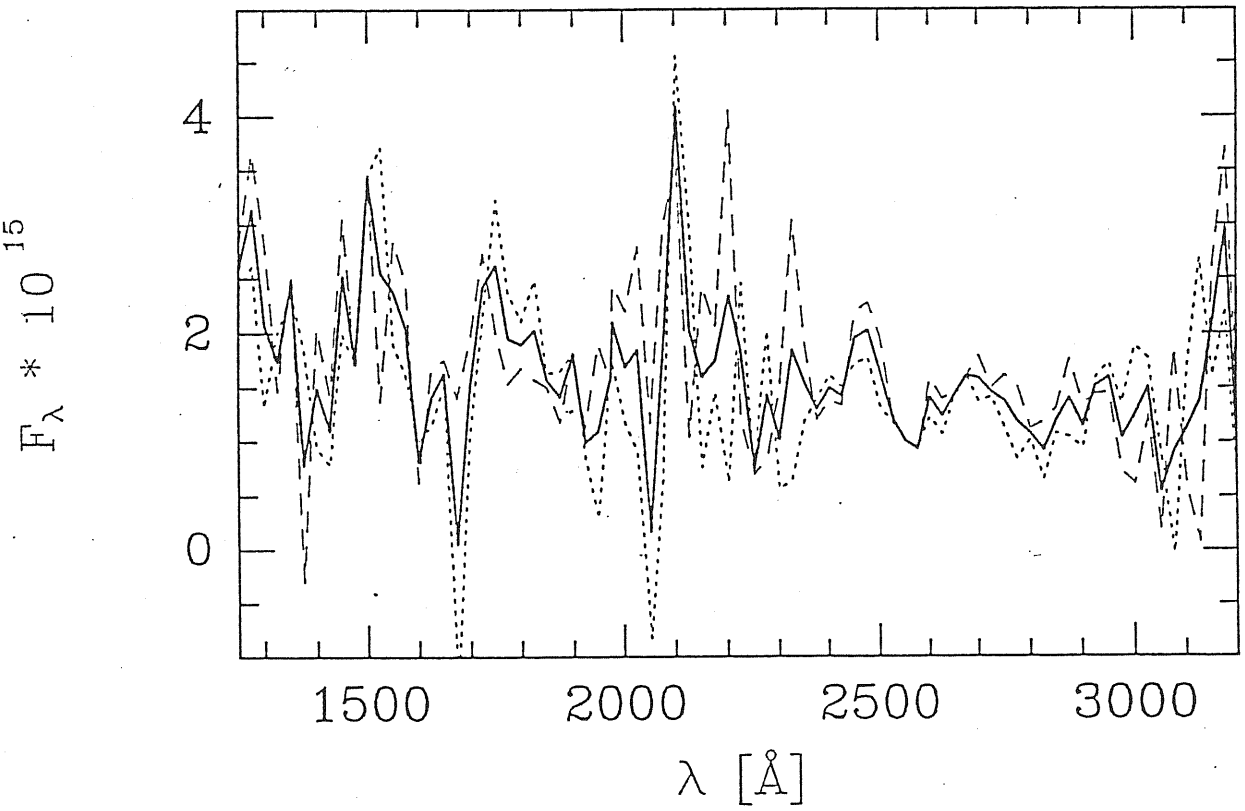

Figure 5.2: The complete UV spectrum (SWP + LWP) of AM 2020–504. The two SWP and two LWP spectra have been reduced separately (dotted and dashed lines respectively); the mean spectrum is displayed using a continuous line. The spectra shown in the figure are rebinned linearly in bins of 25 Å.

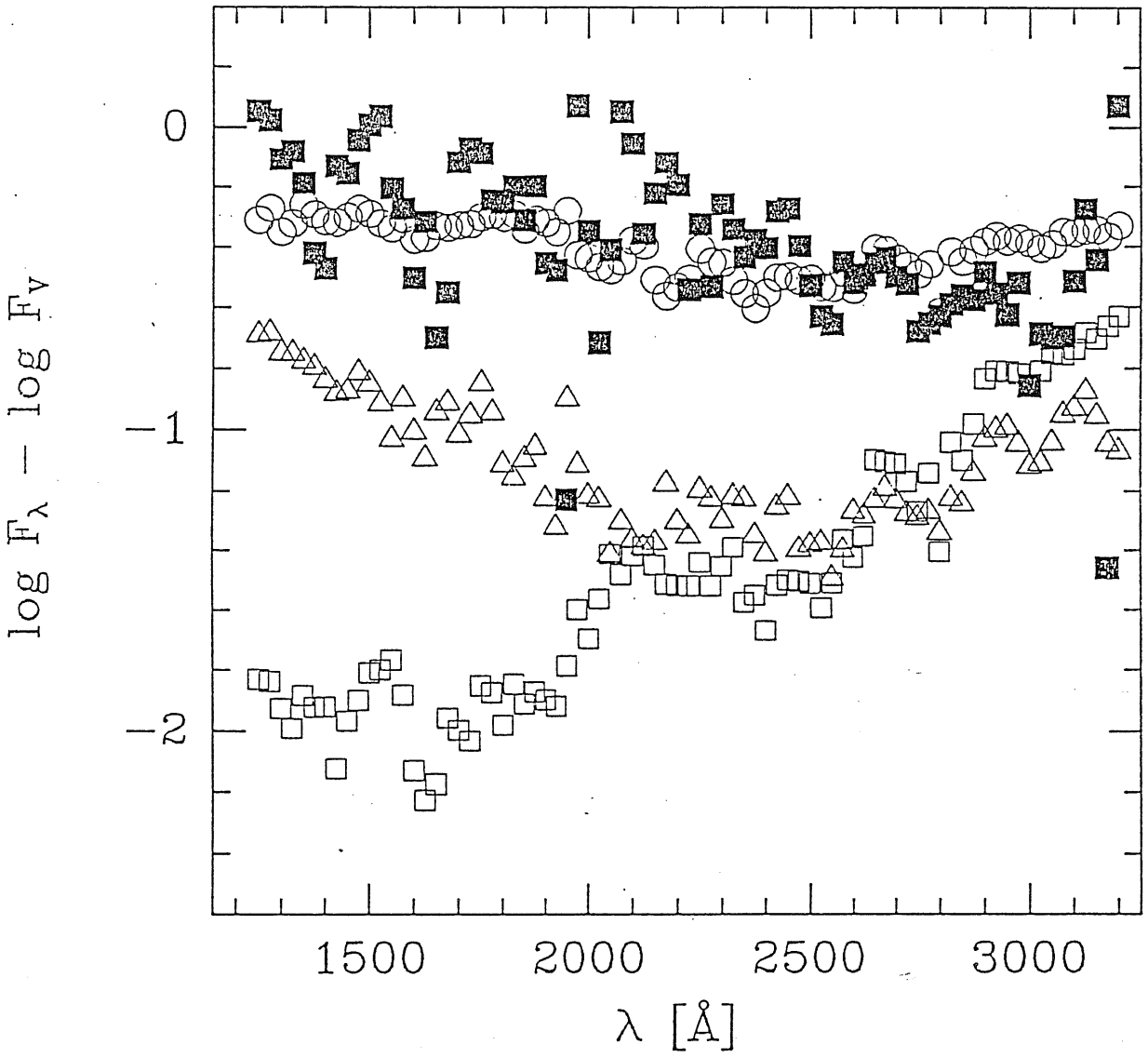

Figure 5.3: Comparison between the UV spectrum of AM 2020–504 and those of NGC 5102, M32 and NGC 4649. Fluxes are expressed on a logarithmic scale, normalized to the visual magnitude. Data for AM 2020–504 are indicated with full squares, while those of NGC 5102, M32 and NGC 4649 with open circles, squares, and triangles respectively.

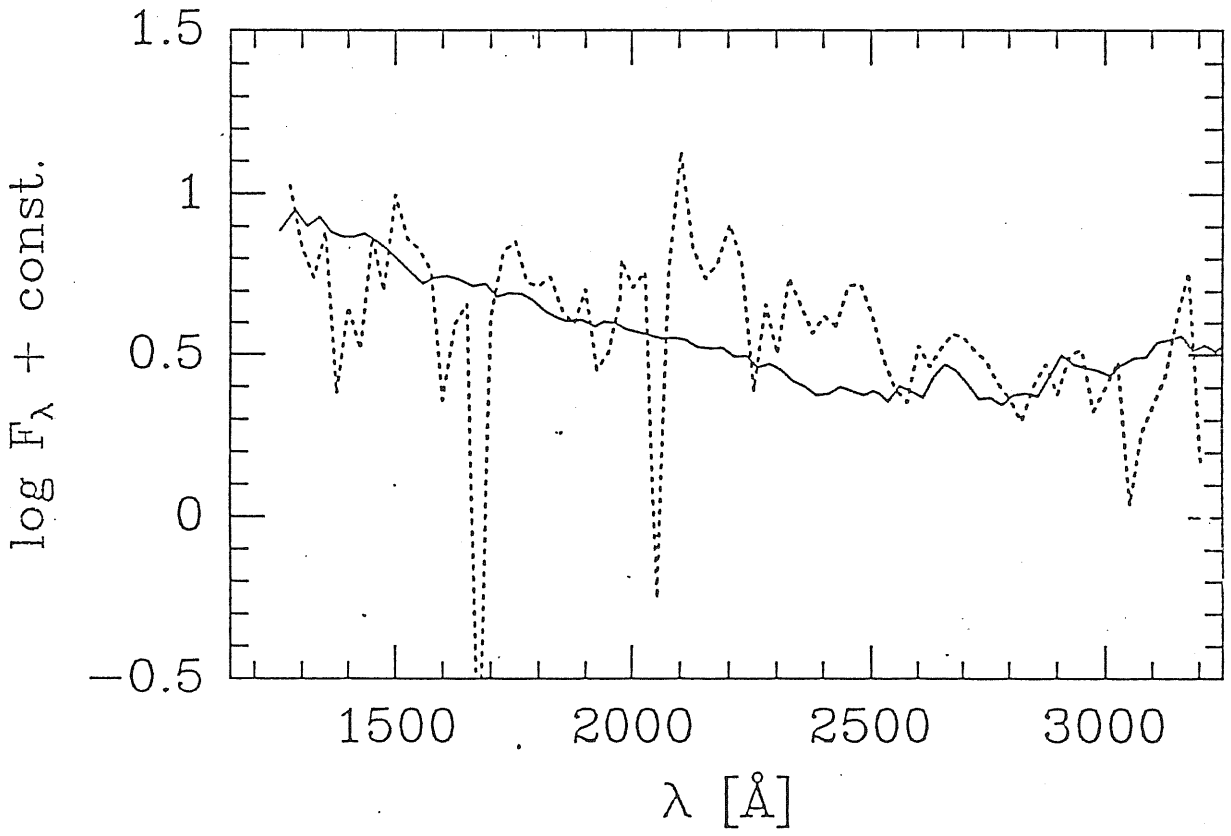

Figure 5.4: The observed UV spectrum of AM 2020–504 plotted against the predicted SED from the star burst model. The flux (units 10^{-15} erg cm^{-2} s^{-1} Å^{-1}) is expressed on a logarithmic scale.

Bibliography

[1] Arnaboldi M., Capaccioli M., Cappellaro E., Held E.V., Sparke L.S., 1992, A&A, in press

[2] Barbaro G., Olivi F.M., 1989, ApJ 337, 125

[3] Bertola F., Capaccioli M., Oke J.B., 1982, ApJ 254, 494

[4] Burstein D., Bertola F., Buson L.M., Faber S.M., Lauer T.R., 1988, ApJ 328, 440

[5] Buson L.M., 1990, The Far–UV Spectra of Early–Type Galaxies. In: Ferrini F., Franco J., Matteucci F. (eds.) Chemical and Dynamical Evolution of Galaxies. ETS Editrice, Pisa, p. 192

[6] Capaccioli M., 1982, Stellar populations in normal galaxies. In: Third European IUE Conference. ESA SP–176, p. 59

[7] Cassatella A., Ponz D., Selvelli P.L., Vogel M., 1988, ESA IUE Newsletter 31, 1

[8] Holm A.V., Bohlin R.C., Cassatella A., Ponz D., Schiffer III F.H., 1982, A&A 112, 341.

[9] Longo G., Capaccioli M., Bender R., Busarello G., 1989, A&A 225, L17

[10] Sackett P.D., Sparke L.S., 1990, ApJ 361, 408

[11] Savage B.D., Mathis J.S., 1979, ARA&A 17, 73

[12] Schweizer F., Whitmore B.C., Rubin V.C., 1983, AJ 88, 909

[13] Sparke L.S., 1986, MNRAS 219, 657

[14] Steiman–Cameron T.Y., Durisen R.H., 1982, ApJ 263, L51

[15] Whitmore B.C., 1991, A Few Statistics from the Catalog of Polar Ring Galaxies. In: Casertano S., Sackett P., Briggs F. (eds.) Warped Disks and Inclined Rings around Galaxies. Cambridge University Press, p. 60

[16] Whitmore B.C., Mc Elroy D., Schweizer F., 1987a, ApJ 314, 439

[17] Whitmore B.C., Mc Elroy D., Schweizer F., 1987b, AM 2020–504: an Elliptical Galaxy with an Outer Ring. In: de Zeeuw T. (ed.) Proc IAU Symp. No. 127, Structure and Dynamics of Elliptical Galaxies. Reidel, Dordrecht, p. 413 (WMSb)

[18] Whitmore B.C., Lucas R.A., Mc Elroy D.B., Steiman–Cameron T.Y., Sackett P.D., Olling R.P., 1990, AJ 314, 439